LBL-35568
UC-413

Lawrence Berkeley Laboratory
UNIVERSITY OF CALIFORNIA

Searches for Massive Neutrino Emission in ^{14}C Beta and ^{55}Fe Electron-Capture Decays

F.E. Wietfeldt
(Ph.D. Thesis)

May 1994

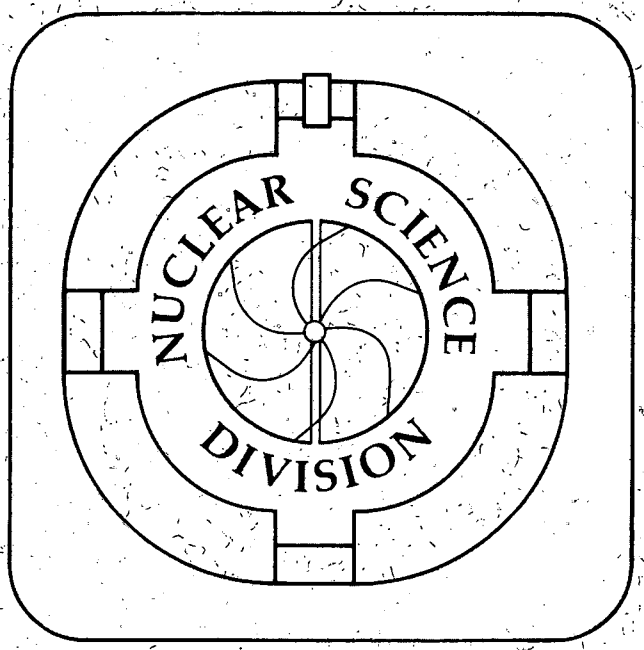

Prepared for the U.S. Department of Energy under Contract Number DE-AC03-76SF00098

DISCLAIMER

LBL-35568

Searches for Massive Neutrino Emission in ^{14}C Beta and ^{55}Fe Electron-Capture Decays

Fred Eberhardt Wietfeldt

Ph.D. Thesis

Department of Physics

University of California

and

Nuclear Science Division

Lawrence Berkeley Laboratory

University of California

Berkeley, CA 94720

May 1994

This work was supported by the Director, Office of Energy Research Division of Nuclear Physics of the Office of High Energy and Nuclear Physics of the U.S. Department of Energy under Contract DE-AC03-76SF00098.

Abstract

Searches for Massive Neutrino Emission in ^{14}C Beta
and ^{55}Fe Electron-Capture Decays

by

Fred Eberhardt Wietfeldt

Doctor of Philosophy in Physics

University of California at Berkeley

Professor Eugene D. Commins, Chair

In 1985 Simpson reported evidence for the emission of a 17 keV mass neutrino in a small fraction of tritium beta decays [1]. An experimental controversy ensued in which a number of both positive and negative results were reported. The beta spectrum of ^{14}C was collected in a unique ^{14}C-doped planar germanium detector and a distortion was observed that initially confirmed Simpson's result. Further tests linked this distortion to a splitting of the collected charge between the central detector and the surrounding guard ring in a fraction of the events. A second ^{14}C measurement showed no evidence for emission of a 17 keV mass neutrino. In a related experiment, a high statistics electron-capture internal-bremsstrahlung photon spectrum of ^{55}Fe was collected with a coaxial germanium detector. A local search for departures from a smooth shape near the endpoint was performed, using a second-derivative technique. An upper limit of 0.65% (95% C.L.) for the mixing of a neutrino in the mass range 5–25 keV was established. The upper limit on the mixing of a 17 keV mass neutrino was 0.14% (95% C.L.).

[1] J.J. Simpson, Phys. Rev. Lett. **54**, 1891 (1985).

Contents

List of Figures

List of Tables

Acknowledgements

First and foremost, I would like to thank my adviser, mentor, and friend, Rick Norman, for the marvelous experience of working with him during the past three years. He taught me a lot about physics, and how to think about physics; and he inspired me with his wonderful spirit and love of science. I will never forget the great care and attention he gave to me and to my education.

I am grateful to Stuart Freedman, Gene Commins, and Bob Stokstad for their tremendous support, wisdom, encouragement, and advice. I thank all of my friends and colleagues at Berkeley, in particular Yuen-Dat Chan, Ruth-Mary Larimer, Kevin Lesko, Tiago da Cruz, Munther Hindi, and Iuda Goldman. Working with them has greatly enriched my experience here. I especially thank my good friends Igor Žlimen, whose contributions to the ^{55}Fe experiment were invaluable; and Alejandro García, who taught me more about doing experiments than he probably realizes. I am indebted to Bhaskar Sur, Paul Luke, Eugene Haller, Al Smith, Dick McDonald, and Chris Cork for their important contributions to the ^{14}C experiment through all of its tribulations.

I thank Claude Lyneis and the staff of the 88-Inch Cyclotron for their hospitality and support throughout my work at LBL; and the superb faculty and staff of the U.C. Berkeley physics department for a deeply rewarding and enjoyable four years. Special thanks to Anne Takizawa for her boundless energy and help in smoothing out the administrative bumps.

Finally, I am grateful for Wednesday night mountain biking with John and

Marisa, and Saturday night Scrabble marathons with Tony and Laarni, for restoring my sanity after many hours in the lab.

Tota in minimis existit natura.

All of nature is in the smallest things.

–Latin Proverb

The bigger they come, the harder they fall.

–American Proverb

Introduction

In 1930 Pauli first postulated the existence of a new light, neutral particle to explain the continuous electron spectrum observed in beta decay [1]. At that time the notion of an "undetectable" particle was abhorrent to many; in fact a competing model by Bohr that violated energy conservation in beta decay was initially more popular [2]. Four years later Fermi included the neutrino in his theory of beta decay [3] and it became a permanent part of our picture of nature. Neutrinos were not unambiguously detected until 1958, when Reines and Cowan measured the cross-section for antineutrino capture by hydrogen [4]. Three types of neutrinos (ν_e, ν_μ, ν_τ) are now firmly ingrained in our Standard Model of particle physics; yet they remain an enigma. We have many questions:

- Do neutrinos have rest mass, and if so what is the mass spectrum?
- Are neutrinos purely left-handed (and antineutrinos purely right-handed)?
- Are neutrinos and antineutrinos distinct particles?
- Do lepton flavors mix in weak charged-current interactions (like quarks)?
- Are neutrinos stable or do they decay?

Actually all of these questions are intimately related to neutrino mass. Any measurement of a neutrino mass, or stricter limit on its mass, will help lead us to the answers and hopefully point us in the direction of new physics.

Neutrinos are readily produced in nuclear processes and once made they have a tiny probability for interaction or annihilation. They were created in great quantity during the big bang, and many astronomical objects such as stars and supernovae are copious neutrino sources. This makes them the most abundant type of matter in the universe. Even with a tiny mass they could dominate the mass density of the universe and therefore play a crucial role in cosmology. Neutrino mass could explain the observed solar neutrino deficit and would be important for understanding neutrino signals from other objects such as supernovae and active galactic nuclei.

This work was motivated by John Simpson's 1985 report of evidence that the electron neutrino contains a 1% admixture of a 17 keV mass state; and the subsequent experiments that both refuted and supported his claim. The first chapter outlines the theory of neutrino mass in the Standard Model and simple extensions; describes laboratory tests and present limits on neutrino mass and mixing; and discusses some of the important implications of neutrino mass in physics. The second chapter chronicles the history of the 17 keV neutrino, from the initial evidence, through the various experiments and experimental issues, to the final conclusion that the 17 keV neutrino does not exist. In the third chapter I describe an experiment, conducted at Lawrence Berkeley Laboratory (LBL), that initially showed evidence supporting the 17 keV neutrino in a ^{14}C-doped germanium detector, but was later determined by us to be mistaken. The fourth chapter describes another experiment performed at LBL that strictly ruled out the presence of a 1% 17 keV neutrino in the internal-bremsstrahlung-electron-capture (IBEC) decay of ^{55}Fe. In the final chapter I draw some conclusions about the 17 keV neutrino story and discuss some lessons that we can perhaps learn from it.

Chapter 1

Neutrino Mass

1.1 Neutrinos in the Standard Model

The Weinberg-Salam-Glashow electroweak Standard Model unifies the electromagnetic and weak interactions. It is formulated as a gauge field theory, in analogy to the very successful theory of quantum electrodynamics. The fundamental fermion fields Ψ are separated into their left and right chiral projections:

$$\Psi_L \equiv \frac{1}{2}(1-\gamma_5)\Psi, \qquad \Psi_R \equiv \frac{1}{2}(1+\gamma_5)\Psi \tag{1.1}$$

with

$$\Psi_L + \Psi_R = \Psi. \tag{1.2}$$

For massless fermions Ψ_L and Ψ_R correspond to particles of helicity -1 and $+1$. The Standard Model begins with three generations of massless quarks and leptons, each assigned two quantum numbers: weak isospin T_w, and electric charge Q.* Within each generation the left-handed quarks and leptons are arranged into weak isospin doublets and the right-handed quarks and leptons into singlets. In the first

*Strictly speaking, the group structure $SU(2)_L \times U(1)$ contains the quantum numbers T_w and Y_w (weak hypercharge), with $Y_w = 2(Q - T_{w3})$.

Table 1.1: Quantum number assignments in the electroweak Standard Model.

Fermion	T_w	T_{w3}	Q
ν_{eL}	$\frac{1}{2}$	$+\frac{1}{2}$	0
ν_{eR}	0	0	0
e_L	$\frac{1}{2}$	$-\frac{1}{2}$	-1
e_R	0	0	-1
u_L	$\frac{1}{2}$	$+\frac{1}{2}$	$+\frac{2}{3}$
u_R	0	0	$+\frac{2}{3}$
d_L	$\frac{1}{2}$	$-\frac{1}{2}$	$-\frac{1}{3}$
d_R	0	0	$-\frac{1}{3}$

generation we have

$$\begin{aligned} &\text{leptons}: && \begin{pmatrix} \nu_e \\ e \end{pmatrix}_L && e_R && \nu_{eR} \\ &\text{quarks}: && \begin{pmatrix} u \\ d \end{pmatrix}_L && u_R && d_R \end{aligned} \tag{1.3}$$

with T_w and Q assignments as shown in Table 1.1. These assignments are motivated by the observed electric charges of the particles and the observation of maximal parity violation in weak decays; i.e. only left-handed particles are seen to participate. The ν_{eR} has zero weak isospin and zero charge, so it does not interact with the other particles. The second (ν_μ, μ, c, s) and third (ν_τ, τ, t, b) generations are arranged in a similar way.

The charged fermions are known to have mass. Mass is added to the theory by introducing the Higgs field Φ, a complex scalar doublet field that couples to the fermions. Through the mechanism of spontaneous symmetry breaking, Φ obtains a non-zero vacuum expectation value,

$$\langle 0|\Phi^\dagger \Phi|0\rangle = \frac{v^2}{2} \tag{1.4}$$

which generates a Dirac mass term in the Lagrangian:

$$\mathcal{L}_{\text{mass}} = -\frac{v}{\sqrt{2}}\left(f_u \overline{u}_L u_R + f_d \overline{d}_L d_R + f_e \overline{e}_L e_R + f_{\nu_e} \overline{\nu_e}_L \nu_{eR} + \ldots\right) + \text{h.c.} \qquad (1.5)$$

The fermion masses are then given by

$$m_{\text{f}} = \frac{v}{\sqrt{2}} f_{\text{f}}, \qquad (\text{f} = u, d, e, \nu_e, \ldots)\,. \qquad (1.6)$$

The fermion mass Lagrangian couples the left-handed and right-handed fields together, breaking the chiral symmetry. The coupling constants f_{f}, and hence the fermion masses, must be determined from experiment. Present experimental evidence is consistent with all neutrino masses being equal to zero. The theory explains this by stipulating that the right-handed neutrino fields do not exist, so the neutrino terms in (1.5) vanish. An equivalent viewpoint is to require $f_{\nu_e} = f_{\nu_\mu} = f_{\nu_\tau} = 0$. The right-handed neutrino fields then have no physical manifestation whatsoever, and essentially do not exist. Neutrinos in the Standard Model are massless and must always have helicity -1 ($+1$ for anti-neutrinos).

1.2 Massive Neutrinos

It is possible that future experiments will show that neutrinos do in fact have mass. If so, massive neutrinos can be incorporated into the Standard Model without serious difficulty. The most straightforward way is to allow the ν_R fields to exist with $f_\nu \neq 0$ in (1.5). The neutrino becomes a massive Dirac particle, like the electron, with four distinct states: ν_L, ν_R, $\overline{\nu}_R$, and $\overline{\nu}_L$. The right-handed neutrino (and left-handed antineutrino) are sterile, i.e. they have no electroweak interaction. However, the chiral states of a massive particle are not solutions of the Dirac equation, so a free ν_R contains a small projection of the opposite chirality and hence may interact as a ν_L. Therefore all four states are physical.

Another possible scenario is to include a term of the following type in (1.5):

$$\mathcal{L}_{\nu\ \text{mass}} = m_\nu \overline{\nu}^c_L \nu_L + \text{h.c.} \qquad (1.7)$$

called a Majorana term. The superscript c signifies charge conjugation. It couples the left-handed neutrino to the right-handed antineutrino, implying that they are opposite helicity states of the same particle. This is allowed only for a neutral particle, otherwise it would violate conservation of electric charge. There is no need for a sterile neutrino in this model, only two states exist. The Dirac or Majorana nature of the neutrino can in principle be determined experimentally; a Dirac neutrino respects total lepton number conservation while a Majorana neutrino necessarily violates it by ΔL=2. Also, a Dirac neutrino is expected to possess a small magnetic moment, while a Majorana neutrino with a non-zero magnetic moment would violate CPT invariance.

More complicated models using Dirac and Majorana mass terms have been proposed. In the seesaw mechanism each generation contains a pair of Majorana neutrinos that couple to the Higgs sector in the following way:

$$\mathcal{L}_{\nu \text{ mass}} = \begin{pmatrix} \overline{\nu}_L^c & \overline{N}_L^c \end{pmatrix} \begin{pmatrix} 0 & m_D \\ m_D & M \end{pmatrix} \begin{pmatrix} \nu_L \\ N_L \end{pmatrix} + \text{h.c.} \tag{1.8}$$

with $m_D \sim m_e$ and $M \gg m_e$. The ν has weak isospin $\frac{1}{2}$ and N is a sterile singlet. When the matrix is diagonalized two mass eigenstates are obtained with masses m_D^2/M (the observed electron neutrino) and M. Such a mechanism could explain why $m_{\nu_e} \ll m_e$ in the context of a grand unified theory. In the Konopinski-Mahmoud model and its variations a neutrino and antineutrino from different generations, for example $\nu_{\mu L}$ and $\overline{\nu_{\tau R}}$, are combined into one Majorana neutrino, while $\nu_{\tau L}$ and $\overline{\nu_{\mu R}}$ form another; and the masses are degenerate. This is equivalent to a single four-component Dirac neutrino and is called a pseudodirac particle. There are no sterile states, but ν_L and ν_R have different dominant lepton flavor. This scheme could allow a large Majorana mass while suppressing neutrinoless double beta decay (Section 1.3) by cancellation.

The fermion mass eigenstates in (1.5) are in general not the same as the weak eigenstates that appear in (1.3). Such a coincidence would imply an unex-

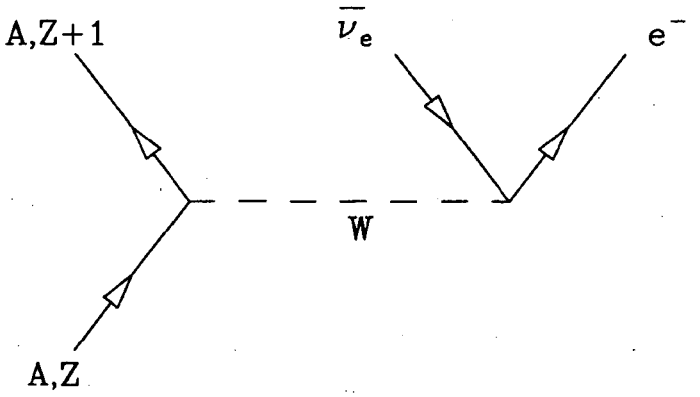

Figure 1.1: Nuclear beta decay. The electron and electron antineutrino share the available decay energy.

pected connection between the weak interaction and mass. In fact, we know from experiment that the quark weak states are related to the mass states by a unitary transformation, the Kobayashi-Maskawa (KM) matrix. A similar situation should occur in the lepton sector if neutrinos have mass. If the weak flavors ($l = e, \mu, \tau$) are defined in the basis of the charged lepton masses, then the neutrino weak states can be written

$$|\nu_l\rangle = \sum_i U_{li} |\nu_i\rangle \tag{1.9}$$

where ν_i are the mass states ($i = 1, 2, 3$). U is the leptonic KM matrix. This leads to the very interesting possibility of neutrino mixing and neutrino oscillations.

1.3 Tests of Neutrino Mass

Probably the most accessible laboratory process that involves the neutrino is nuclear beta decay (see Figure 1.1). The mass of the emitted antineutrino will affect the shape of the observed beta energy spectrum:

$$\frac{dN(E, m_\nu)}{dE} \propto F(E, Z) pE\,(Q - E)\left[(Q - E)^2 - m_\nu^2\right]^{\frac{1}{2}}. \tag{1.10}$$

E, p are the beta's energy and momentum, Q is the total decay energy, and $F(E, Z)$ accounts for final state coulomb effects. Figure 1.2 shows a plot of a typical beta

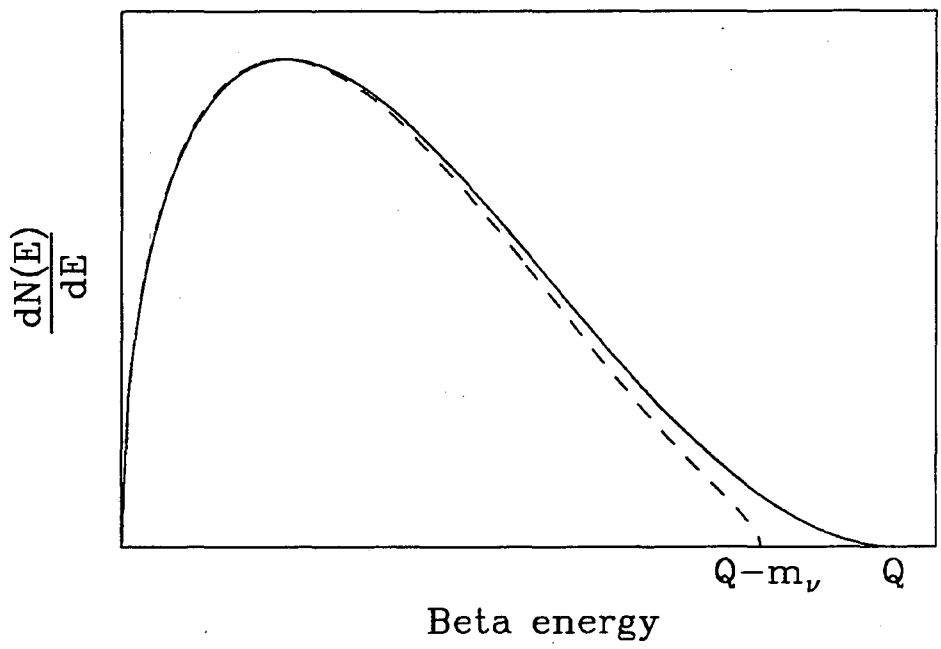

Figure 1.2: Fermi beta spectrum for $m_\nu \neq 0$ (dashed) compared to $m_\nu = 0$ (solid).

spectrum for $m_\nu \neq 0$ compared to $m_\nu = 0$. The maximum beta energy is reduced from Q to $(Q - m_\nu)$ and the slope of the spectrum becomes infinite at the endpoint. This would seem the easiest way to measure the electron neutrino mass.* However if $m_\nu \ll Q$ the observable effect is very close to the endpoint energy where relatively few events occur. The most ambitious attempts have studied the tritium beta spectrum ($Q = 18.6$ keV) with high-resolution magnetic spectrometers [5, 6, 7, 8]. These experiments see no evidence for neutrino mass, but unfortunately are all limited by an unexplained excess of events near the endpoint (a massive neutrino would cause a deficit of events there). The Particle Data Group's global upper limit is $m_{\nu_e} < 7.3$ eV (90% C.L.) [9].

The mass of the muon neutrino has been investigated by studying the kinematics of charged pion decay:

$$\pi^- \rightarrow \mu^- + \overline{\nu_\mu} \tag{1.11}$$

*When I refer to the mass of a flavor state I mean the mass state with the largest $|U_{li}|^2$ for that flavor. I am also assuming here that $m_\nu = m_{\overline{\nu}}$.

The neutrino mass can be determined from precise measurement of the pion and muon masses and momenta. The best quoted limit is $m_{\nu_\mu} < 270$ keV (90% C.L.) [10]. This number is highly dependent on the pion mass, which is presently a matter of some disagreement [11] so perhaps the limit should be higher. The tau neutrino mass can be derived in a similar way from the kinematics of various decay modes. The best limit is $m_{\nu_\tau} < 32.6$ MeV (95% C.L.) from tau decays into five hadrons [12].

There exist a number of even-A nuclei that are stable against beta decay but unstable against two beta decays through a virtual intermediate nuclear state. The Standard Model predicts this decay to occur with the emission of two betas and two antineutrinos ($\beta\beta2\nu$). The matrix element contains two W exchanges so the rate is extremely slow ($\sim 10^{20}$ years), but the process has been observed in several nuclei [13, 14, 15, 16]. Neutrinoless double beta decay ($\beta\beta0\nu$) is a competing process that is possible only if the electron neutrino has a Majorana mass (see Figure 1.3).* The right-handed antineutrino emitted in the initial beta decay will have a small projection of the opposite chiral state due to its mass. This left-handed state has electron neutrino flavor from the Majorana coupling, so it can be recaptured by the nucleus, causing the emission of a second beta. The sum energy of the betas from $\beta\beta0\nu$ must equal the decay Q-value. It can therefore be distinguished experimentally from $\beta\beta2\nu$, which has a continuous sum spectrum. A number of sensitive experiments have placed stringent upper limits on $\beta\beta0\nu$ rate [14, 15, 18] equivalent to an upper limit on the electron neutrino effective Majorana mass (the sum of the mass states weighted by the mixings) of ~ 1 eV. This limit can be evaded by a pseudodirac neutrino, which consists of a pair of Majorana neutrinos degenerate or nearly degenerate in mass. In that case two diagrams like Figure 1.3 will exist with the possibility of opposite CP parities

*A $\Delta L = 2$ right-handed weak current W_R can also initiate this decay mode, but a Majorana neutrino mass is still required [17].

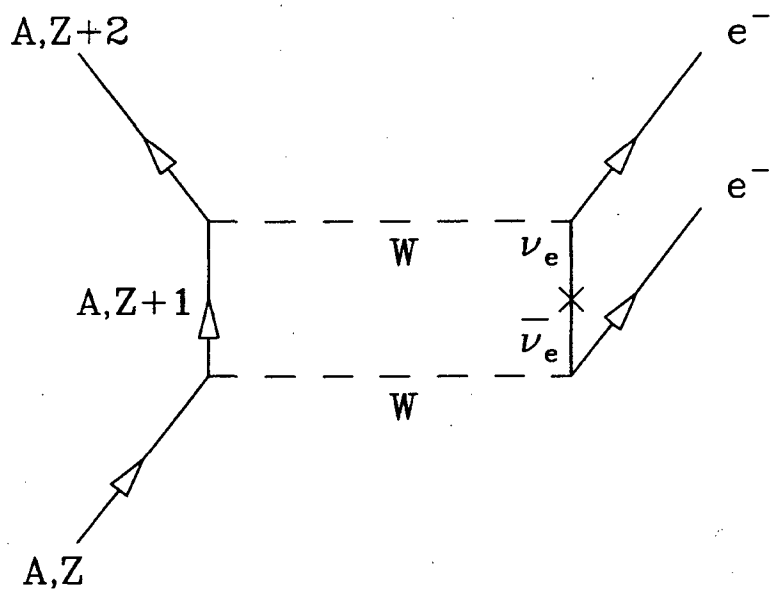

Figure 1.3: Neutrinoless double beta decay can occur only if the electron neutrino possesses a Majorana mass.

causing a cancellation.

As discussed earlier, if neutrinos have mass then they are expected to mix. Consider the simple case of two-component mixing. In addition to its dominant mass, ν_e would contain a small admixture of a different, possibly much larger mass (which would be dominant in ν_μ or ν_τ). The ν_e weak eigenstate would then be:

$$|\nu_e\rangle = \cos\theta|\nu_1\rangle + \sin\theta|\nu_2\rangle \tag{1.12}$$

where $\sin\theta$ and $\cos\theta$ are the approximate elements of the leptonic KM matrix and $|\nu_1\rangle$ and $|\nu_2\rangle$ are the mass eigenstates with masses m_1 and m_2. When a ν_e is created with a certain energy its two mass components will propagate with different wavelengths and interfere with each other coherently. It is easy to show that this causes an oscillation of lepton flavor. The probability that a neutrino initially in eigenstate ν_e will oscillate into a ν_x (the dominant flavor of ν_2) after travelling a distance l in a vacuum is given by:

$$P(\nu_e \rightarrow \nu_x, l) = \frac{1}{2}\sin^2 2\theta \left[1 - \cos\left(\frac{2\pi l}{L_{osc}}\right)\right] \tag{1.13}$$

with

$$L_{osc} = \frac{4\pi E_\nu}{m_2^2 - m_1^2} \tag{1.14}$$

In order to look for this phenomenon one must detect the neutrino, which is no easy matter. Neutrino oscillation experiments use strong neutrino sources, such as a reactor or intense pion beam, and large volume detectors. There are two main categories: "appearance" experiments where the opposite neutrino flavor is detected, and "disappearance" experiments where the detection rate of the original flavor neutrino oscillates as the source distance is varied. Flavor oscillation cannot distinguish between Dirac and Majorana masses. A composite exclusion plot of ν_e appearance and disappearance experiments is shown in Figure 1.4.

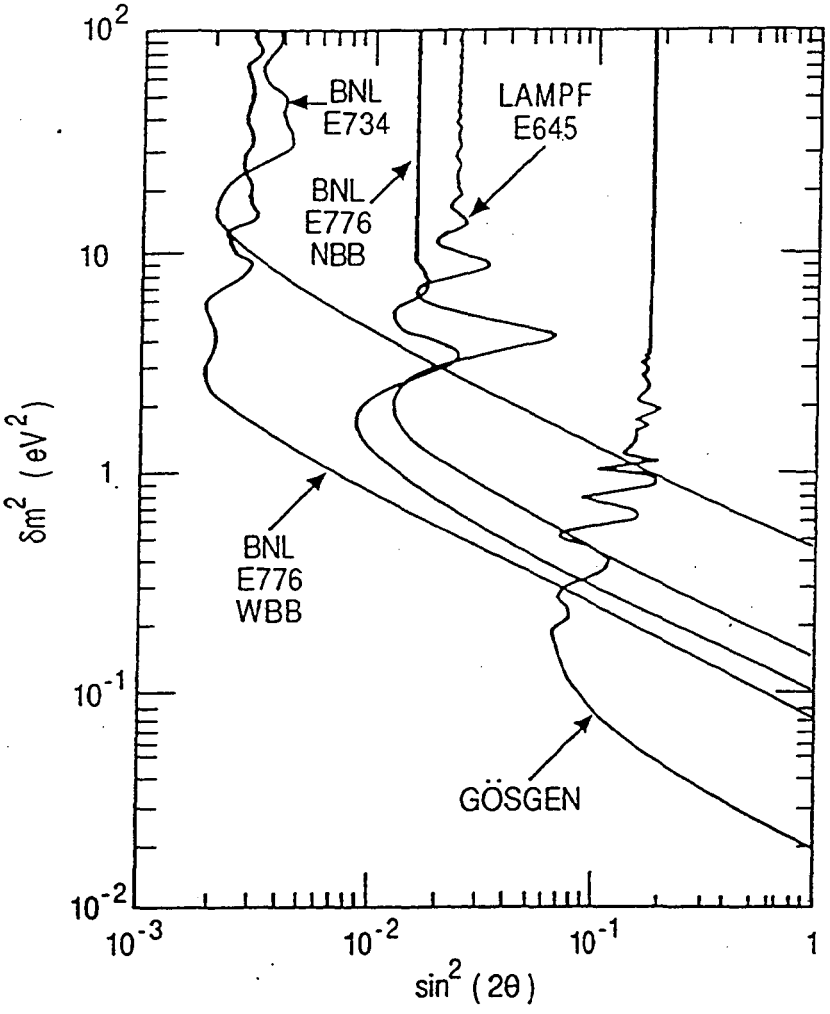

Figure 1.4: Composite exclusion plot, from [19], of ν_e appearance and disappearance experiments. These are equivalent if ν_e mixes primarily with ν_μ. The parameter space to the right of each contour is excluded at 90% C.L. The vertical axis is $\delta m^2 = m_2^2 - m_1^2$. See [20–23].

1.4 Kink Searches in Weak Decays

If neutrinos are massive and the flavors mix, a heavy mass state associated with ν_e will cause a characteristic kink in beta decay energy spectra. Suppose (1.12) is true and $m_1 \approx 0$, $m_2 \gg m_1$. An observed beta spectrum will be an incoherent superposition of the spectra (1.10) corresponding to $m_\nu \approx 0$ and $m_\nu = m_2$:

$$\frac{dN(E)}{dE} = \cos^2\theta \frac{dN(E,0)}{dE} + \sin^2\theta \frac{dN(E,m_2)}{dE} \tag{1.15}$$

For $E > Q - m_2$ the heavy neutrino is energetically forbidden and the spectrum is identical to the massless neutrino spectrum. There is a kink (slope discontinuity) at $E = Q - m_2$, and below that point the relative amplitude rises to $1 + \tan^2\theta$. The values of m_2 and θ will be the same in all beta spectra having $Q > m_2$. It is convenient to write (1.15) as the product of the massless neutrino spectrum and a massive neutrino shape factor $S(E)$,

$$\frac{dN(E)}{dE} \propto \frac{dN(E,0)}{dE} S(E) \tag{1.16}$$

with

$$\begin{aligned} S(E) &= 1 + \tan^2\theta \left[1 - \frac{m_2^2}{(Q-E)^2}\right]^{\frac{1}{2}} \qquad \text{for} \quad E \leq Q - m_2 \\ &= 1 \qquad\qquad\qquad\qquad\qquad\qquad\quad \text{for} \quad E > Q - m_2. \end{aligned} \tag{1.17}$$

Figure 1.5a shows a plot of $S(E)$ normalized in the region $E > Q - m_2$. It gives a clear picture of the effect of the massive neutrino admixture. However in a typical experiment the normalization and Q will be treated as free parameters and determined by a least-squares fit over a wide energy region; with each point weighted by its statistical uncertainty. That normalization of $S(E)$ is shown in Figure 1.5b. The data points of an experimental beta spectrum containing a massive neutrino admixture, divided by the best fit theoretical spectrum with $m_\nu = 0$, will lie along this curve. The curve diverges near the endpoint because Q

will be underestimated if a massive neutrino admixture is present in the data but not included in the fit.

A Kurie plot is often used to analyze an experimental beta spectrum, especially to determine the endpoint energy. It is defined by:

$$K(E) = \left[\frac{\frac{dN(E)}{dE}\Big|_{\text{exp}}}{pEF(E_e, Z)} \right]^{\frac{1}{2}}. \tag{1.18}$$

The Kurie plot of an allowed spectrum (with no massive neutrino) is a straight line. Figure 1.6 shows the effect of $S(E)$ on the Kurie plot of the spectrum. The asymptotic slope above the kink differs from the slope below the kink.

Electron capture by the nucleus is another decay process that can reveal information about neutrino mass. In the lowest order decay an atomic electron is captured by the nucleus and a monoenergetic neutrino and x ray are emitted. There is an order α correction to this process in which the incoming electron emits an internal bremsstrahlung (IB) photon (see Figure 1.7). The neutrino and photon share the available decay energy, resulting in a continuous photon spectrum similar to a beta spectrum. For capture from the $1s$ shell:

$$\frac{dN(k, m_\nu)}{dk} \propto k\,(q_{1s} - k) \left[(q_{1s} - k)^2 - m_\nu^2 \right]^{\frac{1}{2}} R_{1s}(k) \tag{1.19}$$

where k is the IB photon energy; q_{1s} is the decay Q-value minus the $1s$ electron binding energy; and R_{1s} is a correction factor that accounts for the influence of the nuclear Coulomb field on the intermediate electron. It is clear by comparing (1.19) to (1.10) that the effect of neutrino mass on the shape of the spectrum is the same. One difference is that beta decay emits an antineutrino while a neutrino is emitted with electron capture. CPT invariance requires that a particle and its charge conjugate antiparticle have identical mass. However it has not been positively established that the particles we call neutrino and antineutrino are actually charge conjugate states; so it is possible that the masses are different. Nevertheless, in the absence of contrary evidence it is reasonable to assume that they are charge

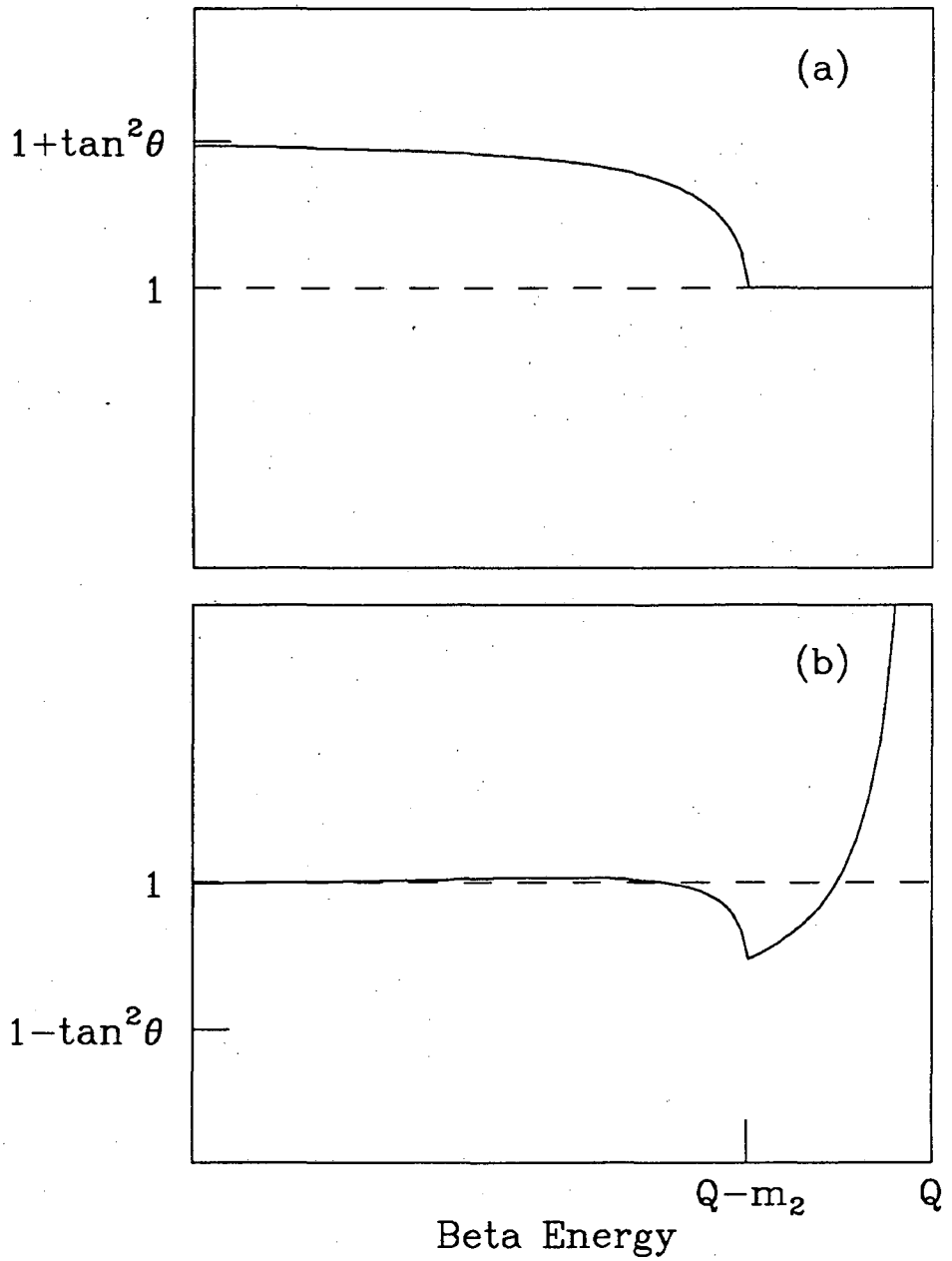

Figure 1.5: (a) The massive neutrino shape factor $S(E)$ for a beta decay spectrum normalized in the region $E > Q - m_2$. There is a kink (slope discontinuity) at $E = Q - m_2$ and a rising amplitude below that point. (b) The same $S(E)$ with the normalization and Q determined from a least squares fit over the entire energy region shown (the expected experimental shape factor).

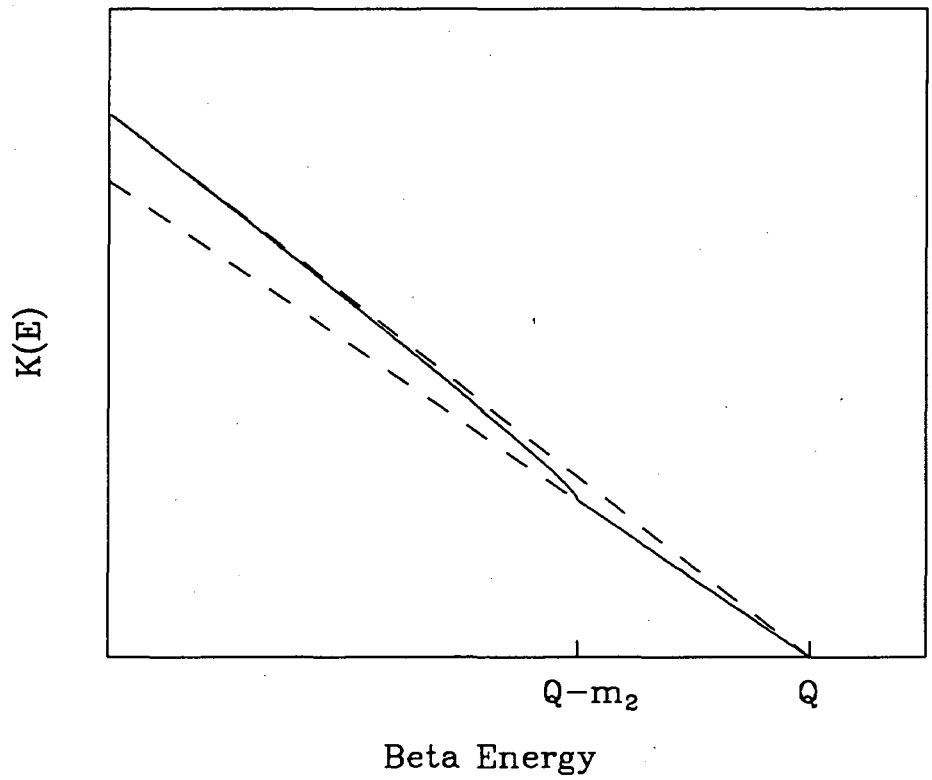

Figure 1.6: The effect of $S(E)$ on the Kurie plot of a beta spectrum (solid). The slope of each component is different (dashed).

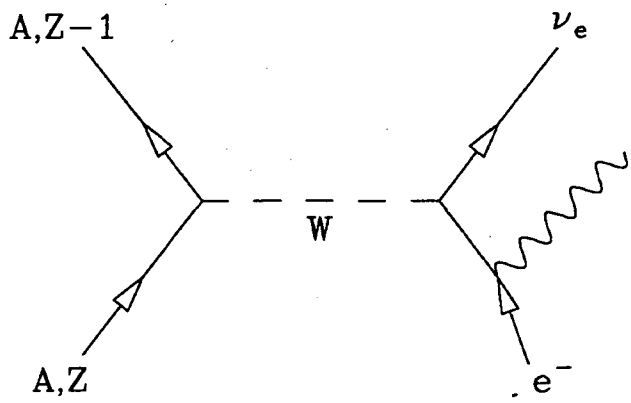

Figure 1.7: Internal bremsstrahlung from electron capture (IBEC). The photon and neutrino share the available decay energy.

conjugates and have the same mass. A massive neutrino shape factor that is observed in beta decay should then also be exhibited in IBEC spectra:

$$\frac{dN(k)}{k} \propto \frac{dN(k,0)}{dk} S(k) \tag{1.20}$$

with

$$\begin{aligned} S(k) &= 1 + \tan^2\theta \left[1 - \frac{m_2^2}{(q_{1s}-k)^2}\right]^{\frac{1}{2}} \qquad \text{for} \quad k \leq q_{1s} - m_2 \\ &= 1 \qquad\qquad\qquad\qquad\qquad\qquad\quad \text{for} \quad k > q_{1s} - m_2 \end{aligned} \tag{1.21}$$

1.5 Implications of Neutrino Mass

Neutrino mass has a number of profound implications for astrophysics and cosmology. Neutrinos are very abundant, so even a tiny mass will contribute significantly to the total mass of the universe. The matter density of the universe is normally parameterized by the dimensionless quantity Ω:

$$\Omega \equiv \frac{\rho}{\rho_c} \tag{1.22}$$

where ρ_c is the density needed to make the universe cosmologically flat. Dynamical evidence from the observed distribution of galaxies implies that $\Omega \geq 0.1$. Lower limits on the age of the universe based on the age of the Earth and stars require [24] $\Omega h_0^2 \leq 1.0$, where h_0 (=0.5–1.0) is the Hubble constant $H_0/100$ km s^{-1} Mpc^{-1}. In addition, observational estimates of the deceleration parameter suggest that $\Omega \leq 2$. We can reasonably conclude that

$$0.1 \leq \Omega \leq 2. \tag{1.23}$$

However, the physics of cosmological expansion suggests that $\Omega \sim 1$ is very unlikely (the flatness problem) unless $\Omega = 1$, which is the case in the inflationary model [25]. The best measurements of the luminous matter in the universe give $\Omega_{lum} \sim 0.01$ so most of the matter must be dark. Primordial nucleosynthesis calculations indicate

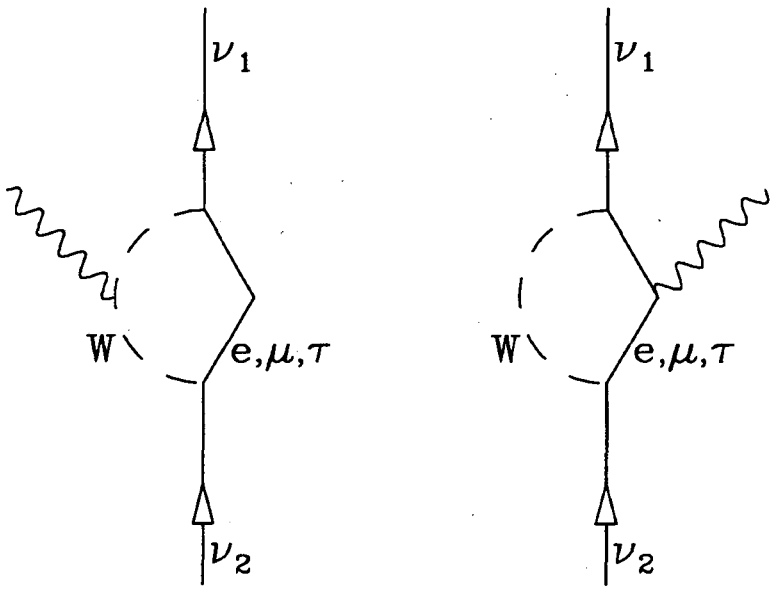

Figure 1.8: Radiative decay of a massive neutrino.

that the total baryonic matter cannot exceed $\Omega_{bar} \sim 0.035$ [26]. One is drawn to the possibility that neutrino rest mass accounts for the difference. If so, and if $\Omega = 1$, then calculations of relic neutrino densities can be used to determine the sum of neutrino masses [27]:

$$\begin{aligned} \sum_l m_\nu &= 45h_0^2 \text{ eV} \quad \text{for Dirac neutrinos} \\ &= 90h_0^2 \text{ eV} \quad \text{for Majorana neutrinos} \end{aligned} \tag{1.24}$$

where the sum is over all light stable flavors. If other non-baryonic dark matter exists then (1.24) is an upper limit. Extremely massive ($\sim$ GeV) neutrinos evade this limit.

If the massive neutrinos are unstable then (1.24) will be modified. With flavor mixing, the minimally extended Standard Model predicts that the heavier mass states will decay radiatively into the lighter ones (Figure 1.8). This type of diagram is suppressed by the GIM factor $(m_\tau/m_W)^2$ so the decay rate is extremely small [28]:

$$\Gamma \approx \left[\frac{m_{\nu_2}}{30\text{eV}}\right]^5 |U_{\tau 2}^\dagger U_{\tau 1}|^2 \quad 10^{-29} y^{-1}. \tag{1.25}$$

The mean life is greater than the age of the universe unless $m_2 > 150$ keV. If $m_2 > 1$ MeV it can instead decay into a lighter neutrino and an e^+e^- pair, which is a much faster process. Otherwise a neutrino with a mass that exceeds the limit of (1.24) will require a more rapid decay than known processes will allow, which will in turn require new physics to explain.

There is a well-known deficit in the detection rate of neutrinos produced by the sun. Bahcall has used detailed solar models to calculate the energy dependent flux of solar neutrinos at the Earth [29], about 6.5×10^{10} cm^{-1} s^{-1} total. Over a twenty-year period, Davis *et al.* have detected an overall rate of 2.1 ± 0.9 SNU in their ^{37}Cl neutrino detector (a SNU equals 10^{-36} s^{-1} interactions per target atom), verses a predicted rate of 8.0 ± 2.6 SNU [30]. The quoted uncertainties are 3σ. Recent experiments using H_2O and ^{71}Ga detectors have confirmed a solar neutrino deficit [31, 32, 33]. The operating detectors are primarily sensitive to electron flavor neutrinos only. A possible explanation for the missing solar neutrinos is that they have mass and a significant fraction oscillate into muon or tau flavor before they reach the Earth. Vacuum oscillation (1.13) is not a satisfying solution since it would require a fine-tuning of $\Delta(m^2)$ to the Earth-Sun distance. It is also unsatisfying on theoretical grounds; it requires tiny mass differences ($\Delta(m^2) \sim 10^{-12}$ eV^2 for L_{osc}= 1 A.U.) and large mixing angles while the quark sector is characterized by large mass differences and small mixing angles. Inside the sun however, refraction of the neutrino wave function due to its interaction with matter can enhance the oscillation (MSW effect [34]). This effect is independent of distance and a solution to the solar neutrino problem can be obtained with reasonable mixing parameters ($\Delta(m^2) \sim 10^{-5}$ eV^2, $\sin\theta \sim 0.03$–0.07 [35]).

The Standard Model predicts that a massive Dirac neutrino will possess a small magnetic moment [36]:

$$\mu_\nu = \left(\frac{3}{\sqrt{2}}\right) \frac{G_F m_\nu m_e}{4\pi^2} \mu_{Bohr}. \tag{1.26}$$

It is unlikely that this could ever be measured in a laboratory experiment, but it

may have astrophysical importance. For example, the rate of energy release from an exploding supernova is limited by the transport of neutrinos; they are trapped inside the dense expanding matter. A magnetic dipole interaction can cause a neutrino to flip helicity into the mostly sterile right-handed state, which will then diffuse more rapidly through the supernova. The overall neutrino transport is enhanced and the supernova cools more rapidly. The observed neutrino pulse duration from supernova 1987A leads to the limit [37]:

$$\mu_\nu < 5 \times 10^{-13} \mu_{Bohr} \tag{1.27}$$

A better limit on the Dirac mass can be obtained by considering weak scattering in the supernova, which can also cause a helicity flip. In this case the Supernova 1987A neutrino pulse gives the limit [38]:

$$m_{\nu,Dirac} < 30 \quad \text{keV} \tag{1.28}$$

The time-energy dependence of the supernova neutrino pulse can in principle be used to determine the electron neutrino mass (the observed signals were presumably all electron neutrino flavor). This is based on the simple kinematical argument that mass will cause a velocity spread in neutrinos of different energy. Bachall and Glashow claim a limit of $m_{\nu_e} < 11$ eV [39]. However, the statistical sample in these data is very small.

Finally, neutrino mass leads to the possibility of CP violation in the lepton sector. CP symmetry is known to be violated in K meson decay. The Standard Model accounts for this through the KM matrix. A general 3×3 unitary matrix contains three rotation angles and six phases. In the KM matrix, five of these phases refer to the relative phases between the quark wave functions and are arbitrary and physically meaningless. The remaining phase is non-trivial and can explain the observed CP violation. The existence of a leptonic KM matrix could lead to a similar breaking of CP symmetry in purely leptonic processes.

Chapter 2

The 17 keV Neutrino

2.1 Simpson's Experiment

The saga of the 17 keV neutrino began in 1985 when John Simpson of the University of Guelph, Canada, reported evidence of a low energy distortion in the tritium beta decay spectrum [40]. The experiment consisted of a Si(Li) detector in which tritium had been implanted at energies from 10.5 to 15 MeV, to a depth of 0.25 to 0.45 mm. This depth was sufficient to stop all the tritium betas and bremsstrahlung photons, yielding a fully calorimetric beta spectrum. The original motivation of the experiment was to study the spectral shape near the endpoint (18.6 keV). However, a divergence was observed at the other end of the spectrum, at an energy of 1.5 keV and below (Figure 2.1). Simpson found that the size and shape of this divergence could be adequately fit by including a massive neutrino component with $m_2 = 17.1 \pm 0.2$ keV and $\sin^2\theta = 0.03 \pm 0.01$ (see Equation (1.15)). This experiment drew considerable interest but the result was not widely accepted mainly for reasons of systematics: the x-ray energy calibration of the detector did not extend below 6 keV and had to be extrapolated down to the energy of the neutrino kink; and the extent of pulse-height defects caused by radiation damage during ion implantation could not be determined at low energies.

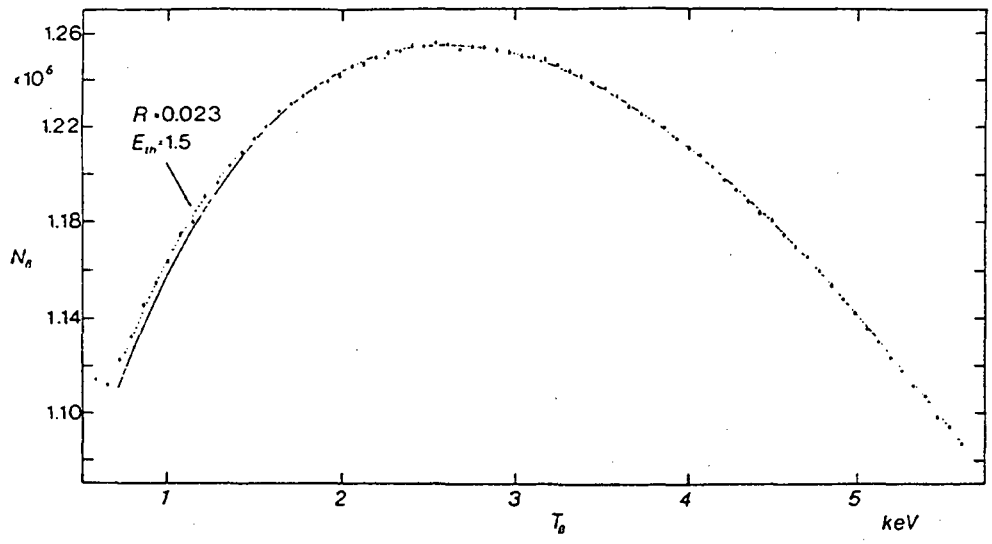

Figure 2.1: Data from [40], showing the low energy portion of the measured tritium beta spectrum compared to the theoretical massless neutrino spectrum (solid line).

Haxton [41] quickly pointed out that conventional approximations used to treat exchange terms in the sudden approximation and electronic screening corrections are only valid for beta energies with wavelengths much smaller than the atomic scale. For a beta energy of 1 keV, $\lambda_e = 0.07$Å, which is 24% of the Bohr radius of He (0.26Å). He concluded that the exchange correction is still quite small but a proper treatment of screening corrections could account for the low energy divergence in Simpson's spectrum. Several authors [42, 43, 44] calculated the appropriate screening potential. When Simpson reanalyzed his data with these corrections he found that the best value of $\sin^2\theta$ was reduced to 0.5–1.6%, but the observed distortion could not be completely accounted for by low energy atomic effects.

2.2 Early Negative Results

In the fall of 1985, only months after Simpson's result was published, five different groups reported negative results from searches for a 17 keV neutrino signal in the

beta spectrum of ^{35}S. This isotope has an endpoint energy of 167 keV, putting the kink at 150 keV, much higher than the 1.5 keV position in tritium. This is an advantage because atomic corrections which were relevent for tritium are negligible and experimental systematics are more easily understood at the higher energy. The disadvantage is that only 0.18% of beta events fall within 17 keV of the endpoint.

Similar experiments at Princeton [45], Russia (ITEP) [46], and Caltech [47] utilized magnetic spectrometers to measure the ^{35}S spectrum. Upper limits on $\sin^2\theta$ for a 17 keV neutrino of 0.4% (99% CL), 0.17% (90% CL), and 0.3% (90% CL), respectively, were reported. Due to uncertainties in the response of these spectrometers, the observed spectra all deviated systematically from the predicted one. To accomodate this problem, the Princeton and Russian groups each multiplied their spectrum by a shape correction: a second order polynomial in energy with coefficients determined by fitting the data. It was claimed that this process would not affect the sensitivity to a massive neutrino: "the systematic error in our procedure is likely neither to simulate a neutrino mass kink nor to cover up such a kink because the correction is a smooth function of the energy." [45]. This claim was later criticized by Simpson and others (see Section 2.5). The Caltech group, which had the lowest statistics, did not require such a correction function.

Datar *et al.* in Bombay [48] used a cooled, 3-mm-thick Si(Li) detector to collect the beta spectrum from a collimated external source of ^{35}S. An upper limit of $\sin^2\theta < 0.6\%$ (90% CL) was reported, which excludes Simpson's original result but not the revised result after correcting for atomic effects. Ohi *et al.* at INS Tokyo [50] used a pair of cooled, 7-mm-thick Si(Li) detectors with a ^{35}S source sandwiched in between (Figure 2.2). It is well known that about 13% of normally incident betas (even more with an uncollimated source) will back-scatter out of a silicon detector, depositing less than their full energy [49]. This arrangement allowed them to veto back-scattered events, mitigating this problem. Unfortunately, it introduced

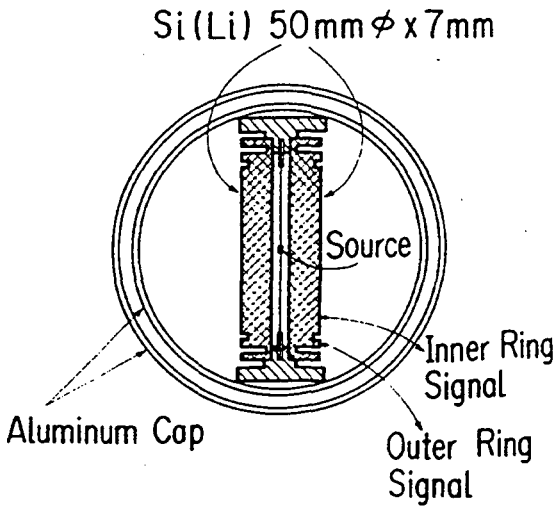

Figure 2.2: Side view of the source-detector configuration in Ohi *et al.* [50].

another problem: some betas will back-scatter from the veto detector depositing too little energy to generate a veto signal. Thus the total number of back-scattered events where the veto detector energy is below threshold (typically several keV), and the remaining energy is collected in the energy detector, is greater compared to a single detector design. This is significant when the high energy part of the spectrum is of interest, as in this case. An upper limit on $\sin^2\theta$ of 0.15% (90% CL) for a 17 keV neutrino was reported. However, it is apparent from Figure 2.3 that while the experimental data was normalized over the region 120–160 keV, the massive neutrino function $S(E)$ is shown normalized from ~150–160 keV (above the kink position), so the validity of this limit is questionable. In fact, in 1986 Simpson published a paper in which he reanalysed the data from [50], showing that a distortion at 150 keV is consistent with emission of a 1–2% 17 keV neutrino when the data is also normalized above 150 keV (Figure 2.3) [51]. He also criticized their analysis for fitting the massive neutrino after the other parameters had been fixed, instead of properly fitting all free parameters simultaneously.

In 1987 a search for a 17 keV neutrino in the beta spectrum of ^{63}Ni was

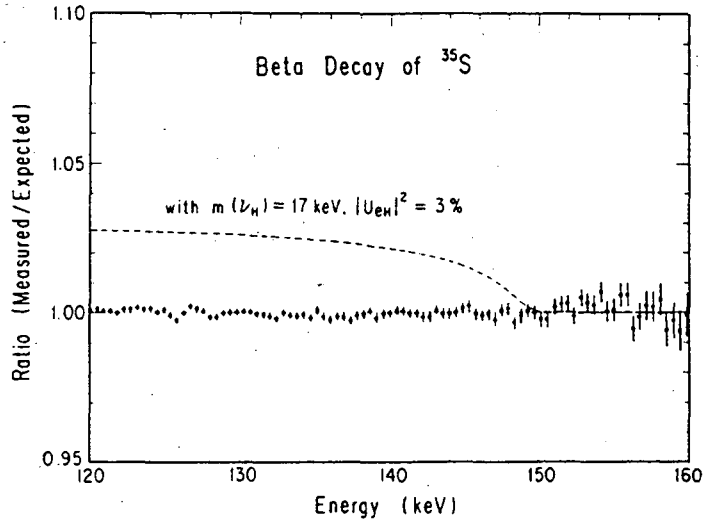

(a)

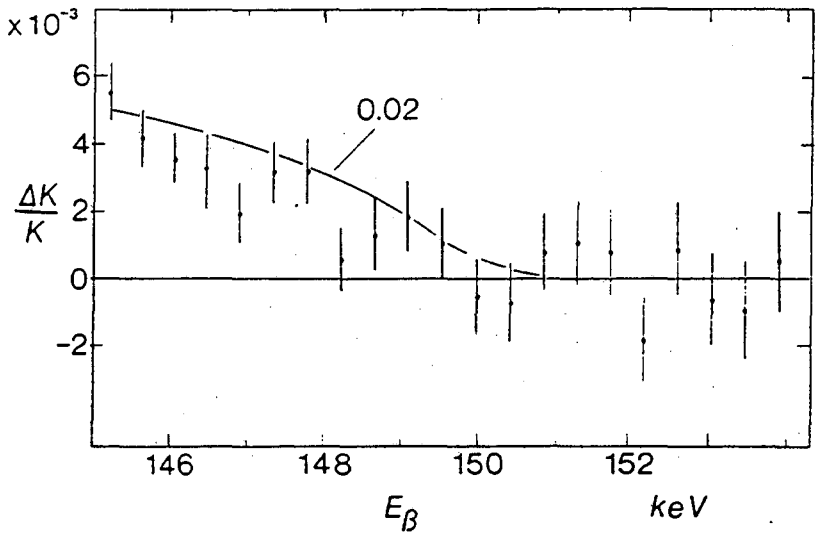

(b)

Figure 2.3: (a) Data/fit of Ohi *et al.* [50]. (b) Simpson's analysis of the same data showing support for the 17 keV neutrino (normalization taken above 150 keV) [51].

completed by Hetherington *et al.* using the $\pi\sqrt{2}$ magnetic spectrometer at Chalk River, Canada [52]. ^{63}Ni has an endpoint energy of 67 keV, lower than that of ^{35}S, resulting in better resolution and statistics at the kink position, yet high enough to avoid the low energy effects that were problematic in tritium. To enhance the count rate, a large area multiple strip source was employed, with an array of 22 proportional counters at the opposite focus, six of which were blocked off to function as background monitors. Numerous systematic effects were studied and described in detail in this impressive paper. An additional shape factor, linear in energy, was needed to correct for systematic distortion. Both a wide range scan (26–67 keV) and a narrow range scan (46–54 keV) were performed (Figure 2.4) and analyzed separately. The narrow range analysis put an upper limit of $\sin^2\theta < 0.44\%$ (90% CL) on a 17 keV neutrino.

2.3 The 17 keV Neutrino Returns

By late 1988, with a number of negative reports contradicting Simpson's experiment (the only positive report), the 17 keV neutrino seemed sufficiently dead. In 1989 Simpson and his student Andrew Hime powerfully brought it back to life with a pair of papers describing two new results supporting the massive neutrino and soundly criticizing the negative experiments [53, 54].

In the first experiment a cooled Si(Li) detector was used to collect the beta spectrum from an external source of ^{35}S. This arrangement was very similar to the one of Datar *et al.* [48] except collimators were not used and the statistical sample was a factor of eight larger. The data from 110–166 keV were fit to the theoretical spectrum, with no shape corrections needed, yielding a best fit of $m_2 = 16.9 \pm 0.4$ keV and $\sin^2\theta = 0.73 \pm 0.09 \pm 0.06\%$.

Simpson and Hime criticized the use of quadratic shape corrections in the Princeton [45] and Russian [46] magnetic spectrometer experiments. They argued

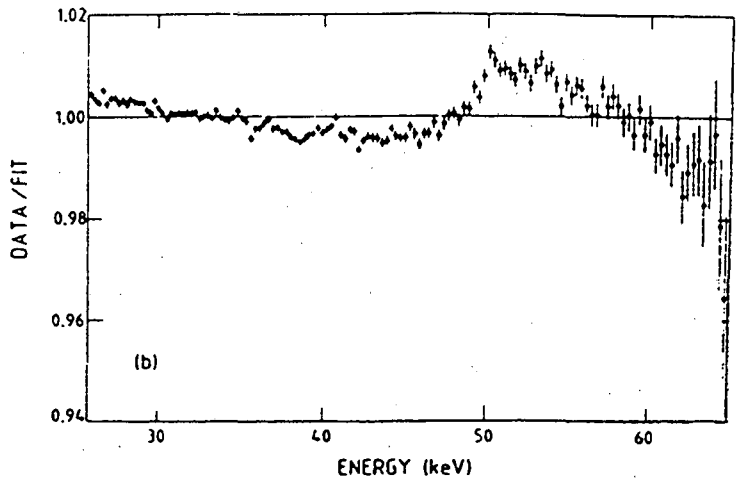

(a)

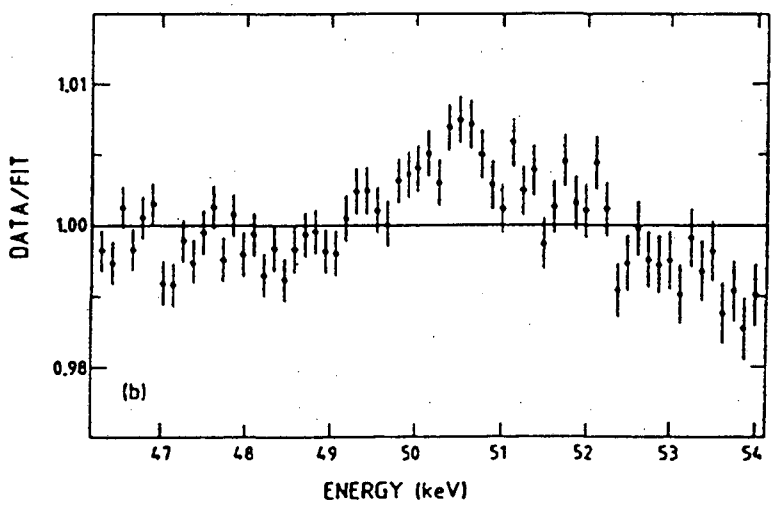

(b)

Figure 2.4: Data/fit including a 17 keV neutrino with $\sin^2\theta = 0.03$ from the Chalk River experiment [52]. (a)Wide range scan. (b) Narrow range scan.

that the linear and quadratic coefficients used in these two experiments are large enough to preclude ruling out a 0.8% 17 keV neutrino. They also criticized the Chalk River experiment [52] on similar grounds for using an excessively large linear correction. The Caltech ^{35}S experiment [47] did not use such a shape correction. However, Simpson and Hime pointed out that the Caltech measured detector response for ^{139}Ce internal conversion electrons indicates a back-scatter fraction of 60%, 4 times larger than that expected for normally incident electrons [49]. They concluded that this probably means some systematic problem was not accounted for, putting their result in question. The paper also criticized [48] on the grounds of low statistics and Ohi *et al.* [50] for the reasons previously discussed (see Section 2.2).

In the second paper, Hime and Simpson reported an improvement on the original tritium experiment. A 7-mm-thick hyperpure germanium detector was implanted with tritium to a depth of 0.28–0.32 mm. The advantage of germanium over silicon is that defects due to radiation damage can be removed by low temperature annealing ($\leq 200°C$) without diffusing out the tritium. The efficacy of the annealing process was monitored with gamma ray scans, and it was shown to be successful. A low energy calibration was obtained in a clever way by flouresc-ing various elements to produce 9.9–19.7 keV x rays, and calibrating with the Ge x-ray escape peaks from these lines. This provided an energy calibration down to 1.3 keV, below the kink position. After the best available low energy atomic corrections for tritium were included, the data exhibited a low energy divergence very similar to that of the original experiment. The authors quote a best fit of $m_2 = 16.9 \pm 0.1$ keV and $\sin^2\theta$ =0.6–1.6%.

The heavy neutrino gained momentum in 1991 as a series of new positive results appeared. The first truly independent result showing support for the 17 keV neutrino came from the group at Lawrence Berkeley Laboratory studying a ^{14}C-doped germanium detector [55]. This experiment is discussed in detail in Chapter

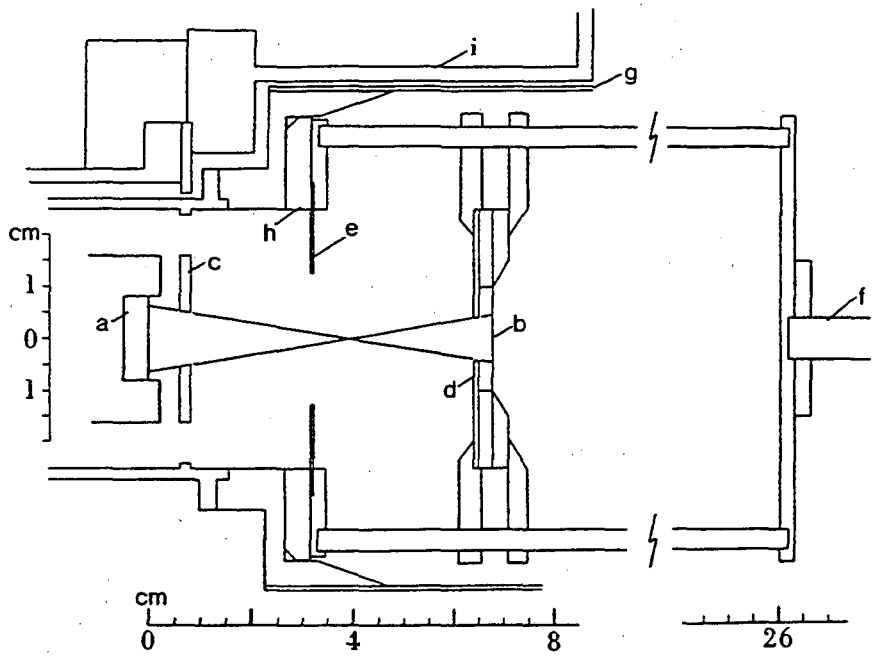

Figure 2.5: Oxford beta spectrometer [56-58]. (a) Si(Li) detector, (b) source substrate, (c) Al detector aperture, (d) Cu source aperture, (e) Al anti-scatter baffle, (f) linear motion feed-through, (g) liquid nitrogen cryo-panel, (h) teflon centering ring, (i) vacuum chamber.

3. Hime, who had moved to Oxford, and Jelley reported new results using ^{35}S and ^{63}Ni [56, 57, 58]. The apparatus used was similar to the one at Guelph [53] except that a set of aluminum and copper collimators were employed to restrict the detected betas to normal incidence (Figure 2.5). These collimators were beveled to minimize the probability of betas scattering from their edges. Normal incidence reduced back-scattering from the Si(Li) detector, and simplified treatment of this effect in the analysis. The beta response function of the detector was measured using K-shell conversion electron lines from ^{57}Co and ^{109}Cd (62.5, 115.0, and 129.4 keV) and extrapolated to the fit energy region (120–170 keV). The effects of back-scattering and energy loss in the thin gold detector window were studied using these lines and Monte Carlo calculations. Two high-statistics runs with slightly different geometries were collected using the ^{35}S source. Analyses of both runs showed

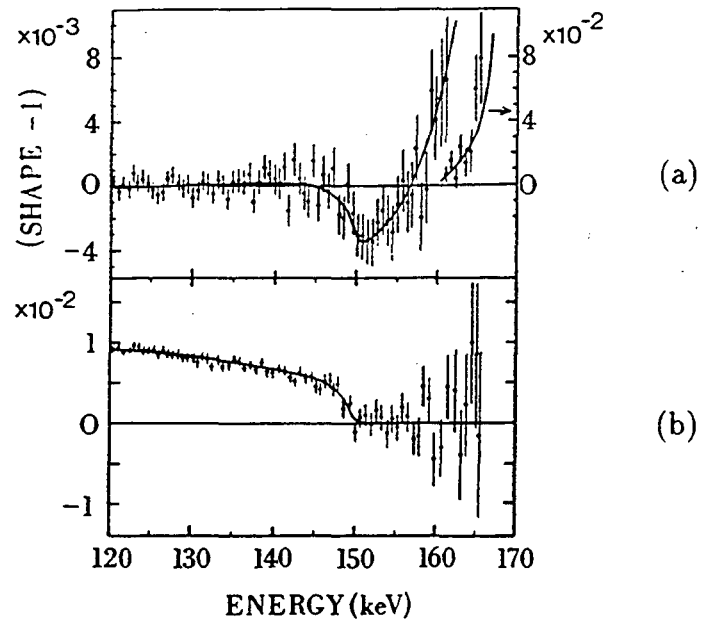

Figure 2.6: ^{35}S [56] data/fit with no massive neutrino component (a) normalized from 120–167 keV (b) normalized from 150–167 keV, showing strong evidence for a 17 keV neutrino kink at 150 keV.

strong evidence in favor of the 17 keV neutrino, and gave a best value of $\sin^2\theta = 0.0084 \pm 0.0006 \pm 0.0005$ (Figure 2.6). The ^{63}Ni data also supported the presence of a 17 keV neutrino, but the statistics were lower and systematic uncertainties in the back-scatter tail were more problematic due to the lower endpoint ($E_{\text{kink}}/E_{\text{endpoint}}$ is lower compared to ^{35}S). A result of $\sin^2\theta = 0.0099 \pm 0.0012 \pm 0.0018$ was quoted. One item of possible concern is that the ^{35}S source was made from a precipitate of $BaSO_4$, while the ^{63}Ni and conversion line sources were made from hydroxides. If energy losses in these sources were significantly different, the detector response function used would have been incorrect. In fact, energy loss in the source was not included in the response function analysis at all. Hime argued that the sources were thin enough so that any possible difference would be insignificant [59].

2.4 IBEC Experiments

As discussed in Chapter 1, internal bremsstrahlung from electron capture (IBEC) photon spectra can be used to study the electron neutrino mass. This approach is complimentary to beta decay, which involves the electron antineutrino. The spectral effect is essentially the same, although the experimental issues are quite different. A photon spectrum is most effectively measured using a large volume solid-state detector. Source scattering is not a serious problem, so large source volumes can be used as well. The main disadvantage is that photon scattering in the detector and surrounding materials is unavoidable and the scattered photon response function is quite complex. The IBEC theoretical shape is also more complicated than that of beta decay, due to capture from different electronic states. The first 17 keV neutrino experiment to use the IBEC method was undertaken by a group at CERN [60]. They produced a source of ^{125}I (K shell IBEC endpoint of 146 keV) and counted it with a pair of planar Ge detetctors. The statistics were rather low, and they were able to establish an upper limit of $\sin^2\theta < 0.02$ (98% CL).

In 1987, Žlimen *et al.* in Zagreb studied an ^{55}Fe IBEC spectrum collected with a 56-cm^3 Ge(Li) detector [61]. To avoid the complications of determining the response function and efficiency over a wide range of energies, they restricted their analysis to 197.5–213.5 keV, and extrapolated the detector efficiency function from the data above this region. They claimed an upper limit of $\sin^2\theta < 0.007$ (3σ) for a neutrino in the mass range 16.4–17.4 keV. This limit was probably overstated because the uncertainty inherent in their method of treating the efficiency was not included, and also because the χ^2 minimum was taken at a negative (unphysical) value of $\sin^2\theta$. The same group also studied the photon spectrum of ^{71}Ge (225 keV endpoint), and in 1991 reported the first positive evidence for a 17 keV neutrino in an IBEC spectrum [62]. In this experiment great pains were taken to determine the response function and efficiency over a wide range of energy. The detector

response was measured using a number of gamma sources and fit to a twelve-parameter function. The photopeak efficiency was similarly measured and fit to a three-parameter function. These parameters were then interpolated to achieve a continuous energy-dependent response. Furthermore, a quadratic polynomial was included to correct this function using the IBEC data above the kink energy. When the analysis was complete, the best fit required a 17.2 keV neutrino with $\sin^2\theta = 0.0160 \pm 0.0053$.

Later in 1991, two groups reported results from IBEC experiments that favored neutrino masses other than 17 keV. The LBL group studied the ^{55}Fe spectrum and found a preference for a 21 keV neutrino with a mixing of 0.0085 in their data [63]; however they pointed out that the kink position was strongly dependent on parameters used in their efficiency function, which was determined from test source data. A group in Buenos Aires found a best fit of 14 keV for a massive neutrino in the initial analysis of their ^{71}Ge spectrum [64] (this result was later retracted).

2.5 An Experimental Controversy

By the end of 1991 the 17 keV neutrino had attracted a great deal of attention and the experimental controversy was at its height. A summary of the experiments is given in Table 2.1. The numbers of positive and negative results were about equal; although the negative camp comprised nine different groups around the world, while Simpson and Hime accounted for most of the affirmative side. A weighted world average of the positive experiments gives m_2=16.95 keV and $\sin^2\theta$=0.93%. A fit of these points to the average using the quoted errors yields a χ^2_ν of 0.17 for the mass and 1.48 for the mixing, remarkably good agreement considering the variety of techniques and isotopes used. Simpson, Hime, and others argued quite effectively that several of the negative experiments were weakened by systematic problems

[45, 46, 47, 50], three lacked the sensitivity to rule out their result [48, 60, 61], and two of them were interpreted as actually supporting the massive neutrino [50, 46]. Yet, many observers still felt that so many groups failing to see the effect was sufficient cause for doubt. Some detractors noted that the positive results were all obtained using silicon or germanium detectors, and suggested that some solid state effect may be responsible; although it was difficult to conceive of a single systematic effect that could cause the same phenomenon in the different isotopes and techniques used.

One of the key issues at this stage was the use of arbitrary functions as shape corrrections to improve the quality of fits, required by all but one of the magnetic spectrometer experiments. In the early experiments, it was claimed that because a massive neutrino produces a kink in the spectrum, use of a smooth correction function in the analysis would not reduce the sensitivity to this effect. Later, Simpson and others correctly pointed out that when a wide-range region of a spectrum is fit, most of the statistical sensitivity to the massive neutrino shape function S(E) comes from its global shape rather than the local effect of the kink itself. This is best illustrated by considering the beta spectrum Kurie plot. Figure 2.7a shows the Kurie plot of a beta spectrum that contains a massive neutrino component (the shape has been greatly exaggerated for clarity). The slope above and below the kink are different. The best fit (minimum χ^2) Kurie plot without a massive neutrino is shown with no shape correction (dashed line), and a quadratic shape correction with coefficients determined from the fit (solid line). This shape correction accomodates much of the difference in slope, reducing the sensitivity to the effect (Figure 2.7b). When a neutrino admixture of only 1% is considered, the difference is crucial. This was demonstrated analytically by Bonvincini [65], who also performed a series of Monte Carlo studies simulating several of the experiments. He showed that the presence of a distortion and the use of a polynomial correction function often caused the analysis to miss the presence

Table 2.1: 17 keV neutrino results as of December 1991.

Group	Method	Isotope	m_2(keV)[a]	$\sin^2\theta$(%)[a]	Ref.
Positive:					
Guelph	Int. Si(Li)	^{3}H	17.1 ± 0.2	0.5–1.6	[40, 54]
	Ext. Si(Li)	^{35}S	16.9 ± 0.4	0.73 ± 0.11	[53]
	Int. Ge	^{3}H	16.9 ± 0.1	0.6–1.6	[54]
LBL	Int. Ge	^{14}C	17 ± 2	1.4 ± 0.5	[55]
Oxford	Ext. Si(Li)	^{35}S	17.0 ± 0.4	0.8 ± 0.08	[56, 58]
	Ext. Si(Li)	^{63}Ni	16.8 ± 0.4	1.0 ± 0.2	[57, 58]
Zagreb	IBEC	^{71}Ge	17.2 ± 0.7	1.6 ± 0.5	[62, 66]
Negative:					
Princeton	Mag. Spec.	^{35}S	17	< 0.4 (99% CL)	[45]
ITEP	Mag. Spec.	^{35}S	17	< 0.17 (90% CL)	[46]
Bombay	Ext. Si(Li)	^{35}S	17	< 0.6 (90% CL)	[48]
Caltech	Mag. Spec.	^{35}S	17	< 0.3 (90% CL)	[47]
Tokyo	Ext. Si(Li)	^{35}S	17	< 0.15 (90% CL)	[50, 51]
ISOLDE	IBEC	^{125}I	17	< 2 (98% CL)	[60]
Chalk River	Mag. Spec.	^{63}Ni	17	< 0.3 (90% CL)	[52]
Zagreb	IBEC	^{55}Fe	17	< 0.74 (99.7% CL)	[61]
Munich	Mag. Spec.	^{177}Lu	17	< 0.4 (68% CL)	[67]
Other:					
LBL	IBEC	^{55}Fe	21 ± 2	0.85 ± 0.45	[63]
Buenos Aires	IBEC	^{71}Ge	13.8 ± 1.8	0.8 ± 0.3	[64]

[a]Separately quoted errors have been added in quadrature.

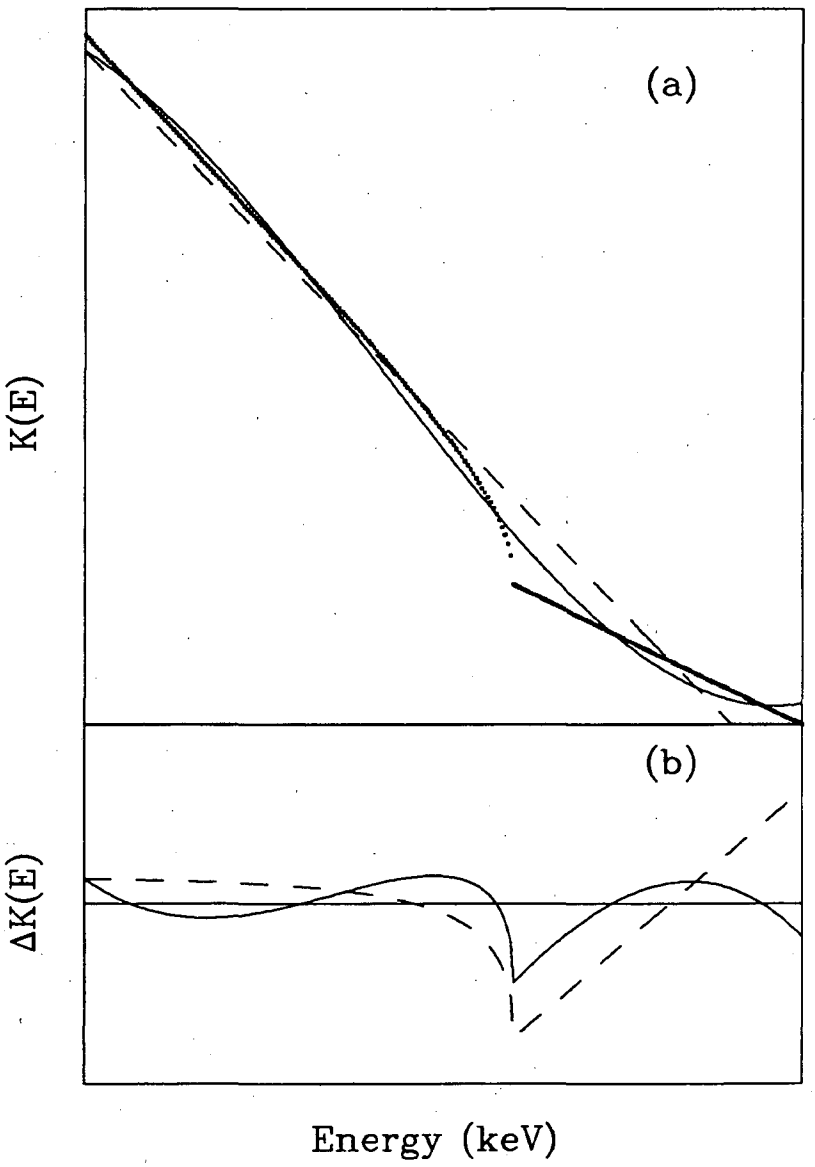

Figure 2.7: (a) The Kurie plot for a beta spectrum containing a massive neutrino admixture (exaggerated). Also shown are the best fit Kurie plots (no massive neutrino) with no shape correction (dashed), and a quadratic shape correction (solid). (b) The residual with no shape correction (dashed) and a quadratic shape correction (solid), revealing the loss in sensitivity.

of a neutrino kink.

A related and more important problem is that even if a shape correction is not needed to improve the fit, the presence of a smooth but unknown distortion in the data can correlate with the shape of S(E), and cause the massive neutrino signal to be either created or hidden. This can also be seen in Figure 2.7. Suppose the experimental spectrum contains a quadratic distortion to begin with, due to energy loss, scattering, efficiencies, or any systematic effect not properly accounted for. When a massive neutrino component is allowed in the fit, and the χ^2 is minimized, the fit values of m_2 and $\sin^2\theta$ will deviate from the true values to best accomodate the distortion. This concern puts all of the above experiments into question, since they all used a wide range fit but none had adequately demonstrated that system response and efficiencies were understood at the 1% level. This issue was clearly of paramount importance for second generation experiments.

Theoretically, a 17 keV mass neutrino was very difficult to reconcile with the electroweak standard model and other experimental results. Double-beta decay experiments excluded such a large majorana mass, so it would have to be a Dirac (or pseudodirac) particle. Yet supernova cooling rate observations seemed to suggest that it could not be an ordinary Dirac neutrino (although a 17 keV mass was not conclusively ruled out by this argument). Neutrino oscillation experiments ruled out its being dominantly muon-flavored, so it would have to be dominantly a tau neutrino. Measurement of the width of the Z resonance at LEP excluded a fourth light neutrino flavor (< 45 GeV). Big-bang neutrinos with a 17 keV mass would over-close the universe, so it would have to be unstable, with a lifetime much shorter than its standard model prediction, implying new physics. Attempts to simultaneously explain the solar neutrino problem and 17 keV neutrino experiments by neutrino mixing in three generations led to additional constraints. It is a tribute to theoretical ingenuity that in spite of all this a number of viable, if somewhat contrived, models for the 17 keV neutrino were developed. See [68–72] for

interesting discussions of some of these models. Although the theoretical debate over the 17 keV neutrino was fascinating, the question of its existence remained an experimental issue. In the summary talk at the Workshop on the 17 keV Neutrino Question convened in Berkeley in December 1991, Bernard Sadoulet stated, "The 17 keV neutrino may not exist, but it will not be because it cannot exist." The stage was set for a new generation of experiments to resolve the controversy.

2.6 Second Generation Experiments

In the summer of 1992 three new experiments were reported that each presented strong evidence against the 17 keV neutrino. The first was a study of the ^{63}Ni beta spectrum using the iron-free $\pi\sqrt{2}$ magnetic spectrometer at INS Tokyo [73]. This effort was similar to the Chalk River ^{63}Ni experiment [52], but it had some systematic difficulties. The detector consisted of an array of 30 single-cell proportional counters. The source (50 μg/cm^2 Ni), source backing (1300 μg/cm^2 Ni), and detector window (200 μg/cm^2 polyester) were quite thick, causing a large tail in the response function, which was determined using only a single calibration line (K-conversion line from ^{109}Cd) measured in the same geometry. Improper treatment of correlated errors in the analysis led to erroneous fits (best fit χ^2=1251.7 for 1738 d.o.f.), but this was corrected in a later publication [74]. The strength of this experiment came from its extremely high statistics: 1.1×10^8 counts/keV at the kink position (50 keV) were collected; about 50–100 times that of the first generation experiments. With this statistical sample they were able to fit a narrow energy region (40–60 keV) and obtain sensitivity to the detailed shape of the kink. A 1% 17 keV neutrino was clearly absent in the data, as seen in Figure 2.8. The group quoted an upper limit of $\sin^2\theta < 7.3 \times 10^{-4}$ (95% CL) for a 17 keV neutrino.

The next result came from an elegent experiment at Argonne National Laboratory. Mortara *et al.* studied the beta spectrum of ^{35}S using a Si(Li) detector

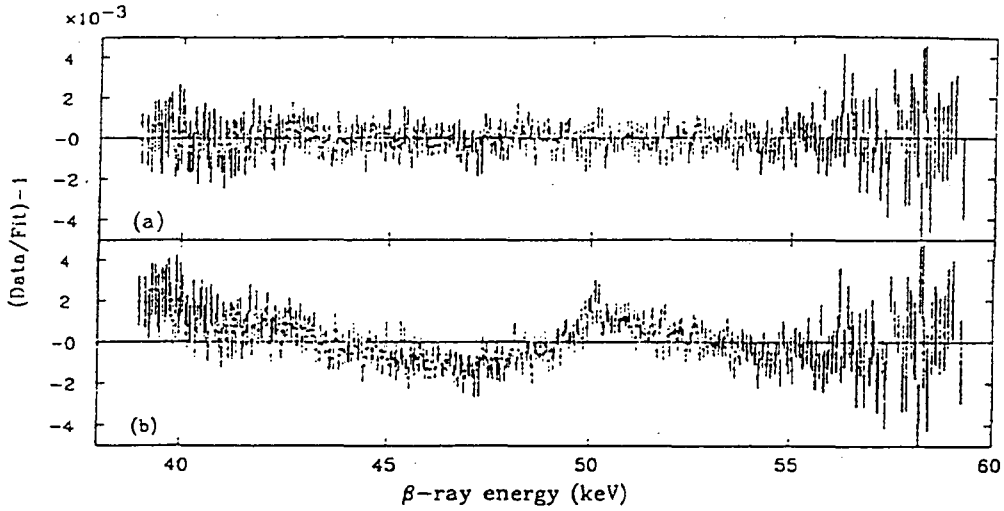

Figure 2.8: Data from [73] showing data/fit including a 17 keV neutrino with $\sin^2\theta$ equal to (a) 0.02% and (b) 1.0%, clearly ruling out the latter.

and an external source placed inside a superconducting solenoidal magnet [75]. This was similar to the Hime and Jelley experiment [56], however the magnetic field provided three significant improvements: the betas were focused onto the detector, increasing the acceptance; normal incidence was achieved without physical collimators, eliminating scattering problems; and betas backscattering out of the detector were reflected back in by the magnetic field, reducing the low energy tail in the response function. The last effect was achieved by shaping the axial field to form a magnetic mirror (see [76] for a discussion of this phenomenon). The apparatus is shown in Figure 2.9. The ^{35}S source ($10^{-4}\mu$g/cm^2), and source backing (20μg/cm^2) were very thin. Conversion lines from ^{139}Ce at 127, 160, and 165 keV and Monte Carlo simulations were used to evaluate the detector response function. These energies bracket the region of interest, unlike the ^{109}Cd and ^{57}Co lines used in [56]. Overall, the prevention and treatment of systematic effects in this experiment were very impressive; however a wide region of energy was fit (120–167 keV) and it remained to be proven that the massive neutrino was not obscured by

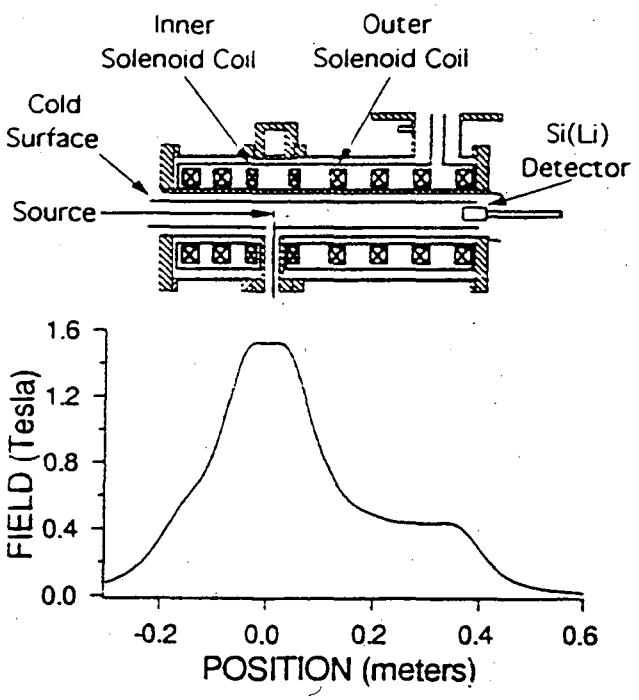

Figure 2.9: Schematic drawing of the apparatus used in [75]. The lower curve shows the axial magnetic field strength.

some small distortion. This was accomplished by counting a separate ^{35}S source that contained small admixture of ^{14}C, which has a beta endpoint of 156 keV. The result was a distortion in the data with a size and shape similar to that of the 17 keV neutrino. The ^{14}C contamination was seen in the data at the correct level (see Figure 2.10). An upper limit of $\sin^2\theta < 0.002$ (95% CL) was established for a 17 keV neutrino.

Finally, the Berkeley group that originally saw the positive result in ^{14}C reported a new result from a high statistics spectrum of ^{55}Fe IBEC [77]. A local kink search analysis, immune to global distortions in the spectrum, was used and a 0.8% 17 keV neutrino was excluded at the 7σ level. This experiment is described in detail in Chapter 4. Unlike all of the first generation efforts listed in Table 2.1, these three experiments were able to convincingly demonstrate sensitivity to the small distortion caused by a 1% 17 keV neutrino, and its final demise seemed certain. Most of the advocates of the heavy neutrino conceded at this point, and new efforts commenced to explain the positive results.

In 1992-94 a number of additional experimental results were reported, all finding no evidence for the 17 keV neutrino. Some of these were improvements on previous experiments. The Caltech group repeated their measurement of ^{35}S using a small (1 cm^2) silicon surface barrier detector with their magnetic spectrometer [78]. The measured backscatter fraction was now more reasonable (17%), and they attempted to demonstrate their sensitivity by generating a synthetic "kink" in the spectrum, masking part of the beam with an aluminum degrader. The Princeton group also repeated their ^{35}S magnetic spectrometer experiment using a small PIN diode detector (0.8 cm^2) and improved collimation to reduce scattering; and a detailed Monte Carlo simulation to determine the backscatter tail shape [79]. The group from Argentina reanalysed their ^{71}Ge IBEC data with improved treatment of the photon response function and pileup. In addition they allowed the absolute probabilities of IBEC from different shells to vary in the fits. They no longer saw

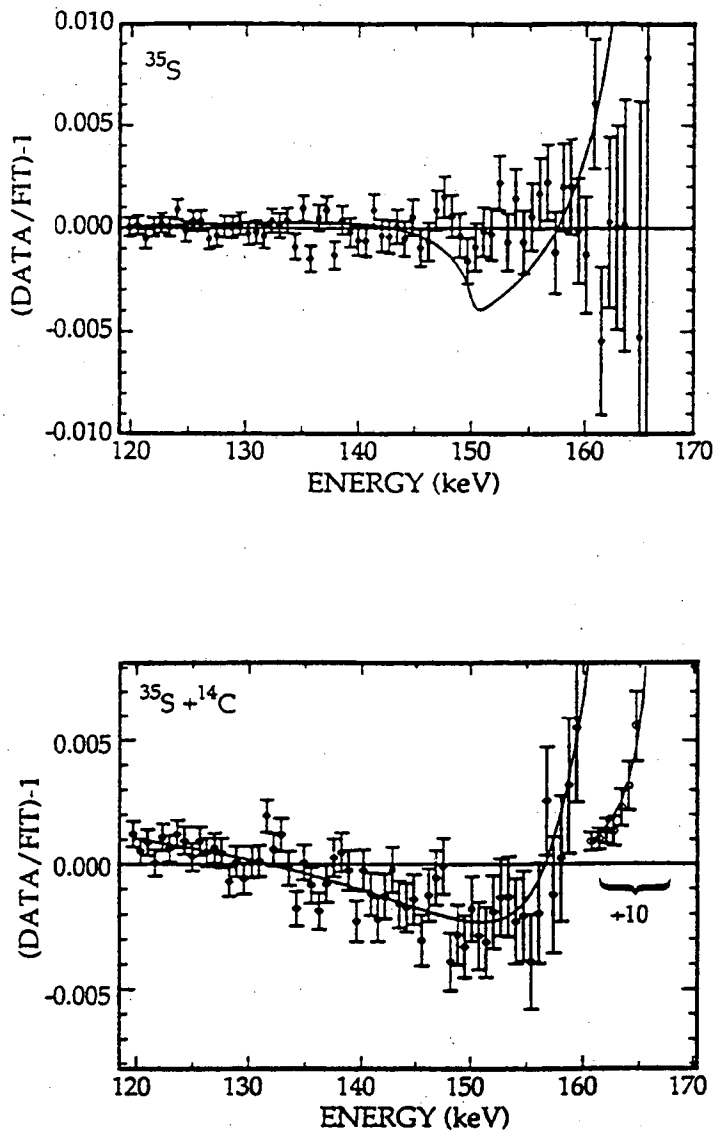

Figure 2.10: Data from [75]; (a) Data/fit for the ^{35}S data. The solid curve shows the expected result from a 17 keV neutrino with $\sin^2\theta$=0.85%. (b) Data/fit for the ^{35}S source containing 1.3% ^{14}C. The solid curve shows the expected result from this contamination.

Table 2.2: Second generation 17 keV neutrino experiments.

Group	Method	Isotope	m_2(keV)	$\sin^2\theta(\%)$	Ref.
INS Tokyo	Mag. Spec.	^{63}Ni	17	< 0.073 (95% CL)	[73, 74]
Argonne	Ext. Si(Li)	^{35}S	17	< 0.2 (95% CL)	[75]
Berkeley	IBEC	^{55}Fe	17	< 0.2 (95% CL)	[77]
U. Oklahoma	Int. gas	^{3}H	17	< 0.28 (99% CL)	[81]
Caltech	Mag. Spec.	^{35}S	17	< 0.2 (90% CL)	[78]
Princeton	Mag Spec.	^{35}S	17	< 0.3 (95% CL)[a]	[79]
Buenos Aires	IBEC	^{71}Ge	17	< 0.5 (95% CL)	[80]
ILL Grenoble	Ext. Si	^{35}S	17	< 0.18 (90% CL)	[82]
Tenn. Tech	IBEC	^{125}I	17	< 0.4 (90% CL)	[83]

[a] Estimated from the reference

a preference for a 13 keV neutrino; the best fit was now consistent with no massive neutrino [80].

Bahran and Kalbfleisch measured the tritium beta spectrum using a tritium-doped gas proportional chamber [81]. They did not observe the excess of counts below 1.5 keV reported by Simpson and Hime. New experimental results were also announced by groups at Grenoble and Tennessee Technological University. A summary of the second generation experiments (1992-1994) is given in Table 2.2. A world summary of the results and limits on the mixing of a 17 keV neutrino is shown in Figure 2.11.

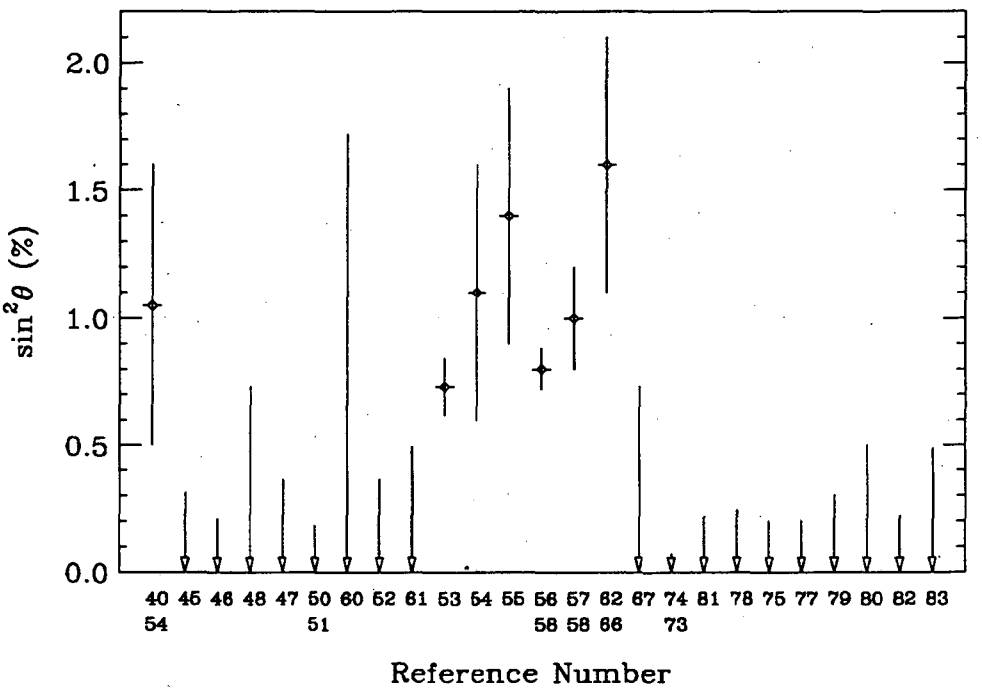

Figure 2.11: World summary of the results and limits on the mixing of a 17 keV neutrino. Error bars are 1σ and upper limits are 95% CL, estimated from the references as necessary assuming gaussian-distributed errors.

2.7 Epilogue

After a great deal of experimental effort, the 17 keV neutrino was finally shown to be nonexistent. The task of explaining the positive results remained. Initially there was hope that a common answer would be found, but eventually it became clear that each of the positive experiments would require a separate explanation.

Simpson has continued to examine the low energy spectral excess that he observed in the two implanted tritium experiments, but he has not found its cause. The first experiment [40] had problems with low-energy calibration and possible implantation defects and can perhaps be discounted. The germanium detector experiment [54] however overcame these problems and its result still stands. Unfortunately the detector has since sustained some damage which has hindered additional tests. It is interesting that Conway and Johnson in 1959 saw a similar spectral excess in tritium using a proportional chamber [84], though they did not consider a massive neutrino hypothesis. The possibility remains that the effect in tritium is real, but is not caused by a 17 keV neutrino. Alternatively, it may be due to some environmental effect in silicon and germanium. Koonin has suggested a model for such an effect [85], although this particular model is not supported by Simpson's tritium spectrum [86].

A lot of effort has been spent to explain the results of the Guelph and Oxford ^{35}S and ^{63}Ni experiments [53, 56, 57]. In 1992 Piilonen and Abashian presented a Monte Carlo simulation that indicated a similarity between the 17 keV neutrino effect and the effect of betas scattering from the Al anti-scatter baffles into the detector (see Figure 2.5) [87]. This had been neglected by Hime in the analysis. Hime later performed his own Monte Carlo study and reproduced their result, although he concedes that this may not explain the Guelph experiment [88]. Meanwhile, Bowler and Jelley have repeated the Oxford experiment using the same apparatus. They find that scattering from the Al baffle was at most a minor contribution. Instead they attribute the effect to energy losses in the chemically

adsorbed $BaSO_4$ source. This conclusion is supported by a proton microprobe study that showed the source to be anomalously thick. When the effective source thickness was allowed to vary in the fits the presence of a 17 keV neutrino was ruled out [89]. A fundamental problem in the ^{35}S experiments was a high sensitivity to the detailed shape of the beta response function of the apparatus, and the failure to measure this response function in the energy region fit. The response function was measured at low energies (63–129 keV) and extrapolated to the region of interest (120–170 keV). If higher energy electron lines had been used (e.g. ^{139}Ce, used by Mortara *et al.* [75]) then anomolies in the response might have been noticed early in the experiment. The same point can be made about the ^{63}Ni experiment, which used the single K-conversion line of ^{109}Cd at 61 keV to measure the response function for the energy region 30–62 keV.

The single positive IBEC experiment [62] and the experiments that saw 21 keV [63] and 14 keV [64] neutrinos can, I think, be discounted. They all had relatively low statistics, and uncertainties in the complicated detector response functions and the theoretical spectra could have easily produced distortions that caused the fits to prefer the massive neutrino signals.

Finally, the 17 keV neutrino signal in the LBL ^{14}C experiment has been linked to a subtle effect caused by the anode groove that separated the guard ring and center region of the detector. This is described in detail in Chapter 3.

Chapter 3

A ^{14}C-doped Germanium Detector

3.1 The Detector

High-precision beta spectroscopy is a difficult undertaking. Magnetic spectrometers have great resolution but seem to suffer from complicated systematic effects that tend to distort the spectra. Solid-state detectors have excellent efficiency and linearity, but getting the betas into the detector is a problem; scattering in the source, collimators, and other surrounding materials and back-diffusion from the detector complicate the overall response. Simpson's approach, implanting tritium inside a solid-state detector, overcame these problems but introduced another: crystal defects caused by the implantation could affect the detector's behavior. In addition, atomic and environmental effects that are negligible in higher energy decays may be significant in the low Q-value beta decay of tritium, and complicate the problem of searching for small features in the spectrum. Perhaps a better approach would be to introduce a radioactive sample into germanium prior to crystal growth. For example, the beta decay of ^{14}C to ^{14}N is an allowed ground-state to ground-state transition with $Q_\beta = 156.48$ keV [90]. A ^{14}C-doped germanium

detector could in principle be produced with no radiation damage. The maximum range of a 150 keV beta in germanium is 84 μm [91], so with a sufficiently large detector the efficiency would be nearly 100% and a fully calorimetric measurement of the ^{14}C beta spectrum could be made. This would be an excellent way to test Simpson's claim of a 17 keV neutrino; the kink would appear at 139 keV where the energy calibration is straightforward and atomic effects are negligible.

Fortuitously, a number of such ^{14}C-doped germanium detectors were already constructed by Haller, *et al.* in 1982 in order to study the solubility of carbon in germanium [92]. Although they are found in the same periodic group, carbon and germanium are metallurgically immiscible. To make these detectors, a mixture of ^{14}C-methane (10%) and ^{12}C-methane was introduced into a silica reaction chamber which contained a silica crucible held at 1050°C. This temperature was high enough to pyrolyze the methane and coat all surfaces inside the chamber with free carbon. Two crucibles were coated in this way, and several germanium crystals were then grown in these crucibles. Some of the crystals were made into radiation detectors, and by integrating the resulting beta spectra, the total carbon concentrations were obtained, ranging from 1.0×10^{14} to 4.5×10^{15} cm^{-3}. Autoradiographs were taken by sandwiching thin slices of the crystals between sheets of x-ray film and allowing the film to be exposed to the ^{14}C beta activity for a period of three months. This revealed that much of the carbon was concentrated into clusters of varying size, although the absolute sizes and numbers of clusters could not be quantitatively determined.

One of the crystals was melted and regrown in a bare crucible. An autoradiograph of this second-generation crystal showed no sign of clusters, and a radiation detector made from it measured a concentration of 6×10^{12} cm^{-3} total carbon. The physical dimensions of this detector are shown in Figure 3.1(top). It is a 12.8-mm-thick planar crystal with a Boron-implanted n^+ anode and a Lithium drifted p^+ cathode. The anode was segmented into a 30-mm-diameter central re-

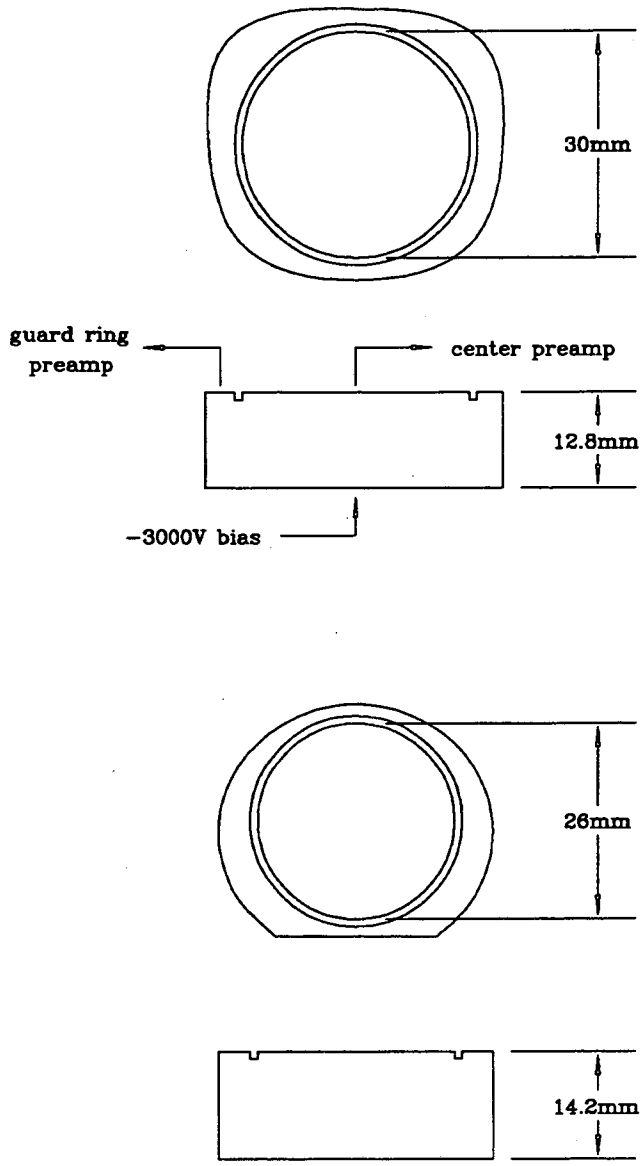

Figure 3.1: Actual size drawings of the ^{14}C-doped germanium detector (top) and the non-radioactive background detector (bottom).

gion and an outer guard ring, separated by a 1-mm-wide circular groove. The purpose of the guard ring was to veto events that occur near the edge of the detector. Surface effects on the edge can cause the electric field lines to fringe outward and trap ionization charge at the surface, resulting in incomplete charge collection. In addition, betas from the ^{14}C close to the edge may escape without depositing their full energy. A small number of betas can still escape near the anode and cathode without generating a veto, resulting in a small tail in the detector's energy response.

The ^{14}C detector's counting rate was quite low (about 20 sec^{-1}), so environmental background was significant and had to be subtracted. To measure the background a separate germanium crystal was grown using the above method but in a non-radioactive carbon-coated silica crucible. This crystal was then made into a planar detector with a size and configuration similar to the ^{14}C detector. It has a thickness of 14.2 mm and a central region of 26 mm diameter. The dimensions of the background detector are shown in Figure 3.1(bottom). Haller, *et al.* found that the shape of the obtained ^{14}C beta spectrum, after background subtraction, was in close agreement with the allowed beta spectrum theoretical shape [92]. The statistical sample for this measurement was relatively low (about 2×10^6 total counts).

3.2 The Experiment

In 1989 the second-generation ^{14}C-doped germanium detector and the non-radioactive background detector (Figure 3.1) were taken out of storage and refurbished at LBL's detector lab in order to begin an experiment to search for evidence of massive neutrino emission in the ^{14}C beta spectrum. Initial tests of the detector using calibration gamma sources in the energy range 60–400 keV showed excellent linearity and resolution (1–1.3 keV FWHM). The crystal was installed in a

standard gamma-detector cryostat and aluminum can with no window. Separate FET integrating preamps for the center region and guard ring were used. The high voltage circuit was configured with a pulser input so that a periodic pulse could be summed with the bias voltage to create a monoenergetic signal in the detector for monitoring gain stability.

The integrated ^{14}C counting rate in the detector was 20 sec^{-1}, so betas having energies within 17 keV of the endpoint were collected at a rate of only about 320 per hour. For this reason it was very important to minimize the environmental background counting rate. The experiment was conducted in the Low Background Counting Facility at LBL, which is shielded from the local accelerators by a hillside and covered with 4–5 ft. of concrete. The entire apparatus was surrounded by 10 cm of low-activity lead. The detector can was also enclosed by a graded shield consisting of several mm each of Al, Cu, Cd, and Sn, and a 13-mm-thick brass end-plate. In this arrangement the background counting rate was about 2 counts per hour per keV in the energy range 100–160 keV; attributable to natural radioactivity in the detector and shielding materials.

Figure 3.2 shows a schematic diagram of the experiment. Data was accumulated in 1–7 day intervals on a PC-based system using the Ortec MAESTRO data acquisition software. Three Ortec 916 ADC's collected simultaneous spectra: center region singles, guard ring singles, and center region vetoed by the guard ring. Each spectrum contained 4096 channels with 144 eV/channel. A bias of -3000 VDC was supplied to the detector, along with a dual pulser that generated alternating pulses at two energies (10 and 484 keV) with a total rate of 5 Hz. Energy signals were processed using Tennelec 243 amplifiers with 4 μs shaping times, and timing signals were generated using the slow unipolar outputs of Tennelec 248 amplifiers with 0.5 μs shaping times. The guard ring veto threshold was set using an Ortec 551 single channel analyzer (SCA), and the veto logic was made with LBL gate generators and an Ortec 418A coincidence amplifier.

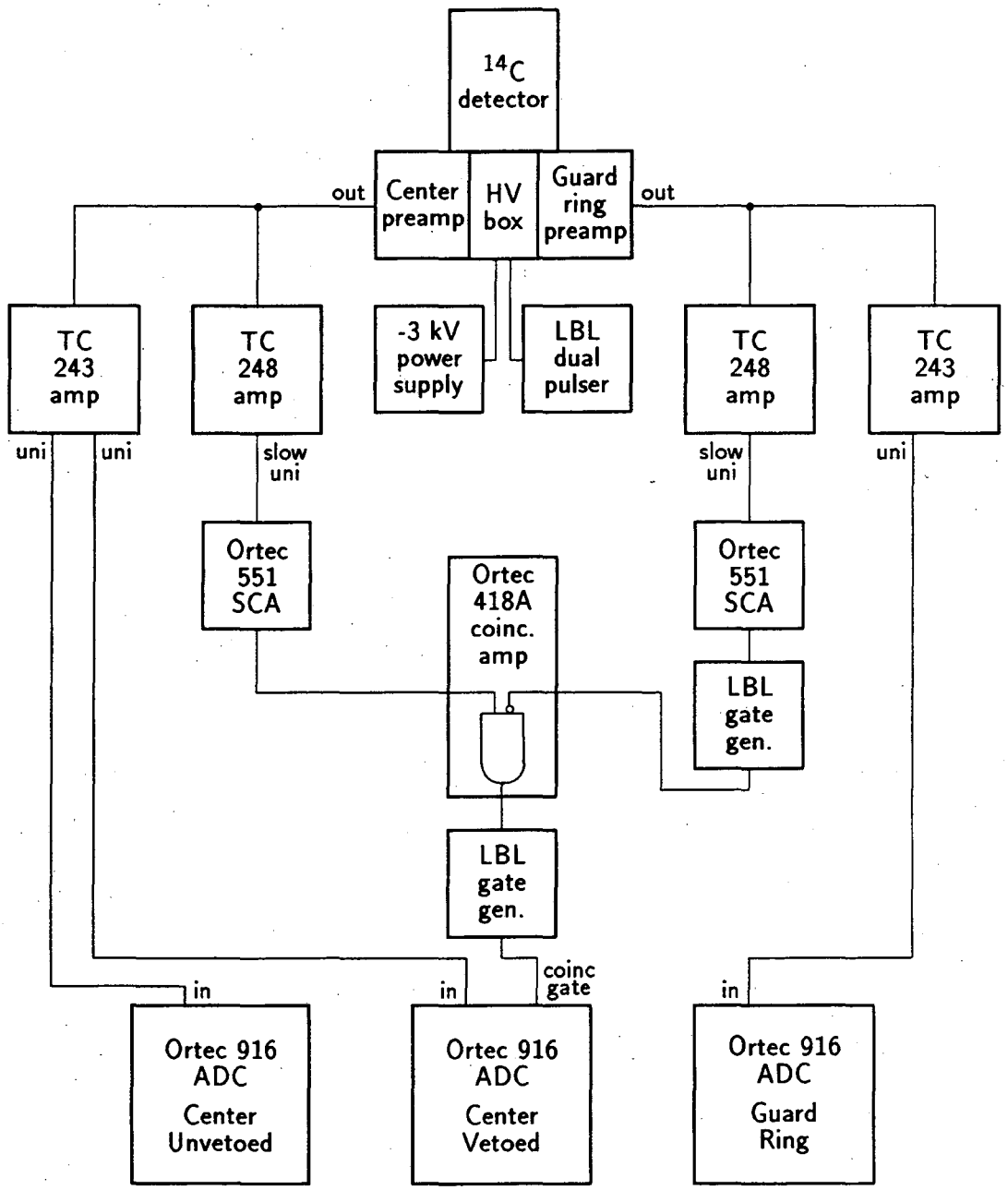

Figure 3.2: Schematic diagram of the ^{14}C experiment

Because the ^{14}C betas have such a short range in germanium, very few events were expected to produce a true coincidence signal in both the center region and the guard ring. However, capacitive coupling between the center and guard ring electrodes and the ionization region causes a small bipolar image pulse to be generated in one electrode whenever a true signal appears in the other. A detailed discussion of this phenomenon is given in Appendix A. In order to prevent vetoing a true center region event on the associated bipolar image signal in the guard ring, the guard ring veto lower threshold was set conservatively at 0.47 volts, which is equivalent to a 20 keV energy signal. The upper threshold was set at 4.50 volts, or 183 keV, well above the ^{14}C endpoint.

A grand total of 392 days of data were collected with the ^{14}C detector. The total vetoed spectrum is shown in Figure 3.3. It contains about 3×10^5 counts/keV at 139 keV (the expected kink position for a 17 keV neutrino). An additional 111 days were collected with the background detector installed in the same cryostat. This spectrum is shown in Figure 3.4. All lines in the ^{14}C and background spectra were identified and accounted for as naturally occuring thorium and uranium decay-chain activity. A list of these background lines and their intensities is given in Table 3.1.

There was no practical way to measure the beta response function of the detector using an electron source, so the response function was determined by making the following argument: a low energy gamma ray will interact inside the detector primarily by creating a single photoelectron (and a germanium x ray) which then ionizes the crystal to form an energy pulse. This photoelectron is indistinguishable from a beta of the same energy, so its response function should be the same. If the gamma ray interacts instead by Compton scattering and the scattered photon is completely absorbed, a full-energy signal will also be obtained. The measured gamma ray full-energy peak is observed to be very regular over a wide range of energy, so the Compton scattered and photoelectric full-energy peak

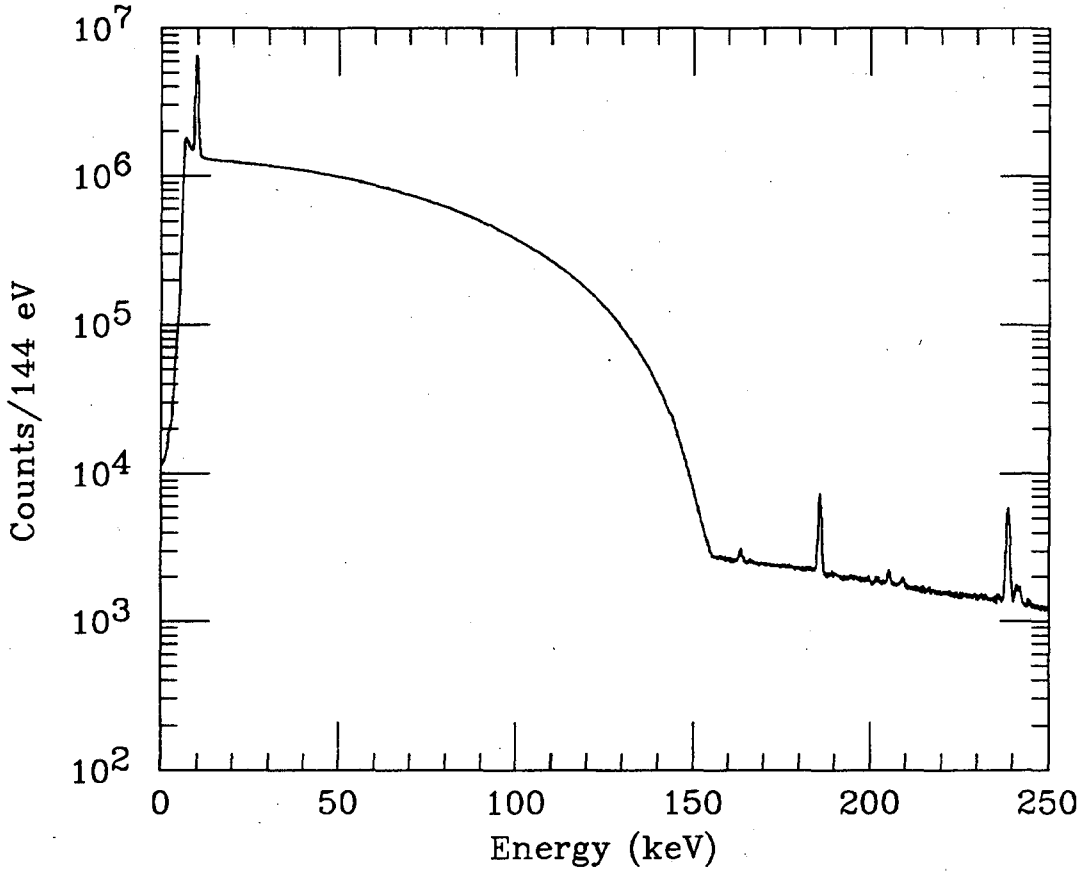

Figure 3.3: Total vetoed ^{14}C spectrum collected in 392 days.

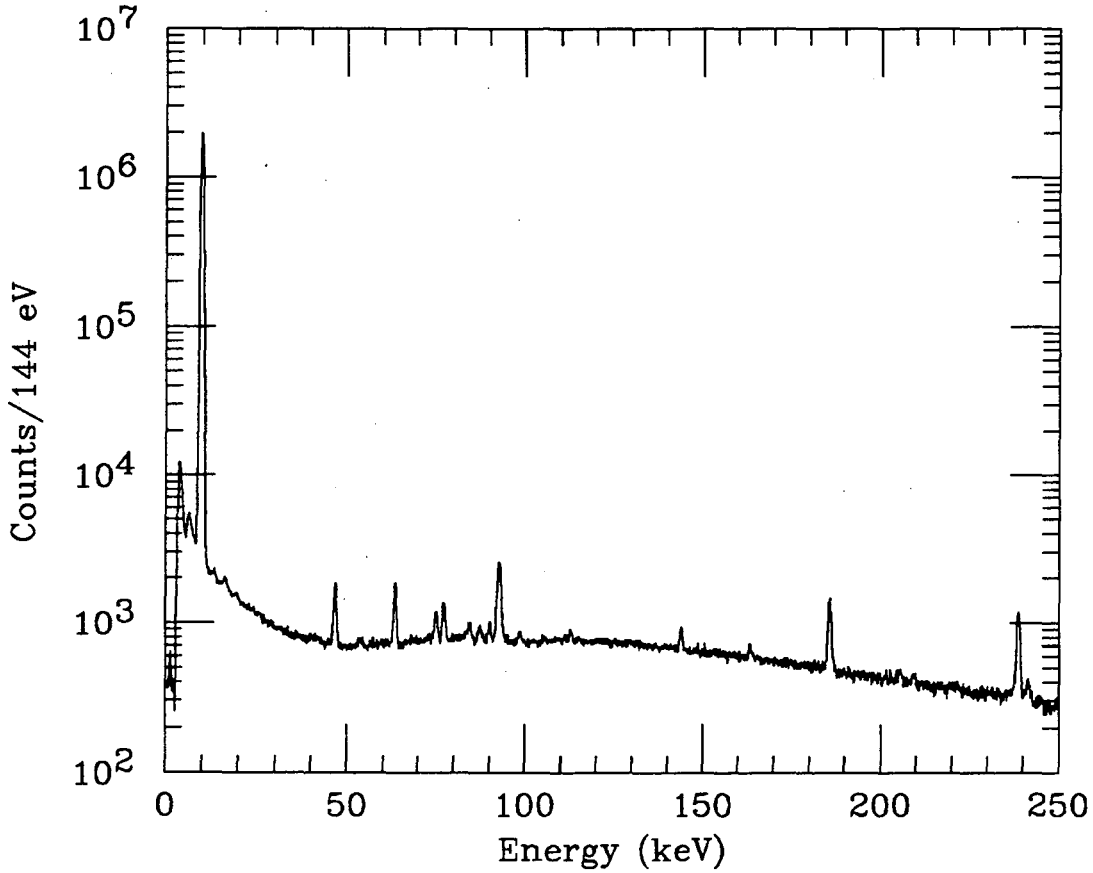

Figure 3.4: Total vetoed background spectrum collected in 111 days.

Table 3.1: ^{14}C background lines.

Energy (keV)	Origin	Intensity[a]	Energy (keV)	Origin	Intensity[a]
46.5	^{210}Pb	0.85	93.4	Th x ray	0.17
63.3	^{234}Th	0.91	98.4	U x ray	0.17
74.8	Bi x ray	0.24	105.6	Th x ray	0.05
75.0	Pb x ray	0.12	112.8	^{234}Th	0.08
77.1	Bi x ray	0.38	143.8	^{235}U	0.26
84.5	Pb x ray	0.09	163.4	^{235}U	0.13
84.9	Pb x ray	0.17	185.7	^{235}U	1.00
87.3	Bi x ray	0.12	205.3	^{235}U	0.10
89.8	Bi x ray	0.04	209.4	^{228}Ac	0.08
90.0	Th x ray	0.10	238.6	^{212}Pb	0.87
92.4	^{234}Th	0.86	241.9	^{214}Pb	0.11
92.8	^{234}Th	0.85			

[a]Intensity is the peak area in the vetoed background spectrum measured relative to the 185.7 keV ^{235}U line.

shapes must be essentially the same. Therefore the full-energy peak of the beta response function should be well represented by that of the same energy gamma ray. Measurements using calibration sources showed gamma-ray peaks to be highly gaussian with widths of 1.0 ± 0.1 keV FWHM in the region 100–160 keV. Figure 3.5 shows a combined spectrum of ^{241}Am, ^{57}Co, ^{133}Ba, ^{113}Sn, and ^{139}Ce collected with the ^{14}C detector.

The low energy part of the response will of course be much different for betas than for photons. Only two types of beta events were expected to contribute to the tail: those originating in decays very close (within ~ 100 μm) to the upper and lower surfaces of the crystal that escape without depositing their total energy; and those that cross from the center region to the guard ring (or vice versa) and deposit less than the threshold energy (20 keV) in the guard ring. The size of the tail caused by these events was estimated (assuming uniform distribution of ^{14}C) by Monte Carlo simulation using the GEANT code [101] and found to be about 0.2% for a 156 keV beta. The tail area should vary roughly in proportion to the beta's energy.

The energy scale of the system was calibrated using gamma ray sources, and the result is shown in Figure 3.6. The linearity exceeds that of most commercial planar germanium detectors. This calibration was monitored over time using the pulser peaks and background lines, and was found to be good to within $\pm 0.1\%$ over the course of the experiment.

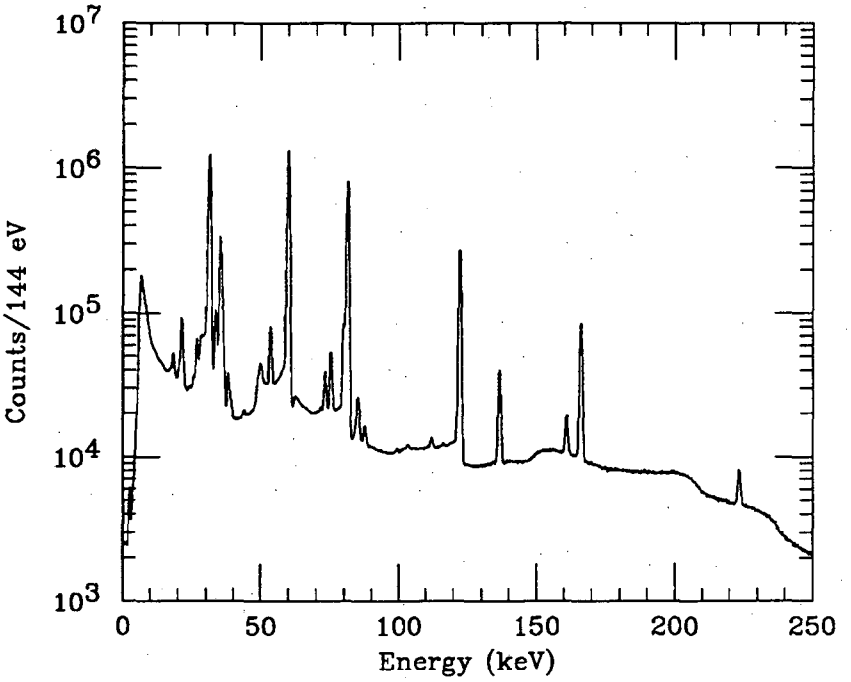

Figure 3.5: Combined gamma-ray spectrum of ^{241}Am, ^{57}Co, ^{133}Ba, ^{113}Sn, and ^{139}Ce collected with the ^{14}C detector.

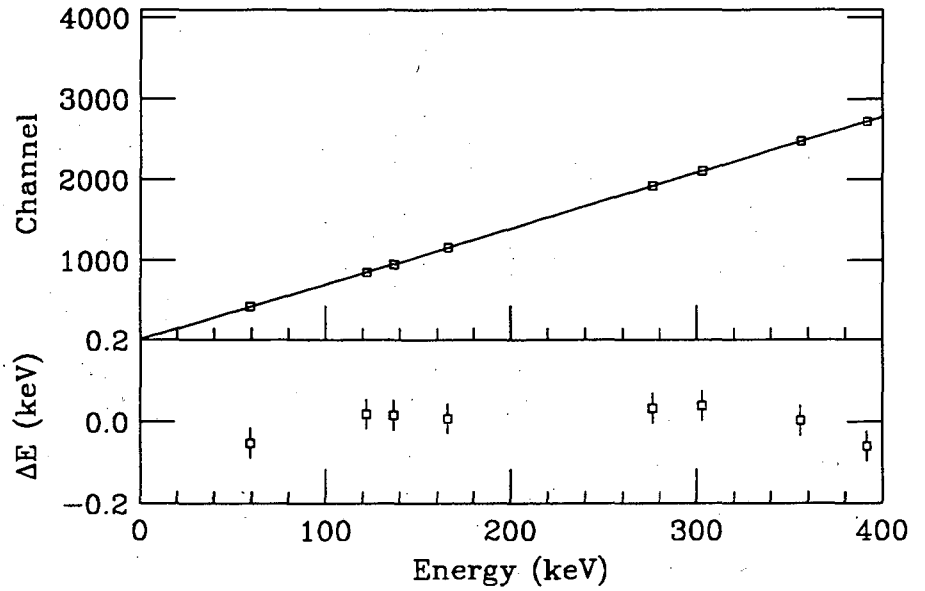

Figure 3.6: Gamma-ray calibration of the ^{14}C detector

3.3 The ^{14}C Beta Spectrum

Carbon-14 beta decay is an allowed $0^+ \rightarrow 1^+$ Gamow-Teller transition. The beta energy spectrum with a massless neutrino can be written [93]:

$$dN(E) = \frac{1}{2\pi^3}\xi C(E)R(E)F(Z,E)pE(Q-E)^2dE. \tag{3.1}$$

E and p are the beta energy and momentum. The Fermi function $F(Z,E)$ accounts for the final state interaction between the beta and daughter nucleus; ξ is the energy-independent allowed nuclear matrix element; the spectral shape factor $C(E)$ contains departures from the allowed shape; and $R(E)$ represents radiative corrections. By evaluating the Dirac wave function of the beta in the Coulomb field of a fixed point source, the Fermi function can be obtained [94]:

$$F(Z,E) = 2\,(\gamma+1)\,\Gamma(2\gamma+1)^{-2}\,(2pR)^{2(\gamma-1)}\exp\left(\frac{\pi\alpha ZW}{p}\right)|\Gamma(\gamma+i\alpha ZW/p)|^2 \tag{3.2}$$

with

$$W = E/m_e, \qquad p = \sqrt{W^2-1}, \qquad \gamma = \sqrt{1-(\alpha Z)^2}.$$

R is an arbitrary length parameter usually taken to be the nuclear radius. An expansion of $F(Z,E)$ in powers of (αZ), with corrections for nuclear recoil and the finite size of the nucleus, are given in [94]. Screening of the Coulomb field due to atomic electrons can be incorporated by shifting the origin of the Fermi function by V_0:

$$V_0 = N(Z)\alpha^2 Z^{4/3} m_e \tag{3.3}$$

where $N(Z)$ is a tabulated function [95]. For the case of ^{14}C, $V_0 = 495$ eV. The Fermi function for ^{14}C, calculated to order $(\alpha Z)^3$ and including nuclear recoil and size and atomic screening corrections, is shown in Figure 3.7.

The radiative correction for beta decay to first order in α has been calculated [96]:

$$R(E) = 1 + \frac{\alpha}{2\pi}g(W,Q) \tag{3.4}$$

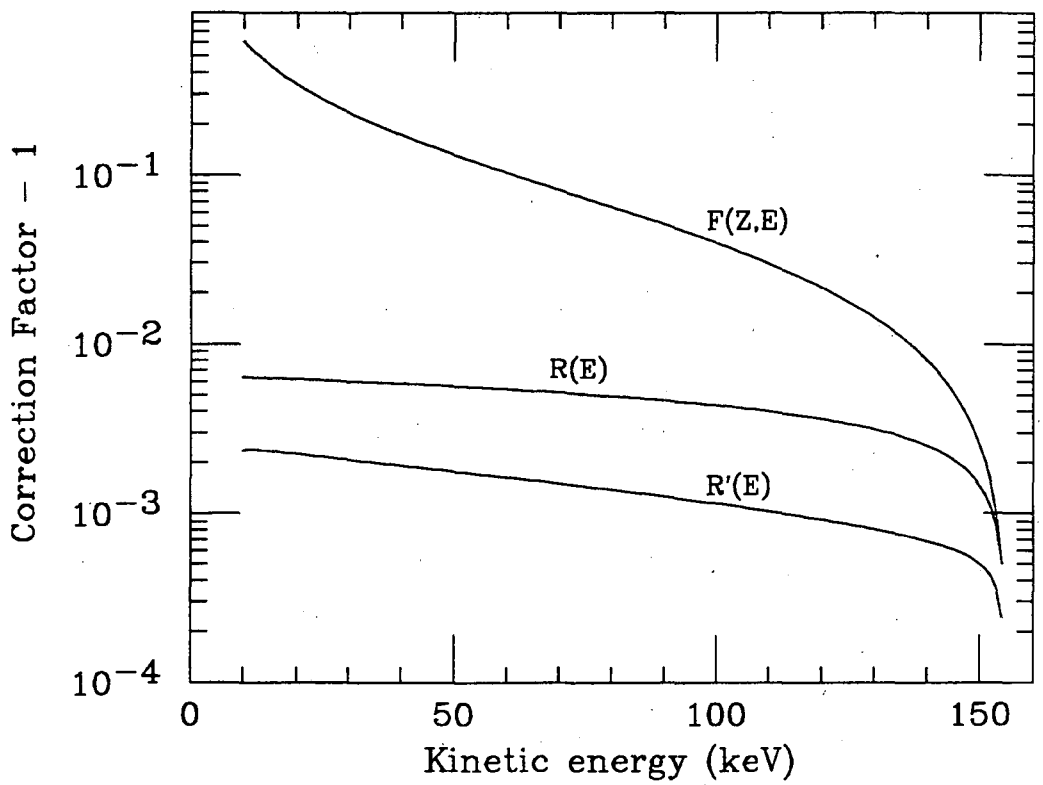

Figure 3.7: $F(Z,E)$: ^{14}C Fermi function (Z=7) with corrections for nuclear mass and size; $R(E)$: the first order radiative correction to ^{14}C beta decay assuming all IB photons escape; $R'(E)$: the radiative correction assuming all IB photons are collected.

with

$$g(W,W_0) = 3\ln M - \frac{3}{4} + 4\left(\frac{\tanh^{-1}\beta}{\beta} - 1\right) \cdot\left\{\frac{W_0 - W}{3W} - \frac{3}{2} + \ln\left[2\left(W_0 - W\right)\right]\right\} + \frac{4}{\beta}L\left(\frac{2\beta}{1+\beta}\right) + \frac{1}{\beta}\left(\tanh^{-1}\beta\right)\left[2\left(1+\beta^2\right) + \frac{(W_0 - W)^2}{6W^2} - 4\tanh^{-1}\beta\right]. \quad (3.5)$$

M is the nuclear mass in units of m_e, $W_0 = Q/m_e$ $\beta = p/W$, and $L(x)$ is the Spence function defined by:

$$L(x) = \int_0^x dt \frac{\ln(1-t)}{t}. \quad (3.6)$$

Figure 3.7 shows $R(E)$ calculated for ^{14}C. It includes the real inner-bremsstrahlung (IB) photons which are emitted in a small fraction of decays and assumes that these photons escape. In the ^{14}C-doped germanium detector most of these photons will be absorbed and their energies summed with the associated beta energies; so the observed radiative correction should be somewhat smaller than the theoretical correction. The probability that a beta created with energy W_i emits an IB photon of energy k is given by [97]:

$$d\Phi(W_i,k) = \frac{\alpha}{\pi k}\left(\frac{p_f}{p_i}\right)\left[\frac{W_i^2 + W_f^2}{W_i p_f}\ln\left(W_f + p_f\right) - 2\right]dk. \quad (3.7)$$

W_f and p_f are the energy and momentum of the beta after emitting the photon. The radiative correction due to IB only, when all the photons escape, will be:

$$R(E)_{IB} = 1 + \left(\frac{dP_F(W)}{dW}\right)^{-1} \cdot\left[\int_W^{W_0} dW'\, F(Z,W)\left(\frac{dP_F(W')}{dW'}\right)\left(\frac{d\Phi(W', k = W' - W)}{dk}\right) - \int_1^W dk\, F(Z, W-k)\left(\frac{dP_F(W)}{dW}\right)\left(\frac{d\Phi(W,k)}{dk}\right)\right] \quad (3.8)$$

where $dP_F(W) = pW(W_0 - W)^2 dW$ is the uncorrected Fermi beta function. The first integral expresses the relative probability that a beta is left with energy W

after emitting an IB photon. The second expresses the probability that a beta created with energy W ends up with lower energy due to IB emission. Note that the Fermi function $F(Z,W)$ is applied to the final beta state (after IB emission). If we assume that all IB photons are collected by the ^{14}C detector then the actual radiative correction is:

$$R'(E) = 1 + R(E) - R(E)_{IB} \tag{3.9}$$

Of course some of the IB photons will escape the detector, so $R'(E)$ and $R(E)$ should be considered lower and upper limits on the true radiative correction. $R'(E)$ is also shown in Figure 3.7.

The spectral shape factor can be parameterized by [98]

$$C(E) = 1 + aE + \frac{b}{E} + cE^2 + \cdots \tag{3.10}$$

and usually a, b, c are negligible in allowed transitions. However ^{14}C has an anomlously long half-life, implying a suppression of the allowed Gamow-Teller matrix element, so the relative size of the shape factor is expected to be large. The dominant contribution comes from weak magnetism, a consequence of the Conservation of Vector Current (CVC) theory of Feynman and Gell-Mann [99]. CVC supposes that the isovector part of the electromagnetic current and the weak currents corresponding to β^+ and β^- decay together form a conserved isovector triplet current. This was a precurser to the $SU(2) \times U(1)$ model that unified the weak and electromagnetic interactions. With this assertion the weak-magnetic form factor for β^- decay can be related to the transition magnetic moment of the analogous $M1$ γ transition in the daughter nucleus, which in turn can be obtained from the observed γ-ray energy and width. A recent calculation of the CVC-predicted shape factor for ^{14}C has $C(E) = 1+aE$ with $a = -0.41$ or $+0.76$ MeV^{-1} [100], depending on the sign of the transition magnetic moment, which cannot be obtained from the $M1$ transition ($\Gamma_\gamma \propto \mu^2$).

A massive neutrino is incorporated into (3.1) by making the substitution:

$$(Q-E)^2 \rightarrow (Q-E)\sqrt{(Q-E)^2 - m_\nu^2} \tag{3.11}$$

3.4 Data Analysis

The total ^{14}C data (392 days) were fit to the theoretical spectrum (Equations (1.15) and (3.1)) using a non-linear least-squares fitting routine [102]. The overall amplitude, endpoint kinetic energy ($E_0 = Q - m_e$), and neutrino mass parameters (m_2 and $\sin^2\theta$) were allowed to vary freely in the fits. The background data (111 days) were subtracted with the normalization varied as a free parameter, most of the sensitivity coming from the region between the endpoint and 160 keV (the highest energy fit). The background detector and ^{14}C detector have different volumes so a live-time background normalization was not appropriate. The following spectral shape factor was used:

$$C(E) = 1 + aE \tag{3.12}$$

with a also varied freely in the fit.

During the fitting process the theoretical spectrum was convoluted with the detector response function, which consisted of a gaussian full-energy peak and a flat tail with area 0.2%/156 keV (from the GEANT calculation). The presence or absence of this tail had a negligible effect on the outcomes of the fits. Use of a larger tail (up to 4%/156 keV) in the 100–160 keV fits resulted in a smaller value for the shape factor a and no significant change in the goodness-of-fit or the other parameters. The width of the gaussian peak was fixed at 1 keV FWHM based on the observed gamma-ray widths. Varying this width by up to ±20%, or including a small energy dependence in the width, did not significantly affect the results.

Table 3.2 gives a summary of the fits. Good fits were obtained in the kinetic energy interval 100–160 keV. The best fit is shown in the first column. It calls for

Table 3.2: Results of fitting ^{14}C data (uncertainies are 1σ).

	Vetoed				Unvetoed
Kinetic energy region fit (keV)	100–160	100–160	100–160	50–160	100–160
Data points	60	60	60	110	60
χ^2	65.0	91.0	65.8	1090.7	60.2
E_0 (keV)	155.78 ± 0.04	155.68	155.78	155.87	155.75
m_2 (keV)	16.6 ± 0.6	0[a]	16.6	16.9	16.3
$\sin^2\theta$ (%)	1.25 ± 0.25	0[a]	1.20	2.5	0.77
a (MeV^{-1})	-0.68 ± 0.02	-0.67	-0.67	b	-0.71
Background norm. factor	4.46 ± 0.03	4.50	4.46	4.42	4.58
Rad. correction (Figure 3.7)	$R'(E)$	$R'(E)$	$R(E)$	$R'(E)$	$R'(E)$

[a]Held fixed during fit

[b]Not meaningful

a neutrino admixture with mass 16.6 ± 0.6 keV and $\sin^2\theta = 1.25 \pm 0.25\%$, in excellent agreement with the results of Simpson and Hime [40, 53, 54, 56]. The second column shows a similar fit where the neutrino mass and mixing were fixed at zero. The chi-squared increases by 26 units, a difference of 5σ. The data/fit for this case is shown in Figure 3.8, normalized both above the kink position and uniformly over the region fit.

The fits in the first and second columns of Table 3.2 both used the radiative correction $R'(E)$ (Figure 3.7), which assumes that all IB photons are collected in the detector. The fit shown in the third column used the correction $R(E)$,

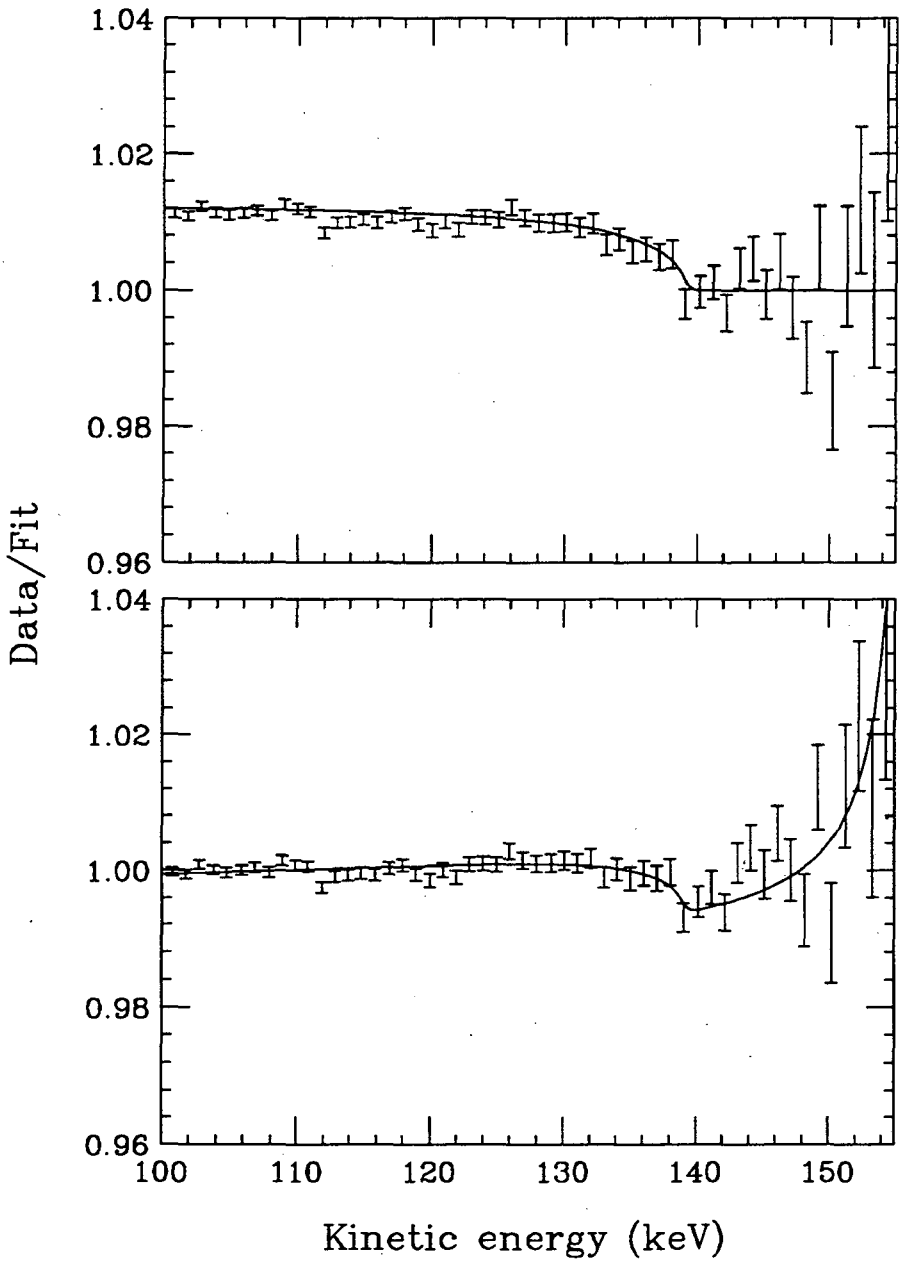

Figure 3.8: Data/fit of total vetoed ^{14}C spectrum from 100–160 keV fit to the theoretical spectrum (3.1) with no massive neutrino. The normalization is taken from 140–155 keV (top) and over the entire interval (bottom). The solid curves show the expected result for $m_2 = 16.6$ keV, $\sin^2\theta = 1.25\%$.

which assumes that all IB photons escape. This fit was slightly worse, but not by a significant amount. The goodness-of-fit worsened considerably when energies below 100 keV were included in the fits, indicating significant distortion of the spectrum at these energies. For example, the fourth column shows a fit to the energy interval 50–160 keV. The fit was very poor, although the fit values of E_0 and m_2 were consistent with those of the smaller interval. The last column gives the results from a fit to the unvetoed center region data from 100–160 keV. The best-fit value of $\sin^2\theta$ was significantly lower but the results of other parameters were consistent.

The endpoint energy E_0 was determined very precisely in the fits, and the result was about 700 eV lower than the accepted value [90] of 156.473 keV. The endpoint problem is discussed further in Section 3.7. The spectral shape factor a was considerable larger than the CVC prediction.

3.5 Systematic Problems and Additional Tests

The evidence for emission of a 17 keV neutrino in the fits to the ^{14}C data, apparently confirming Simpson's and Hime's results, was very exciting. It helped fuel the debate over its existence. However there were some serious anomalies in the data that needed to be understood before a definite conclusion about the neutrino could be made. First of all, the fits were good only for the last 60 keV of the spectrum and a systematic distortion was increasingly evident as lower energies were included. A good fit should have been obtained over a much larger energy range if the detector was functioning as expected. Another concern was the observed coincidence rate; approximately 9% of the center region signals were vetoed by signals in the guard ring. The guard ring veto threshold at 0.47 V was much higher than the level of the coincident bipolar pulses; and the expected rate of true concidences, where the beta deposits energy in both the center and guard ring, was

less than 1%. Both of these problems suggested that the detector's beta response function, determined indirectly from the gamma-ray data and Monte Carlo, was really not well understood.

In order to help understand the coincidence signals, six days of ^{14}C data were collected with a CAMAC-based multi-parameter data acquisition system. This allowed the center and guard ring energies to be recorded separately for each event. Figure 3.9 shows a 2-D plot of center vs. guard ring energy for coincident events. This picture was quite surprising and difficult to understand. Not only was the coincidence rate very high, a large fraction of the events fell into radial bands, where the guard ring energy was proportional to the center energy. An early hypothesis was that these coincidences were caused by electronic cross-talk between the center and guard ring preamp inputs, but this was ultimately ruled out; it would have required unreasonably large capacitances in the system.

A breakthrough in solving the coincidence problem came from scanning the detector with a highly collimated gamma-ray source. A 500 μCi point source of ^{141}Ce was prepared and placed behind a 500-μm-diameter hole in a 1/4-inch-thick lead plate. Starting at the center of the detector face on the side opposite the groove, the source was moved radially outward in 0.5–1.0-mm increments to the outer edge of the guard ring and a spectrum was collected at each increment (see Figure 3.10). ^{141}Ce has a gamma ray at 145 keV, which is inside the energy range of interest (100–160 keV). The mean range of this gamma ray in germanium is 1.1 cm, so the entire thickness of the crystal was illuminated in these measurements. A gamma ray at this energy has about an equal probability of interacting by Compton scattering and photoelectric effect in germanium [103]. Figure 3.11 shows a 2-D spectrum of center vs. guard ring energy at a position of 15.5 mm from the center, directly underneath the groove. The coincidences that sum to 145 keV form a double line. The fainter, straight line contains events where the gamma ray Compton scattered in the guard ring and the scattered photon was subsequently

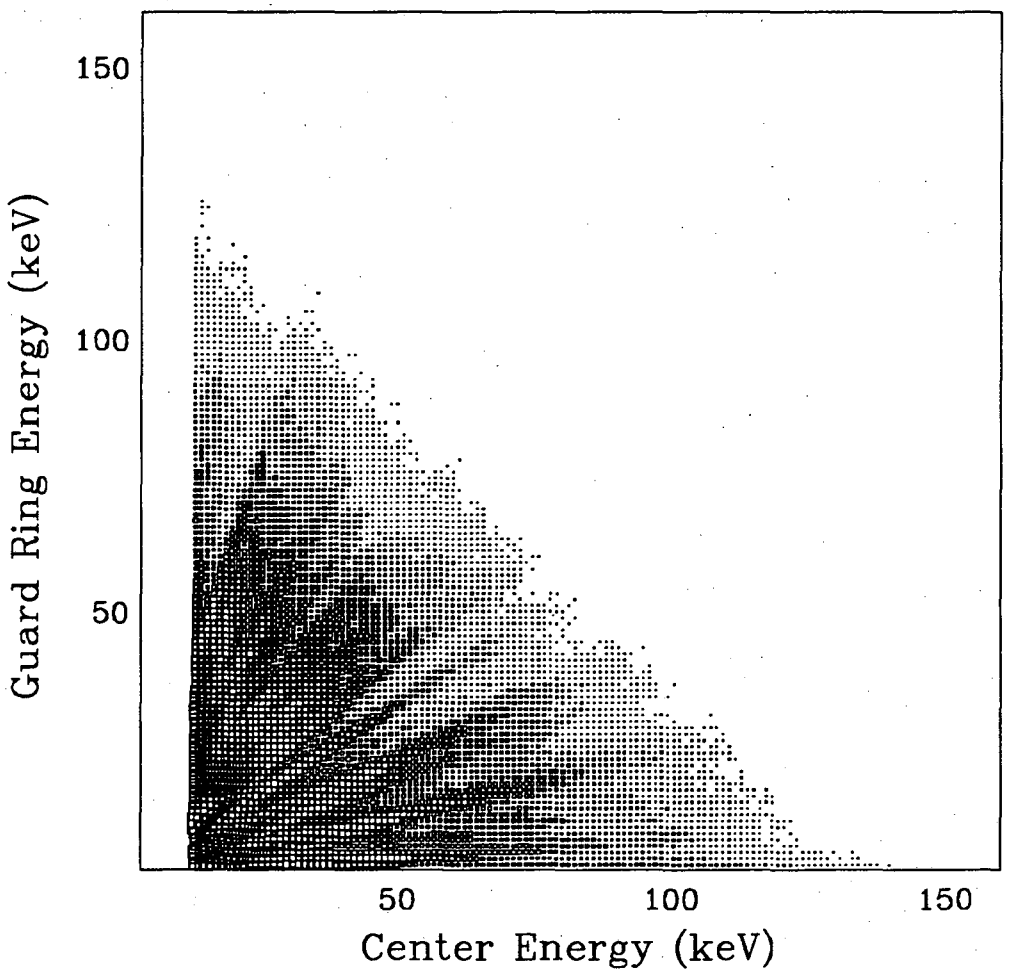

Figure 3.9: Center vs. guard ring energy for coincident ^{14}C events.

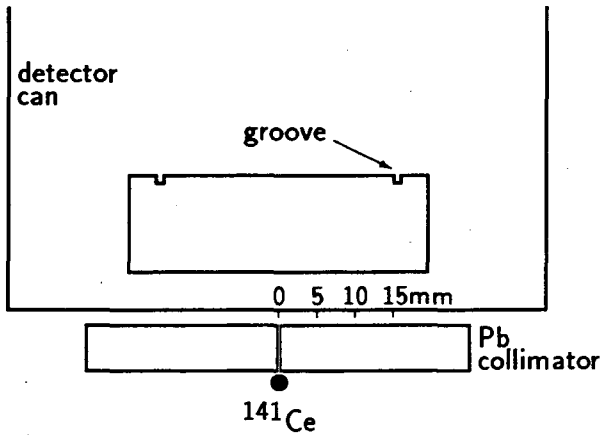

Figure 3.10: Collimated gamma-ray scan of the ^{14}C detector.

absorbed in the center, or vice versa. It exhibits the characteristic gap between the Compton photon and electron backscatter edges. This line faded gradually as the source was moved away from the groove. The stronger, slightly curved line was unexpected. It is peaked at one-half of the full energy and it disappeared entirely when the source was moved away from the groove. Its presence indicates that ionization charge was divided between the center and the guard ring when a gamma-ray interacted under the groove. The curvature in the coincidence line is most likely due to a small amount of charge being trapped at the surface of the groove. Charge division under the groove is also seen in the lower energy Pb and Pm x-rays. The "banana"-shaped curves at the left side of the spectrum are due to trapping of charge by a surface channel in the guard ring (see Appendix A for an explanation) and are not related to the charge division. They indicate chemical contamination or surface reconstruction on the edge of the crystal which was not present during the original experiment. This problem was later corrected by chemical treatment of the crystal.

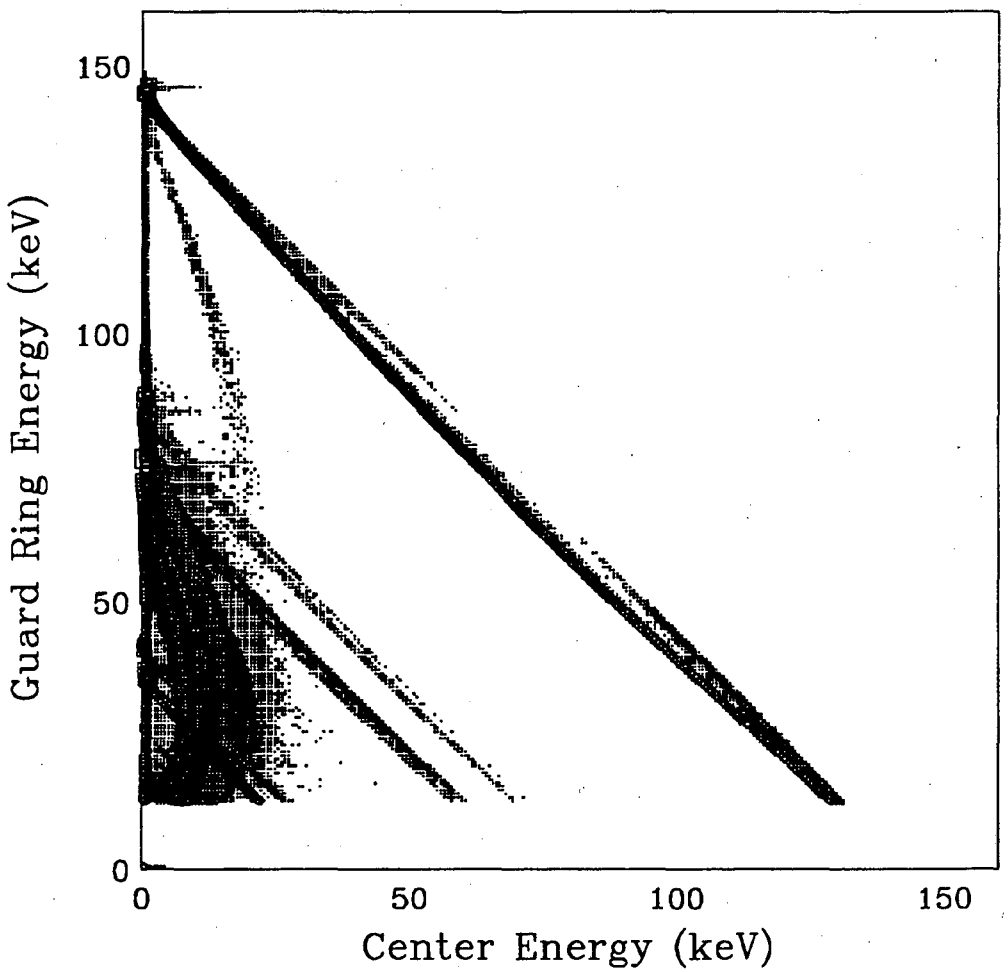

Figure 3.11: 2-D plot of center vs. guard ring energy for coincident ^{141}Ce events. The collimated source was 15.5 mm from the center of the ^{14}C detector (underneath the groove). The effects of charge division under the groove and surface channel trapping of charge are evident (see text).

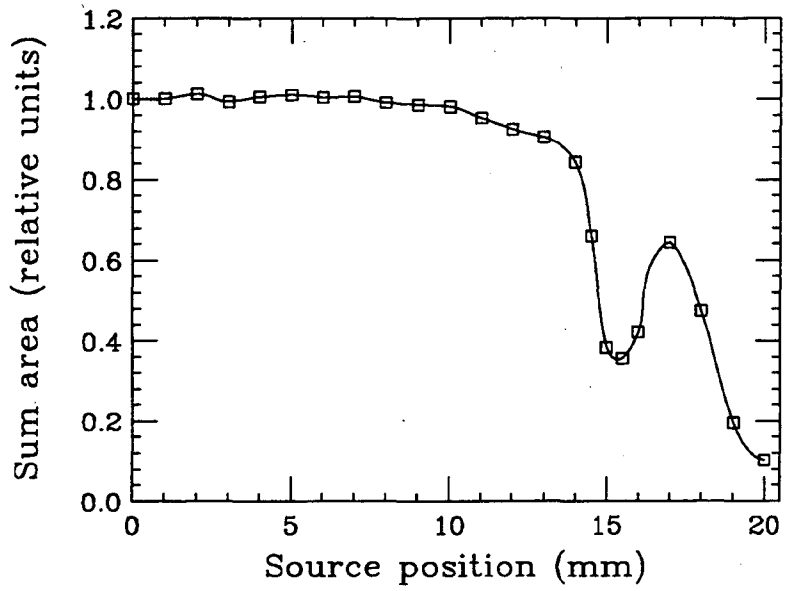

Figure 3.12: Plot of the sum of center and guard ring 145 keV photopeak areas as the collimated ^{141}Ce source was scanned across the detector. The groove is located at 15–16 mm.

Figure 3.12 shows a plot of the sum of the photopeak area in the center region and the photopeak area in the guard ring for the 145 keV line (note that the peak areas were summed, not the energies), as the source was scanned across the detector. The relative peak-area-sum dropped by a factor of two when the gamma-ray beam was underneath the groove (15–16 mm), and it rose again under the guard ring. This confirmed the hypothesis that charge is usually divided between the two regions if an interaction happens under the groove; the event ends up in neither peak. After correcting for beam divergence, attenuation, and Compton scattering, charge division occurred for about 70% of all interactions under the groove. This explains the high coincidence rate observed in the ^{14}C experiment. The volume under the groove is 13.8% of the volume in the center region. If the ^{14}C is distributed uniformly throughout the crystal, the coincidence rate should be about (0.7)(.138)=9.7% due to charge division.

Shortly after completing these tests we became aware of a very interesting

experiment performed by Luke and Haller [104]. Using a ^{14}C-doped germanium crystal from the same second-generation crystal as our detector, they fashioned a position sensitive detector (see Figure 3.13a). It operates as follows. When an ionization event occurs inside the detector, the ionization electrons drift rapidly to the n^+ contact and create a prompt signal. The positively charged holes drift slowly in the weak transverse field to the p^+ contact, giving a delayed signal. The time between these two signals is a measure of the transverse position of the event. Figure 3.13b shows the collected time spectrum when a collimated ^{241}Am source was moved along the length of the detector in 2-mm intervals. The individual positions are nicely resolved. Figure 3.13c shows the time spectrum collected from the internal ^{14}C decays. Each peak in this spectrum indicates the presence of a carbon cluster, i.e. a large concentration of decays originating from one position. By integrating the peaks, Luke and Haller were able to characterize the size of these clusters. A histogram is shown in Figure 3.13d. This result contradicts the earlier autoradiograph that showed no sign of carbon clusters in the ^{14}C-doped crystals of this generation. The autoradiograph technique was not sensitive to clusters of such small size.

The combination of carbon clusters and charge division under the groove can explain the radial bands observed in the ^{14}C coincidences (Figure 3.9). The ionization charge produced by a beta decay from a cluster located under the groove is split between the center and guard ring. The fraction that goes to each region depends on the exact shape of the electric field lines at that position. The clusters are tiny, so this fraction is constant for all decays originating from the same cluster, and they form a proportional band in the coincidence plot. Each salient band in Figure 3.9 is most likely a single cluster under the groove in the ^{14}C detector. The continuum beneath the bands is due to clusters too small to be resolved and/or fully dissolved carbon. Integrating the bands revealed that at least 50% of the total carbon is concentrated into clusters of various size. The most prominant bands are

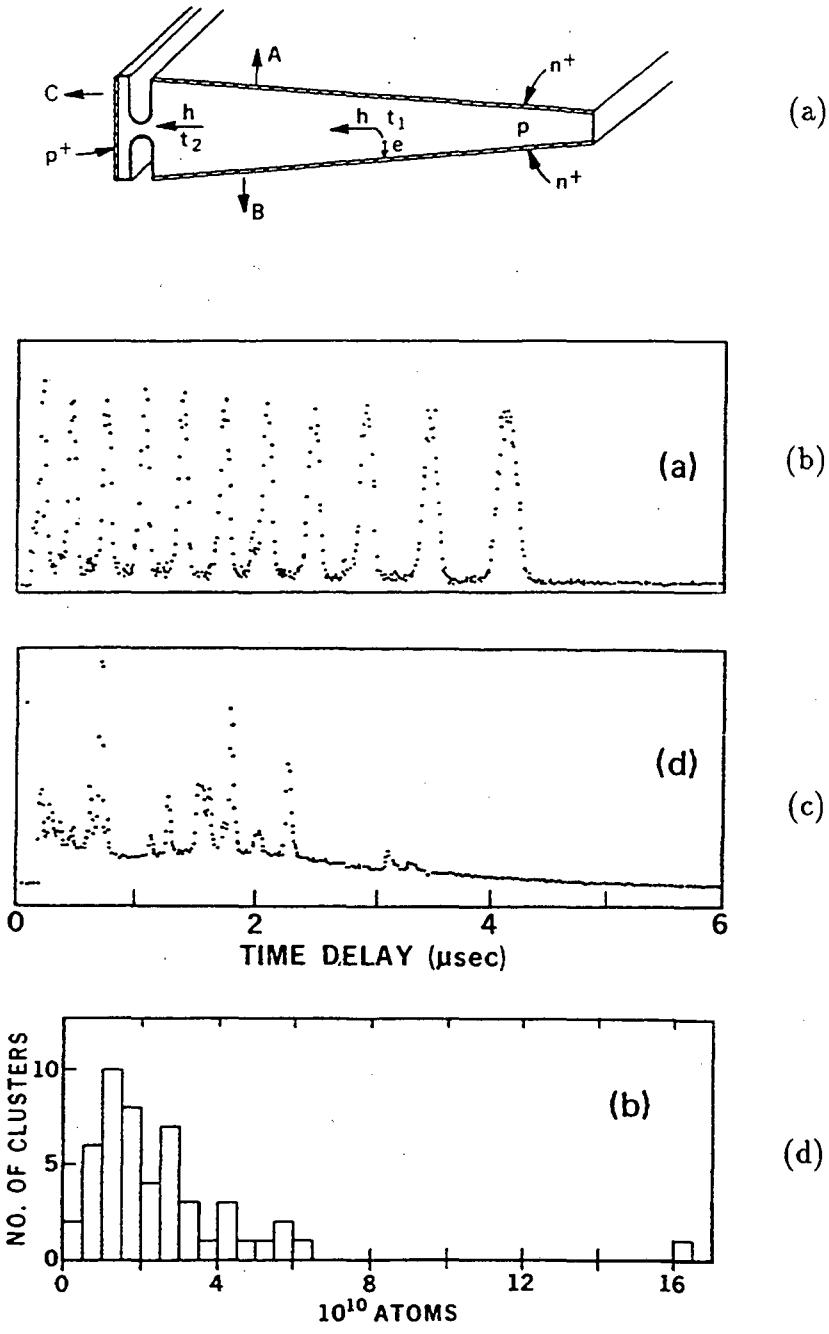

Figure 3.13: From [104]: (a) schematic diagram of the position sensitive ^{14}C-doped Ge detector; (b) time spectrum of collimated ^{241}Am source; (c) time spectrum of internal ^{14}C showing the presence of carbon clusters; (d) histogram of carbon cluster size in the Ge crystal.

each about 1–2% of the total coincidences. Based on the total counting rate of the crystal these clusters contain about $0.5–1 \times 10^{11}$ carbon atoms each (including ^{12}C). This is in excellent agreement with the position sensitive detector result (Figure 3.13d).

So what does this mean for the 17 keV neutrino experiment? In the original measurement, guard ring veto lower threshold was set at 0.47 V (equivalent to 20 keV energy) in order to prevent vetos from the bipolar signals. Therefore all charge-divided events under the groove where the guard ring collected less than 20 keV of equivalent charge were not vetoed. They were included along with the "good" ^{14}C events in the center region. The presence of this charge division contamination may explain the distortion in the wide-range fits and perhaps even the 17 keV neutrino signal.

3.6 A Second Measurement

A second ^{14}C measurement, using the multi-parameter data acquisition system, was conducted in 1993-94 to explore the effect of charge division under the groove on the beta spectral shape. Figure 3.14 shows a schematic diagram of the electronics. The acquisition system was triggered on center region events with an 8.5 keV threshold. This signal was also used to start an Ortec 457 time-to-amplitude converter (TAC). The TAC was stopped by a guard ring signal with the threshold set as low as possible (< 0.5 keV). Ortec 572 amplifiers were used to produce the center and guard ring energy signals, and the center energy, guard ring energy, and TAC output were recorded for each event. The dual pulser was used to monitor gain stability, generating simultaneous pulses in the center and guard ring at a total rate of 0.5 Hz. A total of 74 days of ^{14}C data were collected. The total center region spectrum is shown in Figure 3.15 and the total guard ring spectrum (triggered on center events) is shown in Figure 3.16. An additional 15 days data

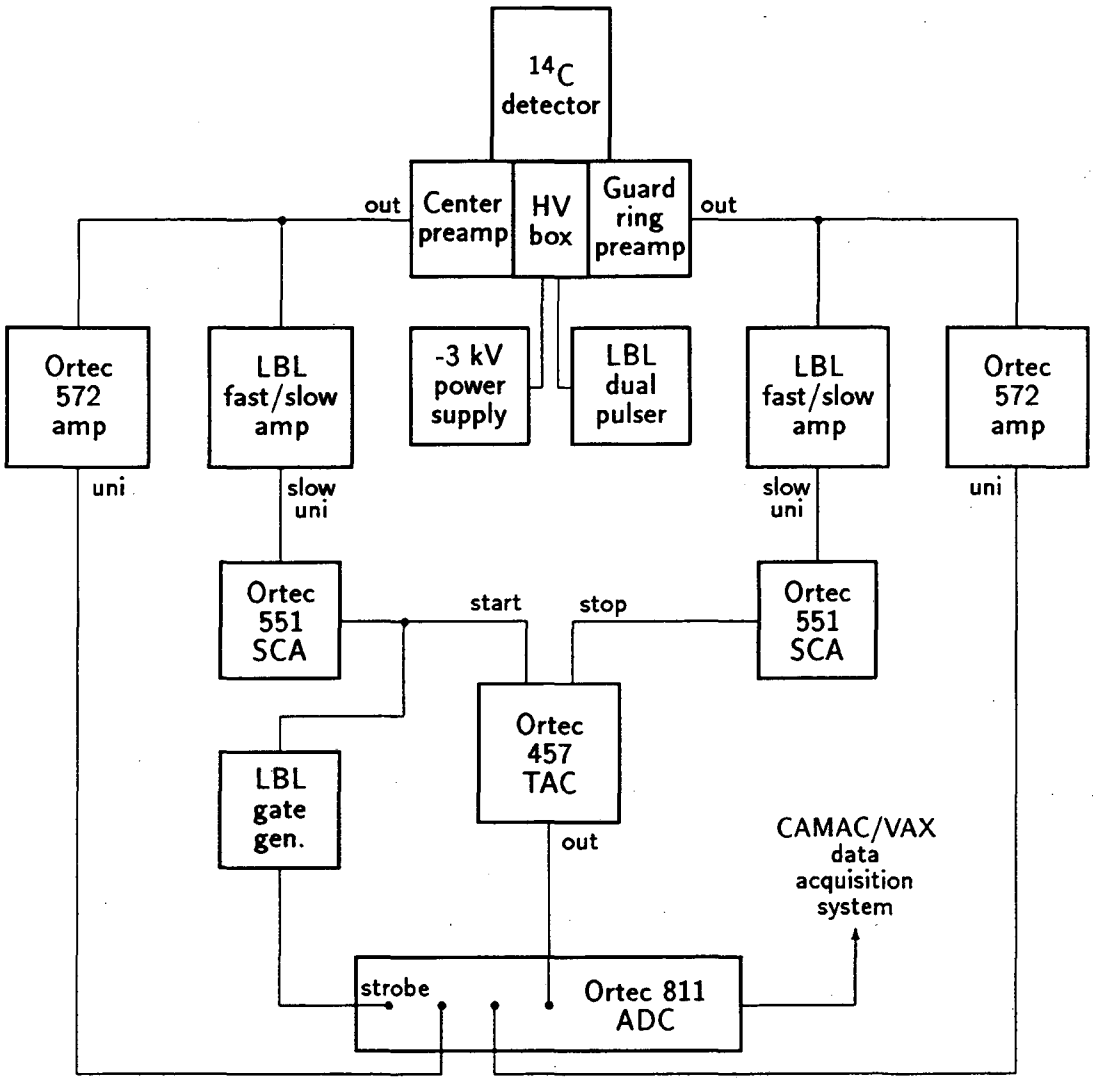

Figure 3.14: Schematic diagram of the second ^{14}C measurement.

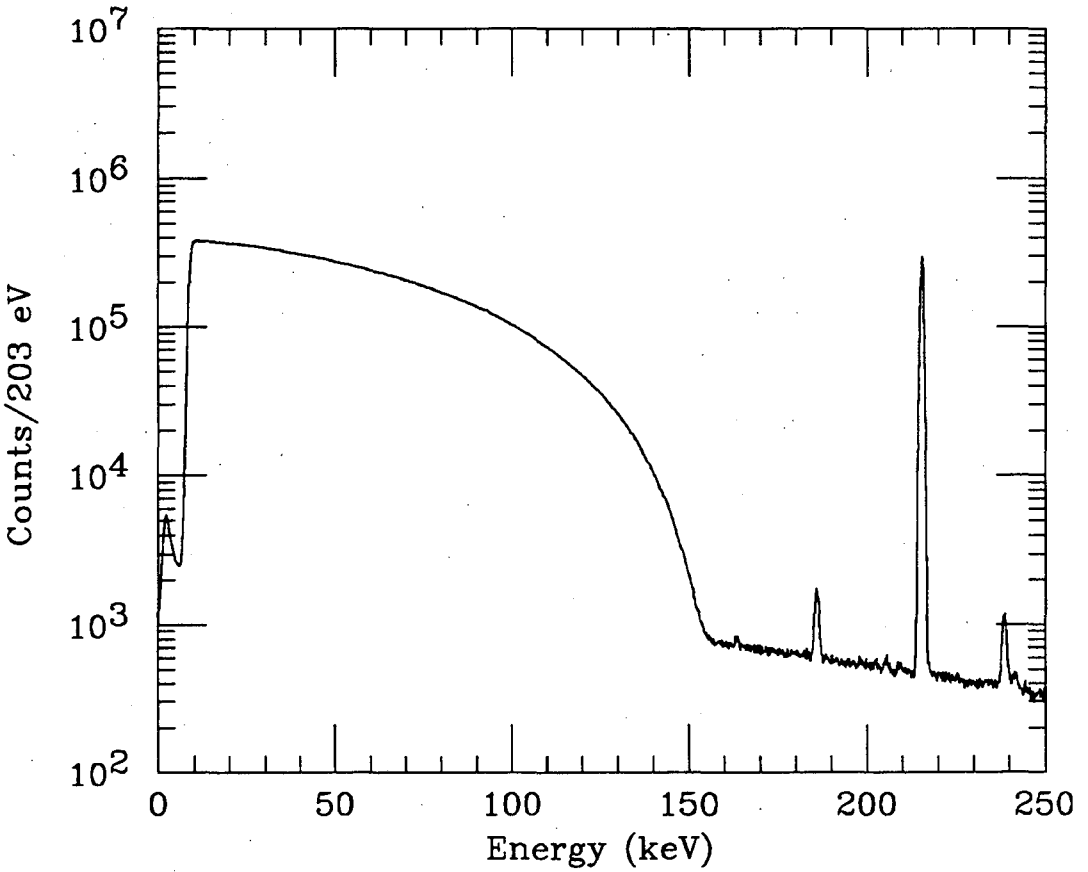

Figure 3.15: The total unvetoed center region ^{14}C beta spectrum collected in 74 days. The large peak is from the pulser.

were collected with the background crystal in the same configuration.

Extracting the true center region ^{14}C spectrum would require vetoing all charge-divided events, at all energies in the guard ring. However the low energy guard ring spectrum (< 5 keV) is dominated by the bipolar pulses in coincidence with events in the center. Vetoing on these bipolar pulses would introduce an energy-dependent efficiency for center region events and distort the beta spectrum. Therefore the goal was to veto as many of the charge-division events as possible without vetoing any of the bipolars. Figure 3.17 shows the TAC spectrum for a portion of the data. The prompt peak contains a narrow component, from the dual pulser, and a broad component, from the true coincidences which are mostly

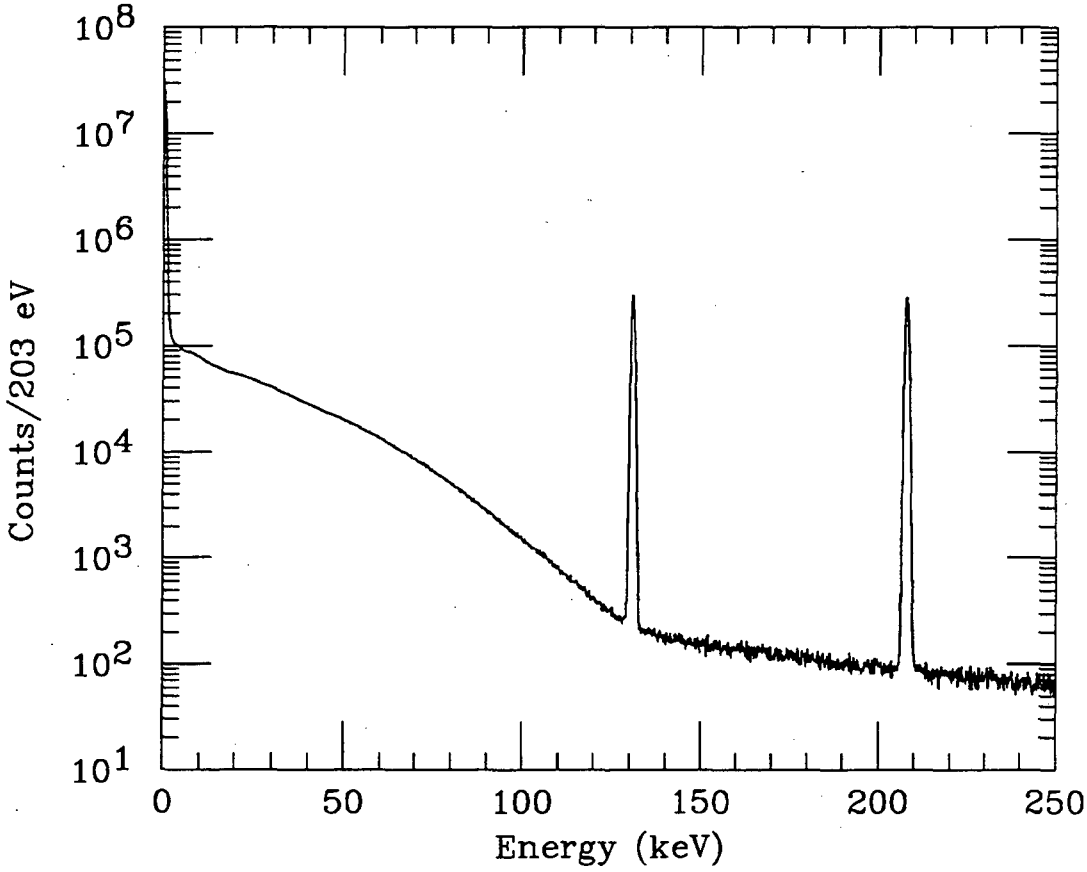

Figure 3.16: The total guard ring spectrum (triggered on center events) collected in 74 days. The two large peaks on the right are from the pulser. The peak below 5 keV is from the bipolar image pulses.

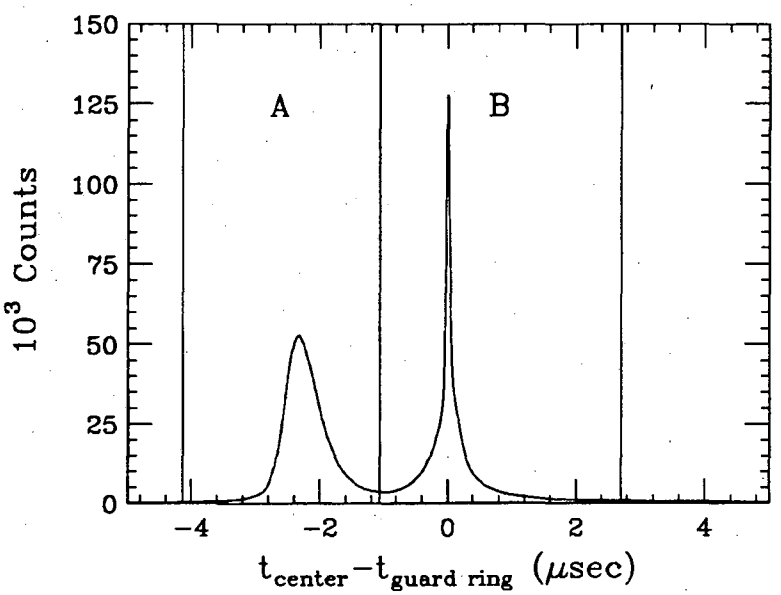

Figure 3.17: Center-guard ring TAC spectrum, showing bipolar coincidences (A), and charge division and pulser coincidences (B).

charge-division events. The peak on the left is from the bipolar pulses. The positive lobe of a bipolar pulse from the guard ring was advanced by about 2 μsec with respect to the associated unipolar pulse in the center, due to the amplifier response. This is fortunate because it allows one to distinguish between the bipolar and true coincidences in the TAC spectrum. This timing advance could also be seen on an oscilloscope using gamma-ray sources. A similar peak should appear at the right side of this plot, caused by bipolar pulses in the center in coincidence with guard signals, but it is absent because they were below the center energy threshold.

Separate TAC gates around the prompt and bipolar coincidence peaks were defined as shown (marked A and B). Figure 3.18 shows the low energy portion of the guard ring spectrum in coincidence with the TAC gates. The highest energy bipolar pulses are at about 5 keV. The prompt coincidence spectrum drops off rapidly below 5 keV, so this was a convenient energy to place the guard ring veto. The two TAC peaks overlap by a few percent, therefore the most effective scheme was to veto all events where the TAC signal was in gate A *or* gate B and the guard

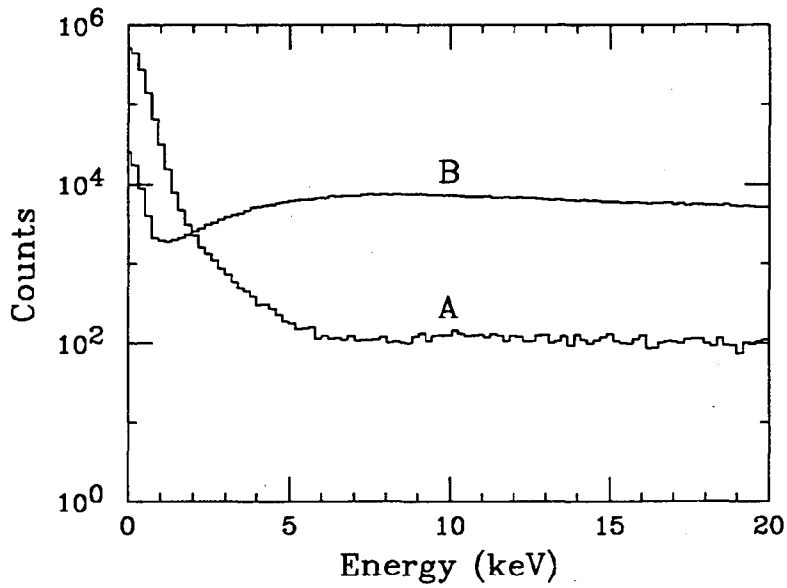

Figure 3.18: The low energy guard ring spectrum gated on the bipolar TAC peak (A) and the prompt TAC peak (B).

ring energy was greater than 5 keV. In this way essentially none of the bipolar signals were vetoed and the only charge division events not vetoed were those that had less than 5 keV in the guard ring. I will refer to the center region ^{14}C spectrum vetoed in this way as spectrum (1), shown in Figure 3.19. Also shown in this figure is the center region spectrum vetoed in the same way except with the guard ring veto threshold at 20 keV. This I will call spectrum (2). Spectrum (2) is equivalent to the vetoed spectrum in the original ^{14}C experiment. In addition to the "good" center region ^{14}C events it contains all the charge division events where the guard ring collected between 5 and 20 keV of equivalent charge. These events were inadvertantly included in the original experiment because the veto threshold was too high. What effect did these charge-division events have on the shape of the spectrum? Figure 3.20 shows the spectrum of these events, the difference between vetoed spectra (2) and (1). It looks roughly like a beta spectrum with an endpoint at about 140 keV, very close to the 17 keV kink position. We can get a better view of the effect by taking the ratio of spectrum (2) and spectrum (1).

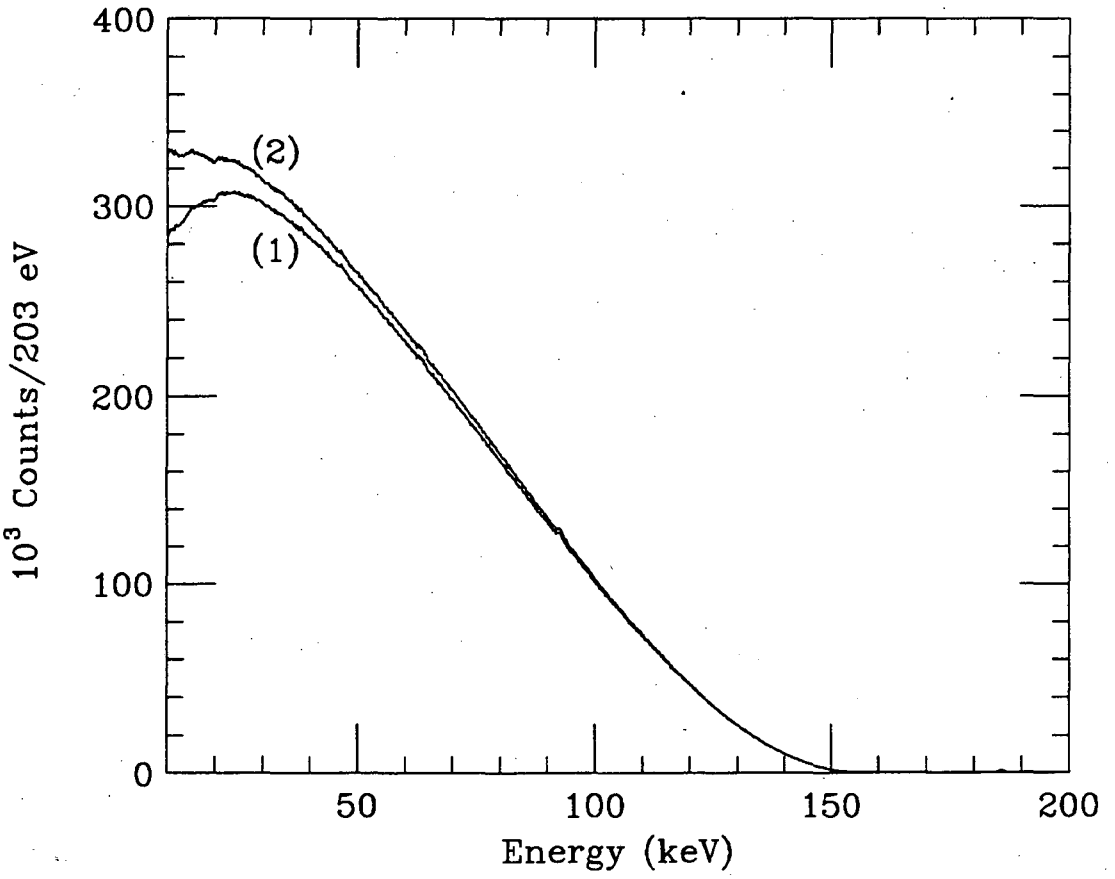

Figure 3.19: Vetoed center region ^{14}C spectrum with the guard ring veto threshold at (1) 5 keV and (2) 20 keV.

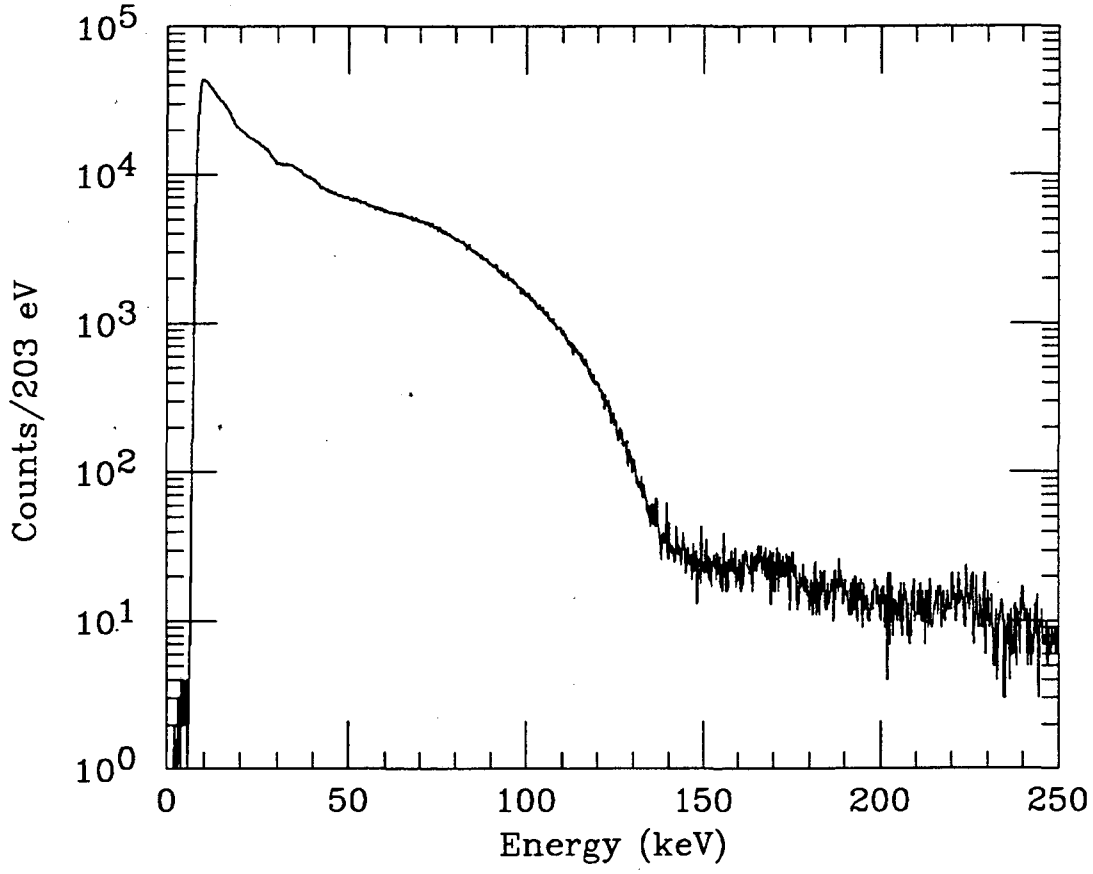

Figure 3.20: Center region spectrum in coincidence with guard ring events with energies between 5 and 20 keV (spectrum (2) minus spectrum (1)).

This is done in Figure 3.21 (after subtracting the background). Compare this plot to the equivalent plot for the 17 keV neutrino effect (Figure 3.8). The effects are remarkably similar in magnitude but the shapes are different. They both begin to rise below about 140 keV, but the older data shows a more sudden jump at that energy, more akin to the threshold expected for a massive neutrino admixture.

The new data were fit to the theoretical beta spectrum in a number of different ways. The results of fitting spectrum (2) are summarized in Table 3.3. Good fits were obtained in the energy region 100–160 keV. The previous result of a 16.6 keV neutrino with $\sin^2\theta = 1.25\%$ is now excluded at 80% CL ($\Delta\chi^2 = 2$). The shape factor a is now in agreement with the CVC predicted value of -0.41

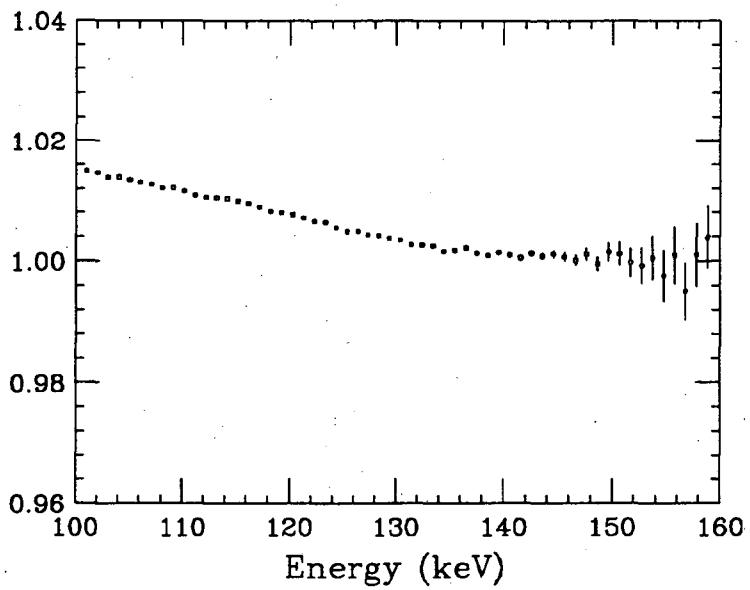

Figure 3.21: Vetoed spectrum (2) divided by vetoed spectrum (1), after subtracting background.

MeV^{-1}. Fits to a wide energy region, 50–160 keV, are still somewhat poor but greatly improved from the original experiment. The data/fit for the fit in the third column of Table 3.3 is shown in Figure 3.22. A small amount of distortion is evident. The best-fit values of the shape factor and endpoint energy are lower for this region, presumably due to this distortion. The 1.25%, 16.6 keV neutrino is rejected in this energy region as well.

Spectrum (1), which should be equivalent to the vetoed spectrum in the original experiment, was also fit. The results of these fits are shown in Table 3.4. The shape factor and endpoint energies are consistent with those of the original vetoed spectrum, but the preference for a 17 keV neutrino is gone. The 1.25%, 16.6 keV neutrino is now excluded at 90% CL ($\Delta\chi^2 = 3$). Apparently something changed during the two years that separate the two measurements. A close examination of the charge-division coincidence spectrum may provide a clue. Figure 3.23(top) shows the center region vs. guard ring 2-D coincidence plot for six days of data collected in May 1992. This is simply a magnified view of Figure

Table 3.3: Results of fitting ^{14}C vetoed spectrum (2) (uncertainies are 1σ).

Kinetic energy region fit (keV)	100–160	100–160	50–160	50–160
Data points	60	60	110	110
χ^2	66.8	68.8	173.1	185.9
E_0 (keV)	155.67 ± 0.08	155.75	155.46	155.55
m_2 (keV)	16.6[a]	16.6[a]	0[a]	16.6[a]
$\sin^2\theta$ (%)	0.4 ± 0.6	1.25[a]	0[a]	1.25[a]
a (MeV^{-1})	-0.45 ± 0.04	-0.46	-0.32	-0.34
Background norm. factor	6.81 ± 0.13	6.88	7.19	7.13
Rad. correction (Figure 3.7)	$R'(E)$	$R'(E)$	$R'(E)$	$R'(E)$

[a]Held fixed during fit

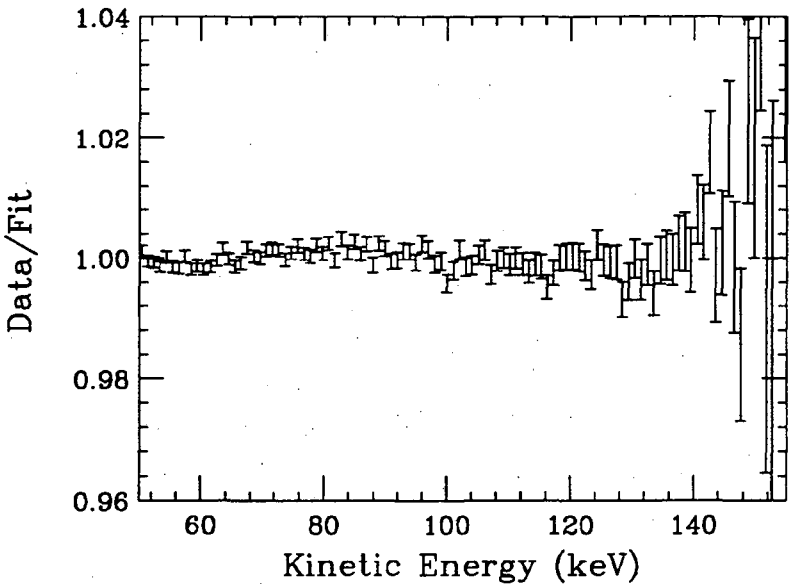

Figure 3.22: Data/fit of ^{14}C spectrum (2) fit to the theoretical beta spectrum (Table 3.3, third column).

3.9. A similar plot for seven days of data collected in December 1993 is shown at the bottom of the figure. The data were taken with different resolutions, but it is clear from these plots that the relative positions of the coincidence bands have changed. The isolated band, labeled *a*, has apparently rotated up by about 4° in the recent data. The broad band, labeled *b*, has spread out and is now resolved into four separate bands. The prominant band, labeled *c*, at about 15° in the older data seems to have rotated down to 6°. Other changes are also visible. What could have caused this? The detector was removed several times from the cryostat during this time period and its surfaces were chemically treated, but it was never heated above room temperature so the carbon clusters cannot have moved. However, it is known that the electric field lines in the guard ring are very sensitive to the chemical condition of the surface at the edges of the crystal. This was clearly demonstrated by the "banana"-shaped coincidences present when the ^{141}Ce tests were done (see Figure 3.11). They revealed a severe surface channel. The crystal was subsequently removed and chemically treated; and when it was reinstalled

Table 3.4: Results of fitting ^{14}C vetoed spectrum (1) (uncertainies are 1σ).

Kinetic energy region fit (keV)	100–160	100–160
Data points	60	60
χ^2	71.0	74.1
E_0 (keV)	155.66 ± 0.07	155.76
m_2 (keV)	16.6[a]	16.6[a]
$\sin^2\theta$ (%)	0.1 ± 0.6	1.25[a]
a (MeV^{-1})	-0.63 ± 0.05	-0.64
Background norm. factor	6.77 ± 0.14	6.69
Rad. correction (Figure 3.7)	$R'(E)$	$R'(E)$

[a]Held fixed during fit

and tested the "banana" coincidences were gone. It is reasonable to expect that changing the shape of the electric field in the guard ring will affect the shape of the field lines under the groove. This will in turn change the proportion of charge split between the center and guard ring for a particular carbon cluster under the groove, causing the corresponding coincidence band to rotate. If the coincidence bands have changed then perhaps this explains why the effect of the 20 keV veto threshold (Figure 3.21) no longer has the shape of a 17 keV neutrino (Figure 3.8). This is a plausible explanation but it cannot be demonstrated for certain.

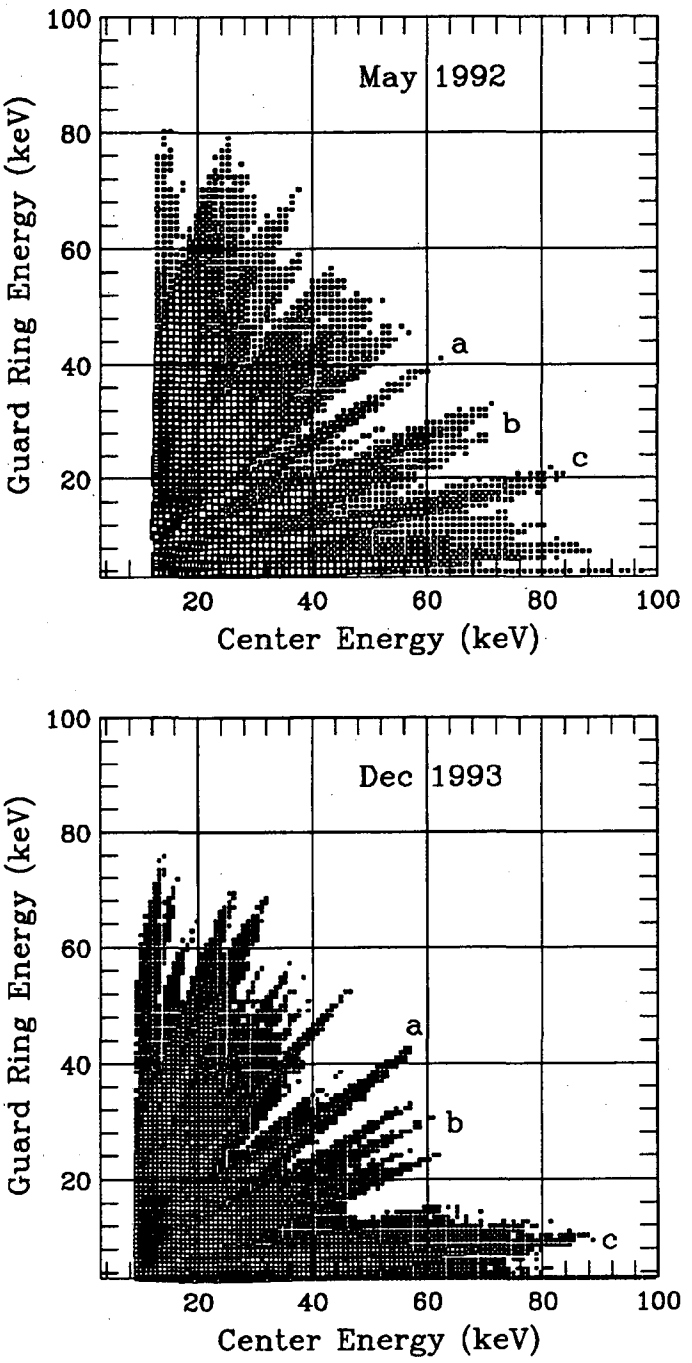

Figure 3.23: Center vs. guard ring 2-D coincidence plots for data taken in May 1992 (top) and December 1993 (bottom).

3.7 Conclusions

Much progress has been made in understanding the behavior of the ^{14}C-doped germanium detector since the first experiment in 1991. The demonstrated presence of charge division under the groove and carbon clusters invalidates the original analysis that showed evidence of a 17 keV neutrino admixture in the spectrum. The response function used in that analysis was clearly incorrect. We cannot be certain exactly what caused the neutrino effect, but there is strong circumstantial evidence that it was due to contamination of the beta spectrum by decays under the anode groove where the charge was split and the guard ring collected less than 20 keV of equivalent charge. This contamination spectrum has an endpoint very close to the kink position (about 140 keV, see Figure 3.20) and about the correct magnitude (1.5%, see Figure 3.21). There is also some evidence that the shape of this effect may have changed over time (Figure 3.23). In any case, the most recent data no longer supports the presence of 17 keV neutrino emission in the ^{14}C beta spectrum.

Fits of the high energy portion of the recent data (100–160 keV) to the theoretical spectrum gives a linear shape factor (-0.45 ± 0.04 MeV^{-1}) in good agreement with the CVC-predicted value (-0.41 MeV^{-1}) [100] for weak magnetism. Fitting a wider region of the spectrum shows deviation from the theory and gives a smaller shape factor, so a strong confirmation of the CVC prediction cannot be made. The inability to completely separate bipolar from charge division coincidences remains a systematic problem in the experiment.

The observed endpoint energy in all the spectra (old and new) is about 700 eV below the accepted value which is strongly weighted by the 1974 mass spectrometer measurement of Smith and Wapstra [105]: 156.476 ± 0.005 keV. The gamma-ray calibration of the ^{14}C-doped detector was excellent (see Figure 3.6) in the vicinity of the endpoint and should be correct for events fully contained in the center region. Of course, betas originating in carbon clusters will lose some energy.

The ^{14}C coincidence bands (Figure 3.9) and the position-sensitive detector (Figure 3.13d) both indicate a maximum cluster size of about 10^{11} atoms. A 150 keV beta starting from the center of such a cluster will lose about 400 eV in the carbon [91]. The average energy loss for all the carbon clusters should be much less, so this cannot completely explain the difference. I believe there is still a significant discrepancy in the ^{14}C endpoint energy. This will hopefully be resolved by future experiments.

Chapter 4

A Kink Search in the ^{55}Fe IBEC Spectrum

4.1 A Local Kink Search

Recall from Section 1.4 that the effect of a massive neutrino admixture in a beta spectrum can be expressed as

$$\frac{dN(E)}{dE} \propto \frac{dN(E, m_\nu = 0)}{dE} S(E) \tag{1.16}$$

with

$$\begin{aligned} S(E) &= 1 + \tan^2\theta \left[1 - \frac{m_2^2}{(Q-E)^2}\right]^{\frac{1}{2}} \quad \text{for} \quad E \leq Q - m_2 \\ &= 1 \quad \text{for} \quad E > Q - m_2. \end{aligned} \tag{1.17}$$

When searching for a massive neutrino admixture in beta decay, the experimental task is to determine if $S(E)$ is exhibited in the data. This function contains a slope discontinuity (kink) at $E = Q - m_2$ and a difference in amplitude above and below the kink. As discussed in Section 2.5, if a wide energy region of the experimental spectrum is fit to (1.16), most of the sensitivity to $S(E)$ comes from the difference in amplitude rather than the shape of the kink. An unexpected smooth distortion

in the spectrum, caused by some experimental artifact, can correlate with this amplitude difference and effectively mimic or hide the effect of a massive neutrino. All of the first generation 17 keV neutrino experiments (Table 2.1) can be criticized by this argument, since none had convincingly demonstrated that their systematics were understood at the level of 1% neutrino mixing.

An experiment that is especially sensitive to the local slope discontinuity in $S(E)$ and relatively insensitive to the overall shape would be very helpful in resolving the 17 keV neutrino controversy. This kink is a characteristic signature of the presence of a massive neutrino, and a local search for such a feature should not be affected by smooth systematic distortions. It is clear that such an approach would require high statistics and a different type of analysis. To this end, two data analysis techniques for beta spectra were developed, both designed to distinguish a smooth spectrum from one with a neutrino kink in it.

The first technique involves taking the second derivative of the experimental spectrum. The second derivative of a discrete spectrum can be defined in analogy to the second derivative of a continuous function. If $N(i)$ is the number of counts in the i^{th} bin then the second derivative $D_2(i)$ is:

$$D_2(i) = \frac{N(i-1) + N(i+1) - 2N(i)}{(\Delta E)^2} \tag{4.1}$$

where ΔE is the bin width. The second derivative has been used previously to effectively reveal the presence of γ-ray lines too small to be seen in raw spectra [106, 107]. The second derivative of a slope discontinuity will produce a delta function. With finite detector resolution this becomes a peak, as shown in Figure 4.1. The statistical dispersion of data points in the second derivative of a spectrum is much larger than in the raw spectrum itself, so high statistics are needed to see the structure. It is obvious that this method will still be effective in the presence of smooth spectral distortions. While the second derivative method produces a result convincing to the eye, quantifying the result presents a difficulty. Adjacent points are covariant, unlike in an ordinary spectrum, so a χ^2-type analysis is unwieldy

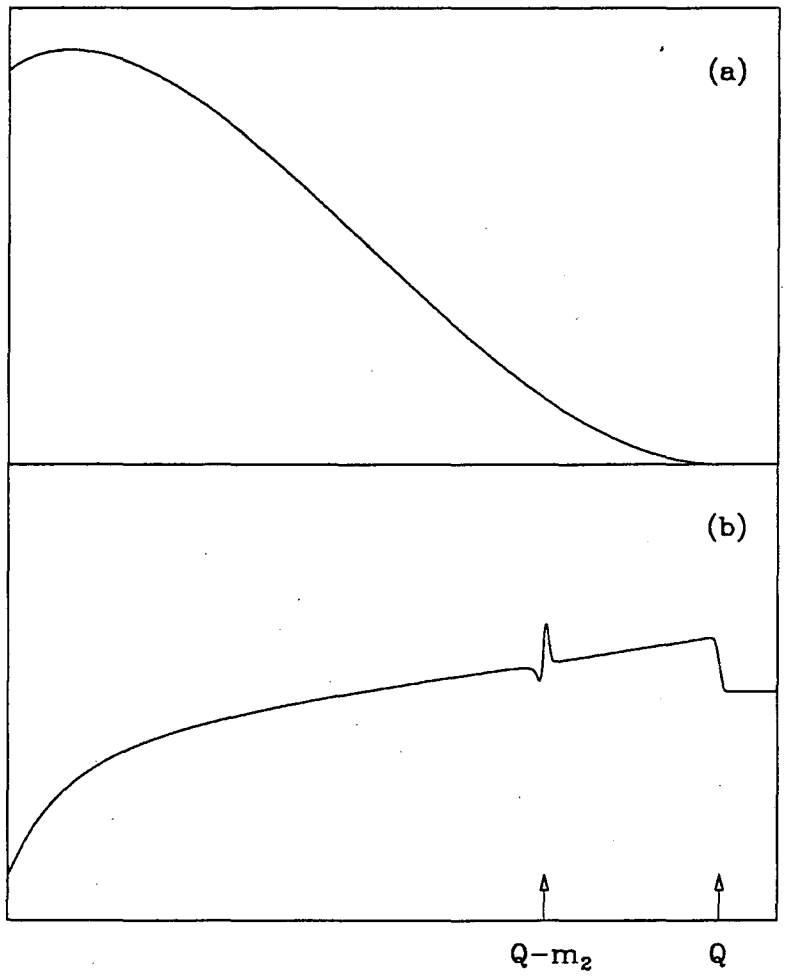

Figure 4.1: (a) Fermi beta function, including a massive neutrino with 1% mixing, convoluted with a gaussian resolution function. The presence of the massive neutrino cannot be seen by eye. (b) The kink is clearly seen in the second derivative of the same function.

and a separate approach is desirable.

The second analysis technique consists of fitting a small portion of the spectrum to a polynomial. If no kinks are present we expect a narrow region of a beta spectrum to be smooth, and well fit by a low order polynomial. If a kink caused by emission of a massive neutrino is present in the region, it should be well fit by this polynomial multiplied by $S(E)$. Tests using pseudodata (see Section 4.3) showed that a third order polynomial works well; i.e. the following function can be used to fit a narrow region of the data:

$$P(E) = (a_0 + a_1 E + a_2 E^2 + a_3 E^3) S'(E) \tag{4.2}$$

where $S'(E)$ is $S(E)$ convoluted by a gaussian with a width corresponding to the measured detector response. If the χ^2 of the fits are sufficiently good, this analysis will give an appropriate quantitative result. Smooth spectral distortions will be accommodated by the polynomial and will not affect sensitivity to the kink.

Clearly, the second derivative method and polynomial fit method are mathematically related. The second derivative of a third order polynomial gives a straight line. Any detailed structure in the second derivative, for example a peak caused by a massive neutrino kink, correspond to powers higher than three in the Taylor expansion of the function; and therefore will be seen in the fit to (4.2).

4.2 The Experiment

The IBEC photon spectrum of ^{55}Fe was chosen for a local kink search experiment. This isotope is available commercially in large quantities and is relatively long-lived, so it was suitable for a high-statistics experiment. A photon source was preferred over a beta source because source scattering is weak, allowing use of a large source volume; and a commercial HPGe photon detector could be used to collect the data, making the setup relatively simple. The electron capture of ^{55}Fe is an allowed ground-state to ground-state transition with a Q_{EC} of 231.7 $\pm$ 0.7 keV, an IBEC probability of 3.25×10^{-5}, and a half-life of 2.73 years [90]. There is also a second-forbidden decay to the $7/2^-$ 126 keV level in ^{55}Mn, but the branch is negligibly small (1.3×10^{-9} [107]).

A sample of ^{55}Fe was purchased from New England Nuclear Company. Initial γ-ray counting revealed impurities of ^{60}Co, ^{54}Mn, ^{123}Te, ^{127}Te, and ^{59}Fe, so the sample was purified using ion exchange column chemistry. The ^{59}Fe could not be removed this way, but it has a short half-life (44.5 days) so the source was allowed to decay for about four months prior to beginning the actual experiment. The total electron-capture strength of the final purified source was about 25 mCi. The source was sealed inside a plastic container with 1-mm-thick walls and attached to the face of an Ortec 109-cm^3 coaxial HPGe detector. An additional absorber, consisting of 0.06-mm-thick copper and 0.05-mm-thick aluminum foils, was placed between the source and detector to help suppress Mn x rays from the ^{55}Fe electron capture decays. The x-ray intensity was suppressed by a factor of about 3×10^6. The detector and source were placed inside an anitcoincidence shield consisting of a 30-cm by 30-cm annular NaI detector and a 7.5-cm by 15-cm plug NaI detector. These NaI detectors were used to veto Compton-scattered events from the source, external background radiation, and ^{59}Fe γ rays that appear in coincidence. Additional lead shielding was placed around the detectors. The experimental setup is shown schematically in Figure 4.2. The initial ^{55}Fe IBEC count rate in the Ge

detector was approximately 8000 sec^{-1}.

A total of 182 days of ^{55}Fe data were collected in 2–3 day running intervals on a PC-based system using the Ortec MAESTRO data acquisition software. Three separate spectra were recorded simultaneously on three Ortec 916A analog-to-digital converters (ADC's): (A) Ge detector singles (no vetos), (B) Ge detector with pileup rejection (PUR) using the pileup inhibit veto from the Ortec 572 amplifier, and (C) Ge detector with PUR and NaI veto. The PUR and NaI veto thresholds were measured to be 27.0 and 29.5 keV, respectively. The amplifier shaping times were 1μs for the 572's and 0.25μs for the NaI amplifiers. Each spectrum contained 4096 channels with 133 eV/Ch (A), 147 eV/Ch (B), and 130 eV/Ch (C). The energy scale for each ADC was measured with external calibration sources. Linear calibration fits and residuals are shown in Figure 4.3. The calibration was also monitored for individual ^{55}Fe runs using the Pb x rays and ^{59}Fe lines in each spectrum. An offset of up to two channels (positive or negative) as needed was added to each run prior to summing them together in order to correct for minor gain shifts over time. A small number of runs required shifts of more than two channels. These runs were not included in the final data sets.

Background spectra were accumulated between ^{55}Fe measurements, and separate sources of ^{59}Fe, ^{60}Co, and ^{54}Mn were also measured. These were then subtracted by normalizing to the corresponding peaks in the ^{55}Fe raw spectra. All lines in the background and ^{55}Fe spectra from 50–400 keV were identified and accounted for by normal room background and the above-mentioned impurities. A complete list is given in Table 4.1. The total summed raw data collected in ^{55}Fe spectra A, B, and C, with the corresponding peak-normalized background and impurity spectra, are shown in Figure 4.4a-c. Comparing these, we can see that the NaI veto suppressed about 82% of the ^{59}Fe, 81% of the ^{60}Co and ^{54}Mn, and 68% of the external background, at energies below the ^{55}Fe endpoint. After subtraction, ^{55}Fe spectra A, B, and C contained 1.70×10^7, 1.47×10^7, and 1.13×10^7 counts/keV,

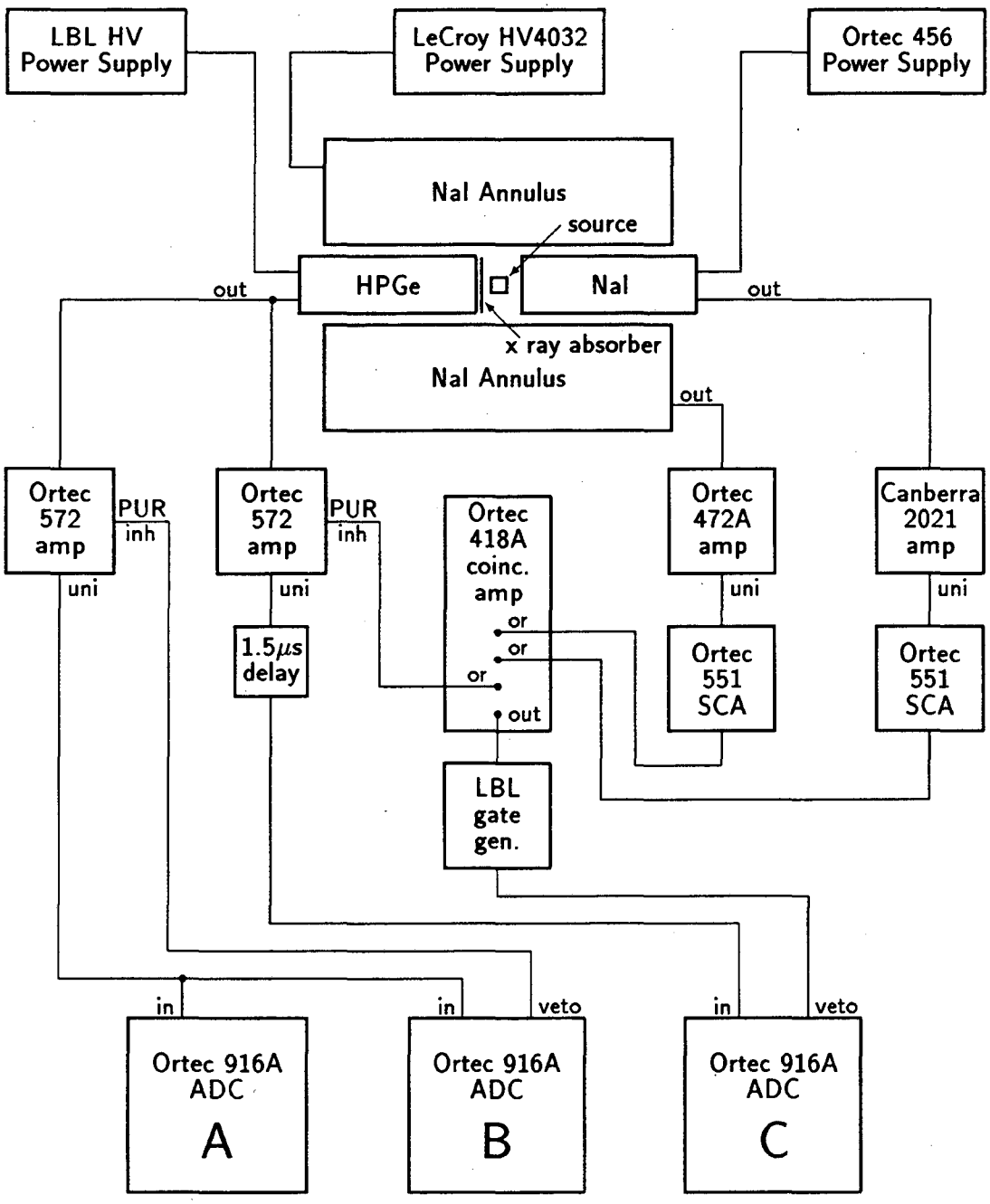

Figure 4.2: Schematic diagram of the ^{55}Fe IBEC experiment.

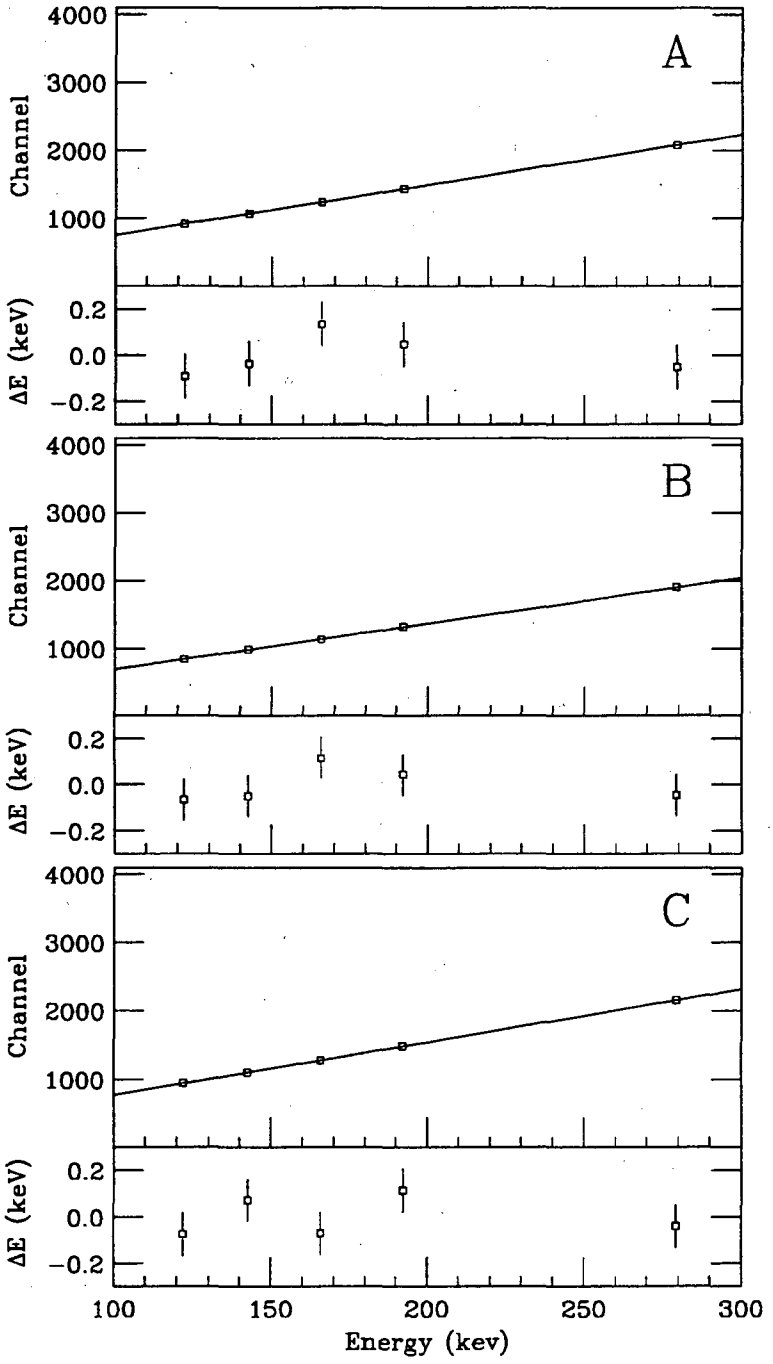

Figure 4.3: Linear calibration fits and residuals for ADC's A (no vetos), B (PUR only), and C (PUR and NaI veto).

respectively, at 208 keV (the expected kink position for a 17 keV neutrino).

At the conclusion of the experiment, it was discovered that the peak to continuum ratio of the background in all three spectra varied significantly from run to run. This was probably due to operation of the 88-inch Cyclotron located in the same building, and other research activities in the immediate environment. As a result, it was not possible to simultaneously normalize the peak and continuum areas of the background spectra to the ^{55}Fe. For example, normalizing on the peaks left a residual background continuum of about 2000 counts/channel in ^{55}Fe spectrum C, which is about 0.1% of the total at 208 keV. This was not expected to affect the results of the analysis, and to verify that it did not, the background was normalized in two ways, first on the peaks, and then on the continuum in the region 420–500 keV. The complete analysis was performed on both data sets, with virtually identical results. Further discussions will refer to the peak-normalized, background-subtracted data.

Table 4.1: ^{55}Fe background and impurity lines.

Energy (keV)	Origin	Intensity[a]	Energy (keV)	Origin	Intensity[a]
53.2	^{214}Pb,^{234}U	0.0098	139.7	^{74}Ge(n_{th},γ)^{75}Ge	0.0040
53.4	^{72}Ge(n_{th},γ)^{73}Ge	0.0048	142.7	^{59}Fe	0.4583
59.5	^{241}Am	0.0086	143.8	^{235}U	0.0191
63.3	^{234}Th	0.1450	159.0	^{123}Te	1.4592
66.7	^{72}Ge(n_{th},γ)^{73}Ge	0.0023	163.4	^{235}U	0.0076
72.8	Pb x ray	0.0183	185.7	^{235}U	0.0937
74.8	Bi x ray	0.0548	192.3	^{59}Fe	1.0000
75.0	Pb x ray	0.0282	198.9	^{70}Ge(n_{th},γ)^{71}Ge	0.0078
77.1	Bi x ray	0.0982	205.3	^{235}U	0.0056
84.5	Pb x ray	0.0105	209.4	^{228}Ac	0.0051
84.9	Pb x ray	0.0202	238.6	^{212}Pb	0.1456
86.8	Bi x ray	0.0105	241.9	^{214}Pb	0.0245
87.3	Bi x ray	0.0202	277.3	^{208}Tl	0.0035
87.3	Pb x ray	0.0043	279.2	^{203}Hg	0.0055
92.4	^{234}Th	0.1023	295.1	^{214}Pb	0.0424
92.8	^{234}Th	0.1011	300.0	^{212}Pb	0.0049
94.7	U x ray	0.0043	328.1	^{228}Ac	0.0020
98.4	U x ray	0.0069	335.0	^{59}Fe	0.0550
112.8	^{234}Th	0.0084	338.4	^{228}Ac	0.0198
120.9	^{234}U	0.0026	351.9	^{214}Pb	0.0759
122.1	^{57}Co	0.0035	382.3	^{59}Fe	0.0026

[a]Intensity is the peak area after normalization measured relative to the 192 keV line from ^{59}Fe, using the spectra from ADC C (PUR and NaI veto).

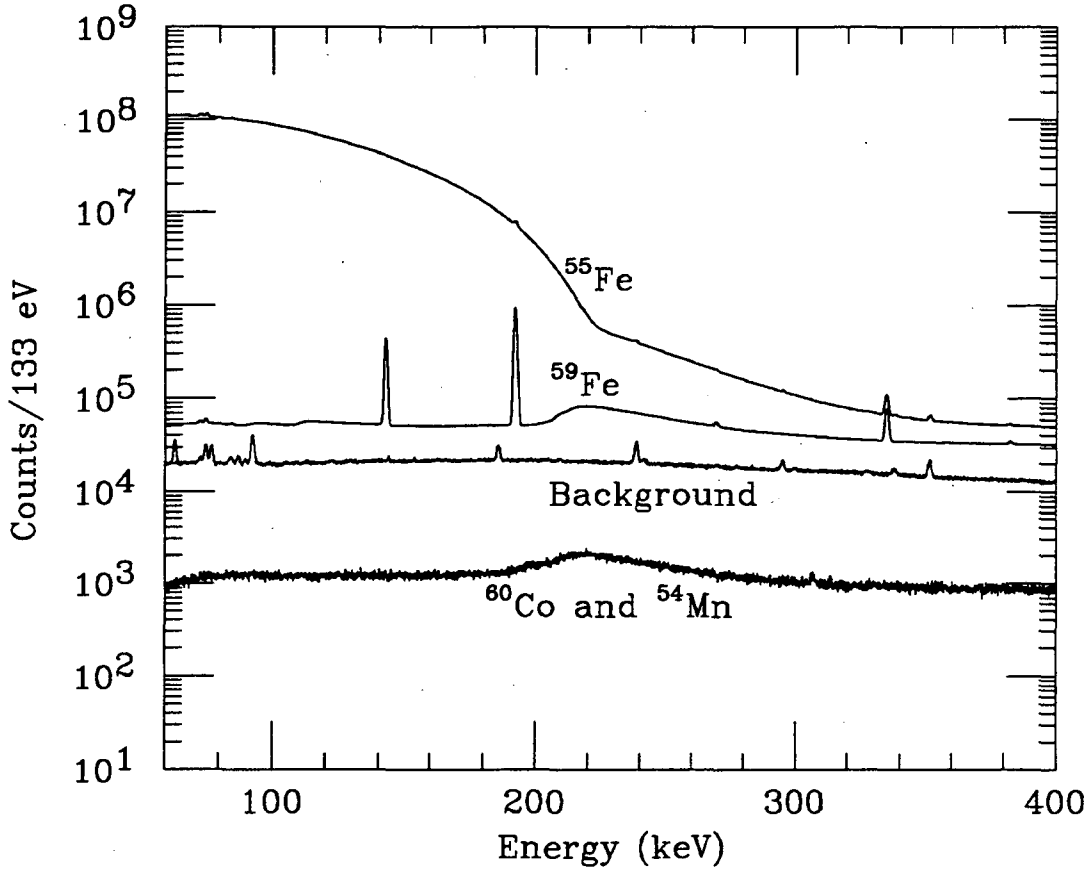

Figure 4.4a: Total raw data in ^{55}Fe spectrum A (no vetos) with normalized background and impurity spectra.

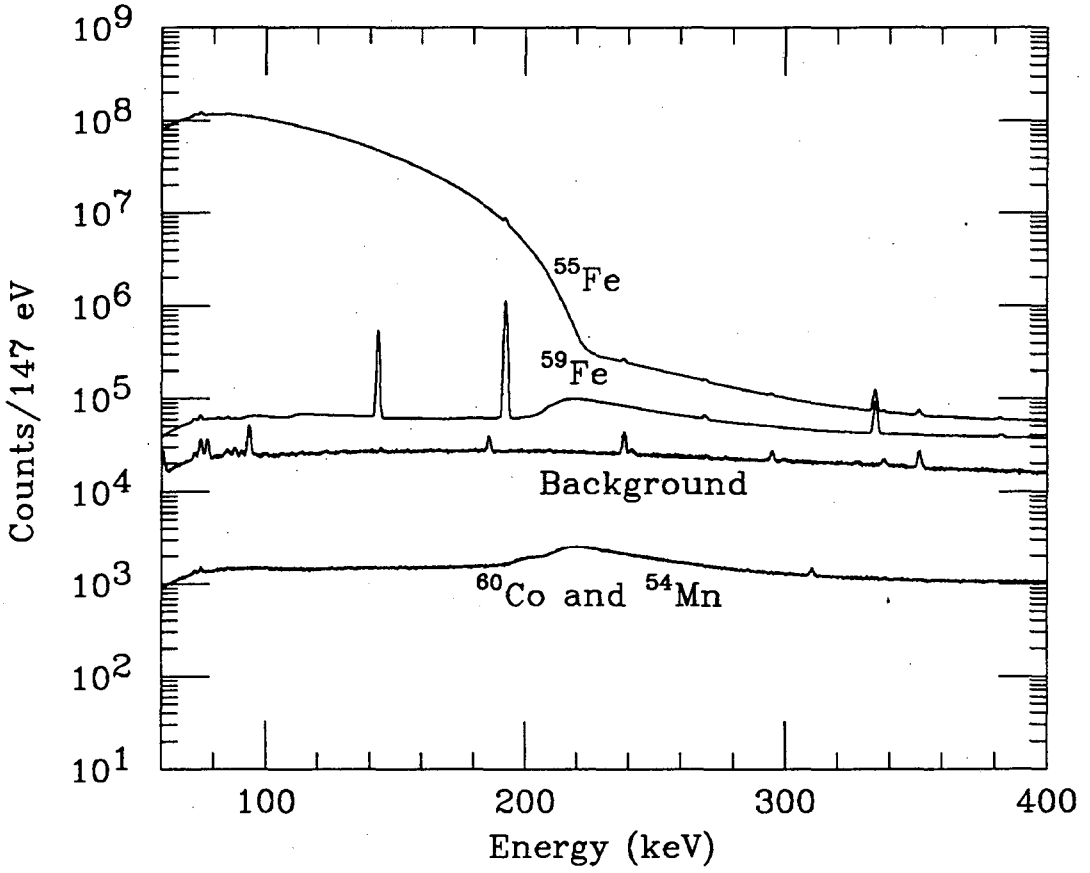

Figure 4.4b: Total raw data in ^{55}Fe spectrum B (PUR only) with normalized background and impurity spectra. The falloff below 80 keV is due to the ADC threshold setting.

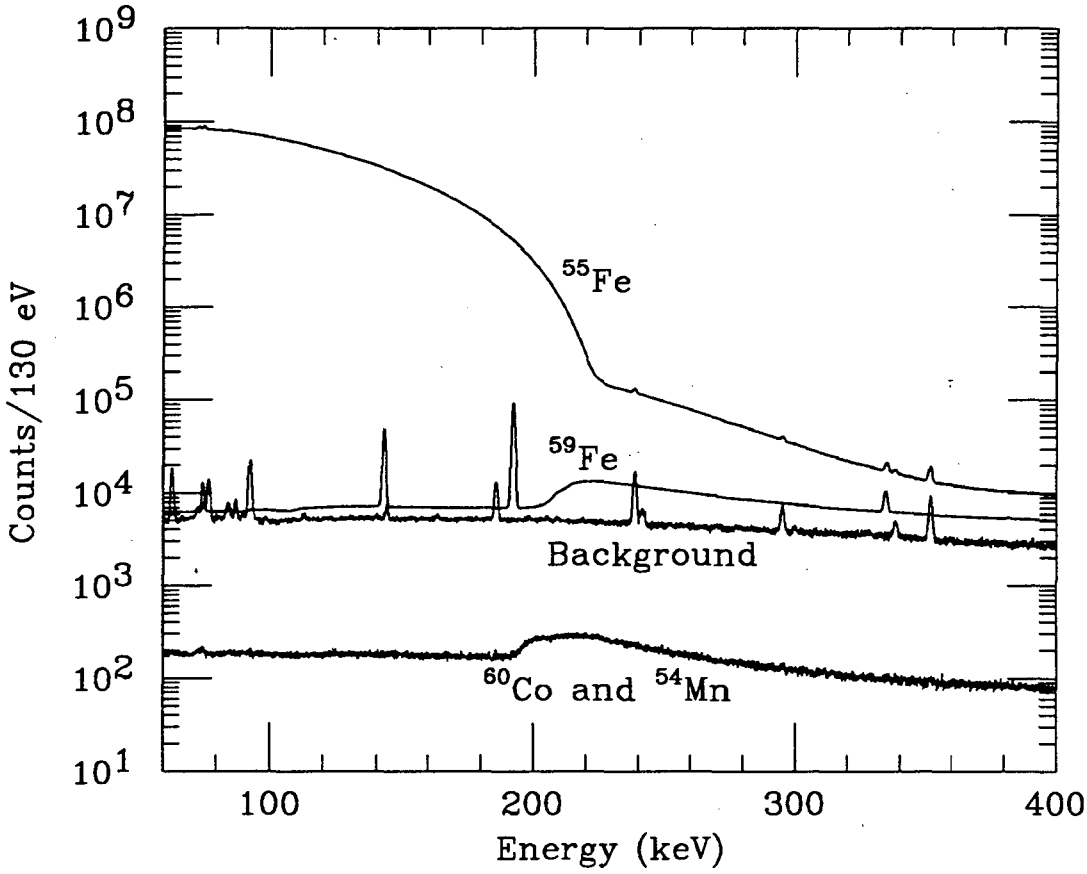

Figure 4.4c: Total raw data in ^{55}Fe spectrum C (PUR and NaI veto) with normalized background and impurity spectra.

4.3 Pseudodata Tests

Use of the second derivative and polynomial fit methods described in Section 4.1 does not require knowledge of the theoretical spectral shape or any experimental corrections to it, provided they form a sufficiently smooth function of energy. A kink caused by massive neutrino emission will stand out against the smooth underlying spectrum. Still, it is worthwhile to test these methods using realistic spectra, with and without the presence of a neutrino kink, to judge their effectiveness and obtain a measure of their sensitivity. To do this, a computer program was written to generate pseudodata spectra simulating the ^{55}Fe data of ADC C. This program began with the theoretical ^{55}Fe IBEC spectrum, incorporated the measured experimental efficiency, response function, and pileup; and randomized the points using Poisson statistics.

The theoretical energy spectrum for radiative electron capture from an ns ($l = 0$) state, including the effects of the Coulomb field on the intermediate virtual electron, was first calculated by Glauber and Martin [108, 109]. For relatively light nuclei and IBEC photon energies less than the electron mass the nonrelativistic calculation is appropriate. In this case the ratio of radiative capture to that for non-radiative K capture is given by [109]:

$$\frac{d\omega_{ns}(k)}{\omega_K dk} = \frac{\alpha}{\pi}\frac{|\phi_{ns}(0)|^2}{|\phi_{1s}(0)|^2}\frac{k\,(q_{ns}-k)^2}{q_{1s}^2}R_{ns}(k) \tag{4.3}$$

where k is the photon energy, q_{ns} is Q_{EC} minus the daughter atomic excitation energy, and R_{ns} is the Coulomb correction factor, defined by

$$R_{ns}(k) = \frac{1}{2}\left(1 + B_{ns}^2(k)\right). \tag{4.4}$$

Glauber and Martin calculated B_{ns} for the $1s$ and $2s$ states [109]:

$$B_{1s}(k) = 1 - \frac{4\eta_1}{3\,(1+\eta_1)}\left\{1 + \frac{\eta_1}{1-\eta_1}\left[2K\left(\lambda_1\right) - 1\right]\right\} \tag{4.5}$$

$$B_{2s}(k) = 1 - \frac{\eta_2}{(1-\eta_2^2/4)}\left(\frac{4}{3}+\frac{5}{6}\eta_2\right) - \frac{\eta_2^2}{(1-\eta_2^2/4)^2}\left[\frac{8}{3}\left(1-\eta_2^2\right)K(\lambda_2) - 3 - \eta_2 + \frac{5}{4}\eta_2^2\right] \quad (4.6)$$

with

$$\eta_n(k) = \left(\frac{1}{n^2}+\frac{k}{E_{1s}}\right)^{-\frac{1}{2}} \quad (4.7)$$

and

$$\lambda_1 = \frac{1-\eta_1}{1+\eta_1}, \qquad \lambda_2 = \frac{2-\eta_2}{2+\eta_2}. \quad (4.8)$$

The function $K(\lambda)$ is defined as:

$$K(\lambda) = \lambda\int_0^1 \frac{x^{-\eta}}{1+\lambda x}dx \approx \ln(1+\lambda) - \eta\sum_{j=1}^{\infty}\frac{(-\lambda)^j}{j\,(j-\eta)} \quad (4.9)$$

and in (4.7) E_{1s} is the $1s$ electron binding energy. In a nonrelativistic calculation, non-radiative electron capture from a p-wave is forbidden because the np wave functions are vanishingly small at the nuclear surface. However, radiative p-capture is allowed when the photon is emitted in an electric dipole transition. The intermediate electron is then captured as an s-wave.* Glauber and Martin calculated the p-capture spectrum [109]:

$$\frac{d\omega_{np}(k)}{\omega_K dk} = \frac{4}{\pi Z^2\alpha}\left[Q_{np}(k)\right]^2\frac{k\,(q_{np}-k)^2}{q_{1s}^2}S_{np}. \quad (4.10)$$

De Rujula's calculations of the integrals Q_{np} [111] were used:

$$Q_{2p}(\eta_2) = \frac{\eta_2^2}{2\,(1-\eta_2)}\int_0^1 d\nu\,(1-\nu)\,\nu^{1-\eta_2} \cdot\left(\frac{-2A^2\eta_2 + \left[12+\eta_2^2\,(1-\nu)\right]A - 8\eta_2\,(1-\nu)}{A^5}\right) \quad (4.11)$$

with

$$A \equiv \left(1+\frac{\eta_2}{2}\right)\left(1+\nu\frac{2-\eta_2}{2+\eta_2}\right) \quad (4.12)$$

*This process seems to violate the exclusion principle if the lower s states are already occupied. However, the reverse-time-ordered process, where an s-wave electron is captured followed by an electric dipole transition of a p-wave electron into the vacated shell, is allowed. This was first discussed by Feynman [110, 111].

and

$$Q_{3p}(\eta_3) = \frac{48\eta_3^2}{81\,(1-\eta_3)\,(2-\eta_3)} \int_0^1 d\nu\,(1-\nu)\,\frac{\nu^{2-\eta_3} N}{C^7} \tag{4.13}$$

with

$$C \equiv \left(1+\frac{\eta_3}{3}\right)\left[1+\frac{\nu\,(3-\eta_3)}{(3+\eta_3)}\right], \tag{4.14}$$

$$\begin{aligned} N \;\equiv\; & \eta_3\,(\eta_3-1)\,C^4 - \left[12+\eta_3\,(\eta_3-1)\,(1-\nu)\right]\eta_3 C^3 \\ & + \left[48+16\eta_3^2\,(1-\nu)+\frac{2}{9}\eta_3^3\,(\eta_3-1)\,(1-\nu)^2\right] C^2 \\ & - \left[\frac{1}{9}\eta_3^2\,(1-\nu)+2\right] 40\,(1-\nu)\,\eta_3 C + \frac{80}{3}\eta_3^2\,(1-\nu)^2 . \end{aligned} \tag{4.15}$$

and η_n is given in (4.7). Note that the $Q_{np}(k)$ contain poles at the K shell binding energy. At that energy the process is equivalent to ordinary (non-radiative) $1s$-capture and x ray emission. The screening correction S_{np} in (4.10) corrects for the screening of the initial state wave functions by the electron cloud. Calculated values of S_{np} are given in [109]. The $\phi_{ns}(0)$ in (4.3) were taken from the relativistic Hartree-Fock-Slater calculations of Martin and Blichert-Toft [112] which implicitly include screening corrections. The theoretical ^{55}Fe IBEC spectra for $1s$-, $2s$-, $2p$-, and $3p$-capture were calculated numerically from the above formulae for photon energies above 10 keV. A plot of these is shown in Figure 4.5. An admixture of a massive neutrino was incorporated by multiplying (4.3) and (4.10) by $S(k)$:

$$\begin{aligned} S(k) &= 1+\tan^2\theta\left[1-\frac{m_2^2}{(q_{nl}-k)^2}\right]^{\frac{1}{2}} && \text{for} \quad k \le q_{nl}-m_2 \\ &= 1 && \text{for} \quad k > q_{nl}-m_2 \end{aligned} \tag{4.16}$$

which is equivalent to $S(E)$ in beta decay.

The photon attenuation due to the x-ray absorber was calculated using

$$P_{abs}(k) = \exp\left[-0.153(k)^{0.654}\right] \tag{4.17}$$

(k here and below is in keV) with the constants determined using sources of ^{241}Am and ^{57}Co. The photopeak efficiency $\eta_{\rm ph}(k)$ of the HPGe detector was modeled by

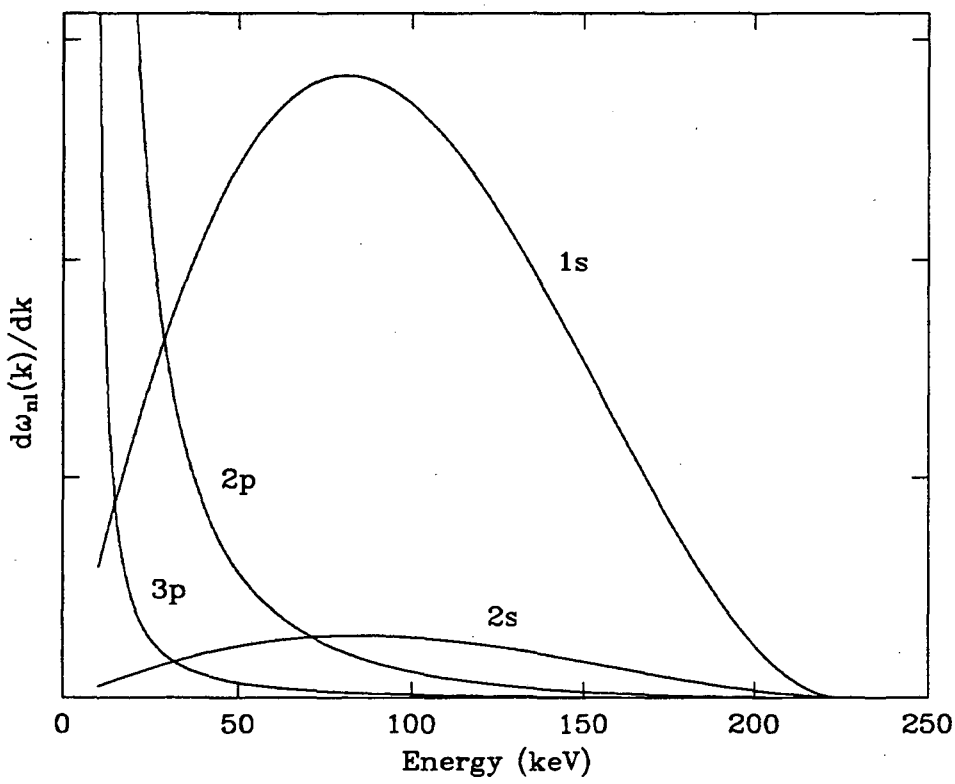

Figure 4.5: Theoretical ^{55}Fe IBEC spectra for $1s$-, $2s$-, $2p$-, and $3p$-capture.

a (simplified) standard functional form [113]:

$$\eta_{\rm ph}(k) = (k)^a \exp\left[b\left(\frac{k}{m_e}\right)^c\right]. \tag{4.18}$$

In the close geometry of this experiment $\eta_{\rm ph}$ is very sensitive to the position of the source. A source of ^{182}Ta, which has a number of γ lines in the range 50–300 keV, was measured at a distance of 10 inches from the detector, centered on the detector face. This measurement could not be done close to the detector because of prompt summing of coincident γ rays. The 10-inch photoefficiency function was used to relatively calibrate a set of sources with non-coincident γ rays at 10 inches. These sources were then measured against the face of the detector, in approximately the same geometry as the ^{55}Fe experiment. The constants in (4.18) were found by fitting these data:

$$\begin{aligned} a &= -0.954 \\ b &= -0.00759 \\ c &= -2.12\ . \end{aligned}$$

The relative photopeak efficiency functions at 0 and 10 inches are shown in Figure 4.6.

The photon response function for the data collected by ADC C was determined using sources of ^{241}Am, ^{57}Co, ^{139}Ce, and ^{203}Hg. For the purpose of generating the pseudodata, a complicated model of the response function was not needed. A very simple model was used, consisting of a gaussian photopeak and a flat tail corresponding to Compton scattered photons that escaped the detector and also escaped the NaI Veto. The variance σ^2 of the gaussian peak was measured to be

$$\sigma^2 = 0.208 + 4.73 \times 10^{-4} k \quad \text{keV}^2 \tag{4.19}$$

A prominant peak was seen in the test source spectra at the Compton backscatter energy, probably due to photons that backscattered from the detector cold finger

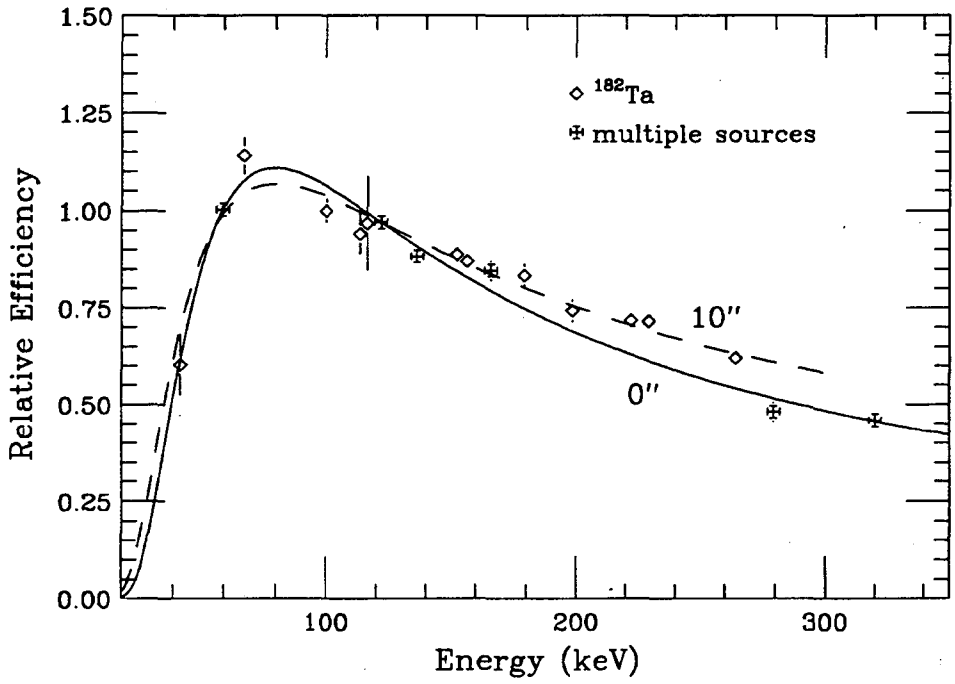

Figure 4.6: Relative photopeak efficiency functions $\eta_{\mathrm{ph}}(k)$ measured at 10 inches (^{182}Ta source) and 0 inches (multiple sources).

into the Ge crystal, so were not vetoed. This was modeled by a right-triangular peak with a full width of 30 keV. The tail height/photopeak height and backscatter-peak height/photopeak height ratios at each energy were extrapolated from the test-source measurements. The measured and model response functions for ^{57}Co (122 keV) and ^{139}Ce (166 keV) are shown in Figure 4.7.

The PUR circuit of the Ortec 572 amplifier operates as follows. When a second input pulse (above threshold) is received more than 300 ns but less than six times the set shaping time after an initial pulse, a PUR inhibit gate is generated which is used to gate off the ADC for that event. If the time separation is less than 300 ns this gate is not produced, and an event at approximately the sum energy of the two input pulses is recorded. This creates a residual pileup spectrum. The PUR efficiency was measured by collecting a time-to-amplitude converter (TAC) spectrum of successive pulses using the ^{55}Fe source and the HPGe detector, taken in coincidence with the 572 PUR inhibit signal. The result is shown in figure 4.8. A PUR inhibit gate is always present when the signals are greater than 600 ns apart and never present when the signals are less than about 300 ns apart. From 300–600 ns the probability for getting a PUR inhibit gate is approximately linear. Because a residual pileup pulse is recorded at nearly the sum energy of the two simultaneous pulses, its spectrum can be approximated by a simple convolution:

$$\frac{dN(k)_{pileup}}{dk} = I_{pu} R \int_{k_{min}}^{k_{max}} dk' \frac{dN(k-k')}{d(k)} \cdot \frac{dN(k')}{dk'} \tag{4.20}$$

where R is the counting rate ($\approx$ 8000 s^{-1}) and I_{pu} is the integral over Δt of the probability for not generating a pileup reject gate. Figure 4.8 shows $I_{pu} \approx$ 450ns. The contribution to the pileup spectrum from signals below the PUR threshold (27 keV) was neglected. The photopeak efficiency falls off rapidly below 50 keV, so this contribution to the pileup in the energy range of interest (180–240 keV) is expected to be very small.

When the pseudodata spectrum was generated incorporating all of the above elements a slight linear divergence from the experimental ^{55}Fe spectrum of ADC

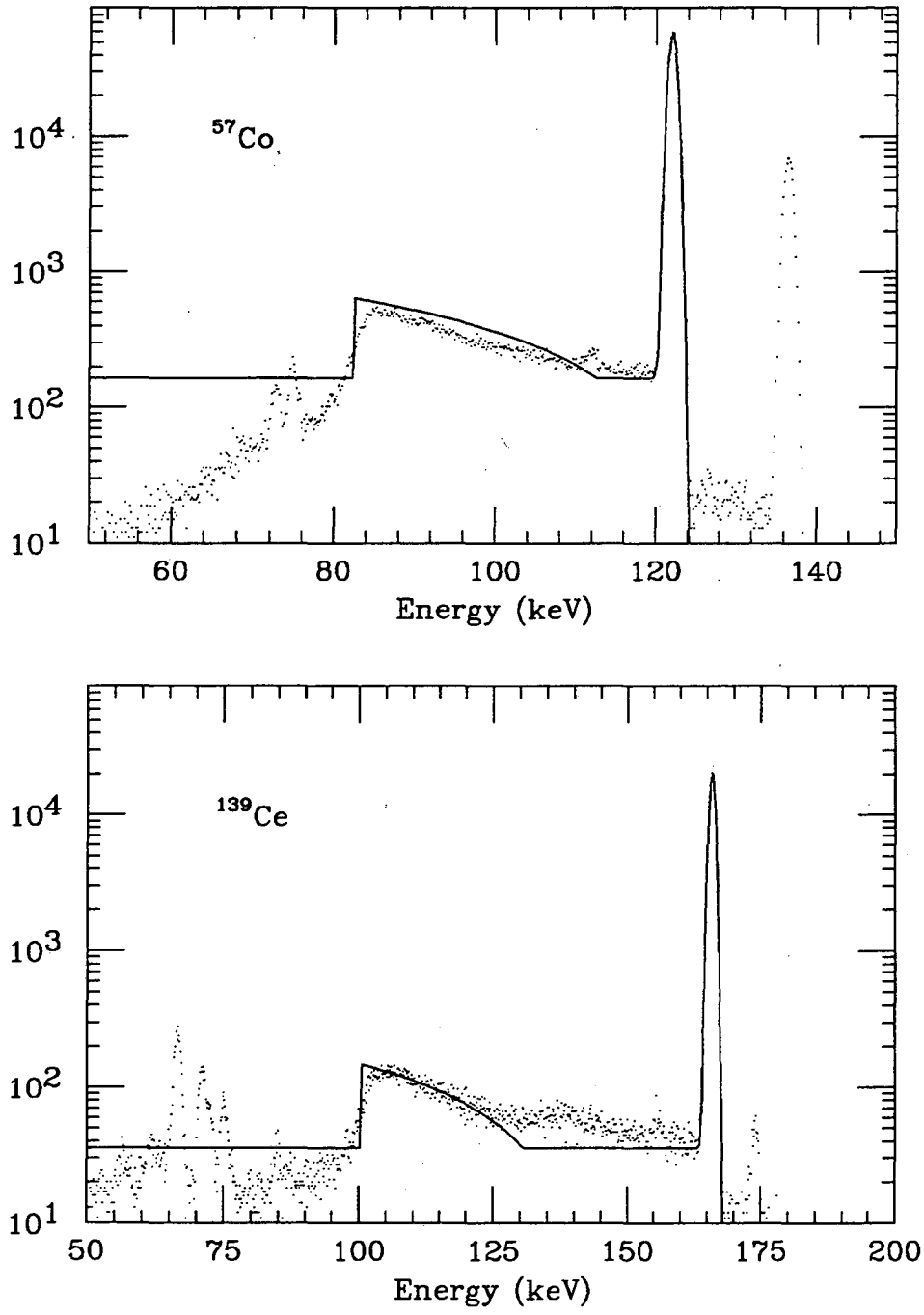

Figure 4.7: Measured and model photon response function (with PUR and NaI veto) for ^{57}Co (top) and ^{139}Ce (bottom).

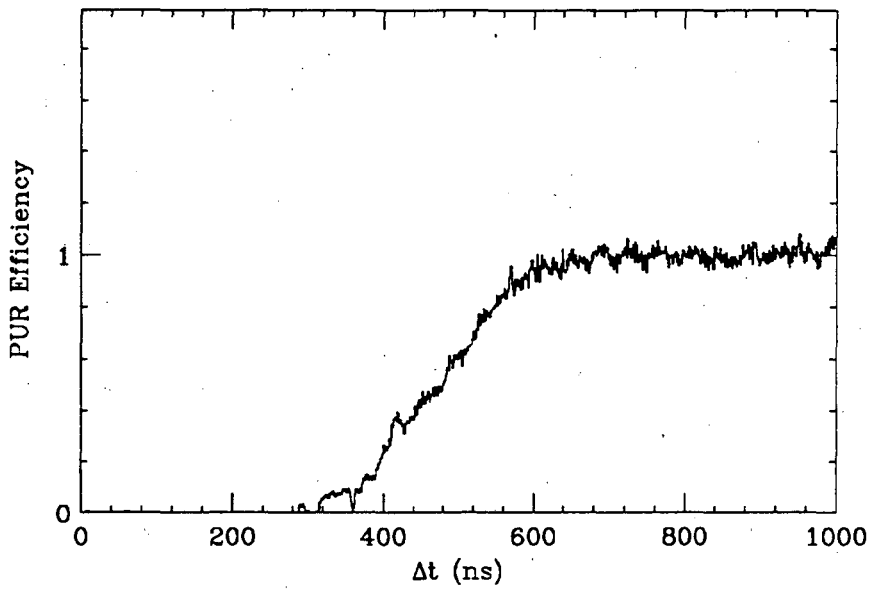

Figure 4.8: PUR efficiency measurement: TAC spectrum of successive ^{55}Fe pulses in coincidence with 572 amplifier PUR inhibit.

C was evident. To correct this, a linear correction factor equal to $[1 + 8.0 \times 10^{-4}\text{keV}^{-1}(q_{nl} - k)]$ was included in the pseudodata spectrum. The divergence was probably due to the uncertainty in measuring the photopeak efficiency in such close geometry. This correction was included to make the pseudodata as realistic as possible, although it clearly will not affect a local kink search in the pseudodata spectrum. Figure 4.9 shows the complete pseudodata spectrum containing 1.17×10^7 counts/keV at 208 keV, compared to the background- and impurity-subtracted ^{55}Fe spectrum C. The ratio of these spectra is shown in Figure 4.10, both with and without the shape correction, and the agreement is good over several orders of magnitude in intensity, and excellent in the region of interest. X rays from Pb flourescence, the ^{55}Fe line at 126 keV, and the ^{123}Te impurity line at 159 keV can also be seen in this figure.

Figure 4.11 shows the second derivative of the pseudodata spectrum prior to adding statistical dispersion. There are two neutrino kinks: one at 208 keV from the 1s spectrum, and another at 214 keV due to the 2s, 2p, and 3p spectra which

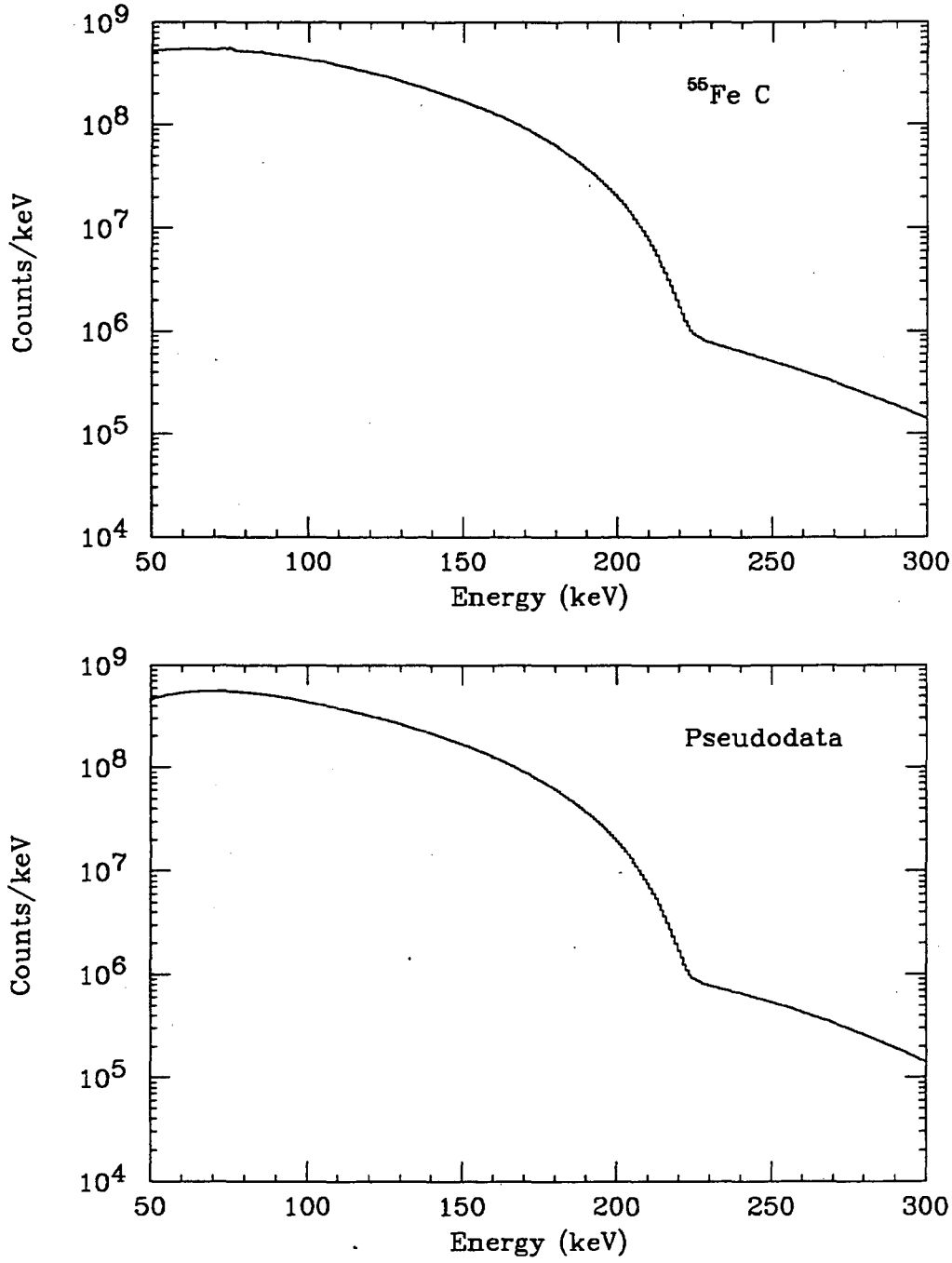

Figure 4.9: ^{55}Fe spectrum C with background and impurities subtracted (top) and the corresponding pseudodata spectrum (bottom).

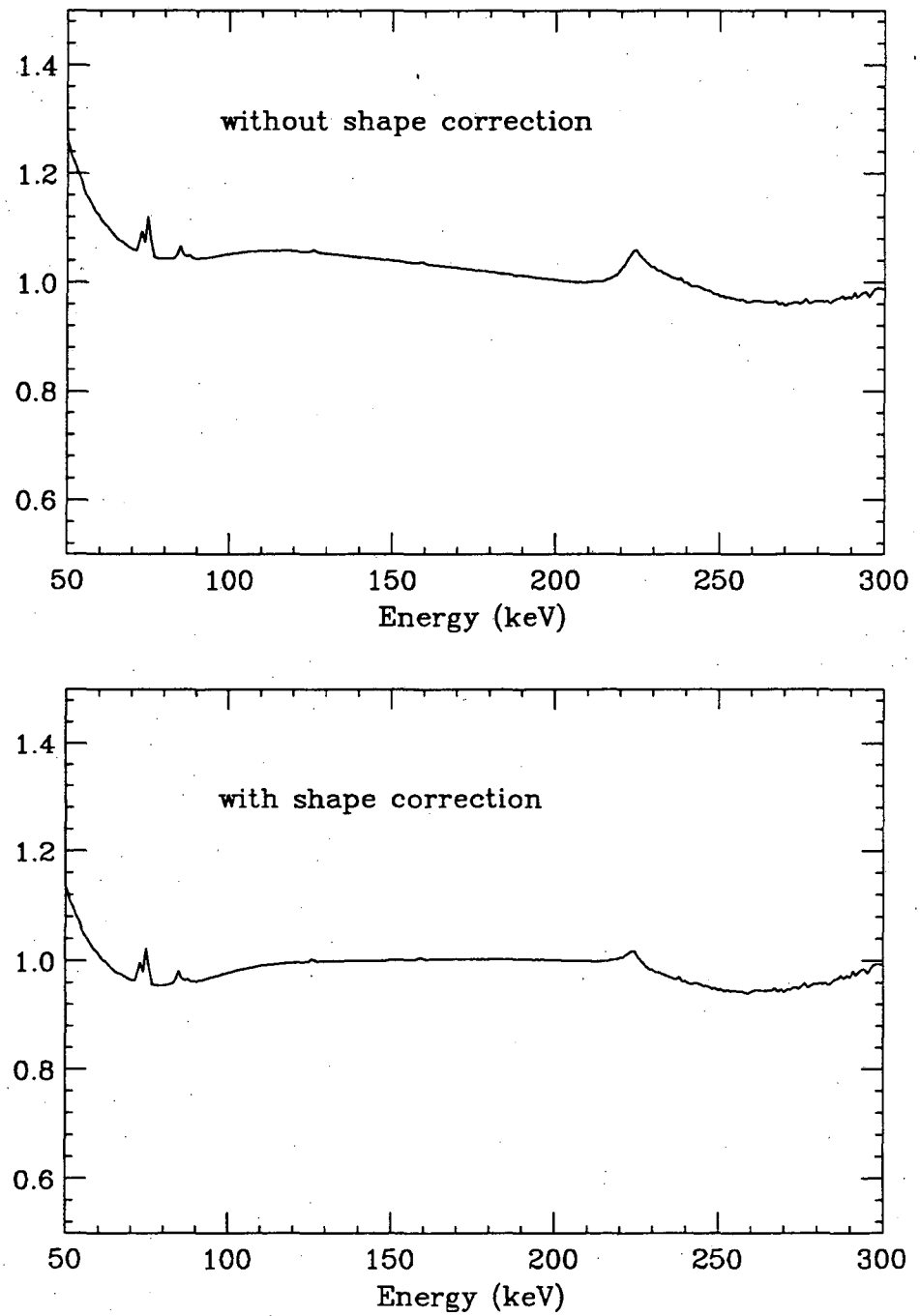

Figure 4.10: Ratio of ^{55}Fe spectrum C to the pseudodata without a shape correction (top), and with a linear shape correction $[1 + 8.0 \times 10^{-4}\text{keV}^{-1}(q_{nl} - k)]$ to the pseudodata (bottom).

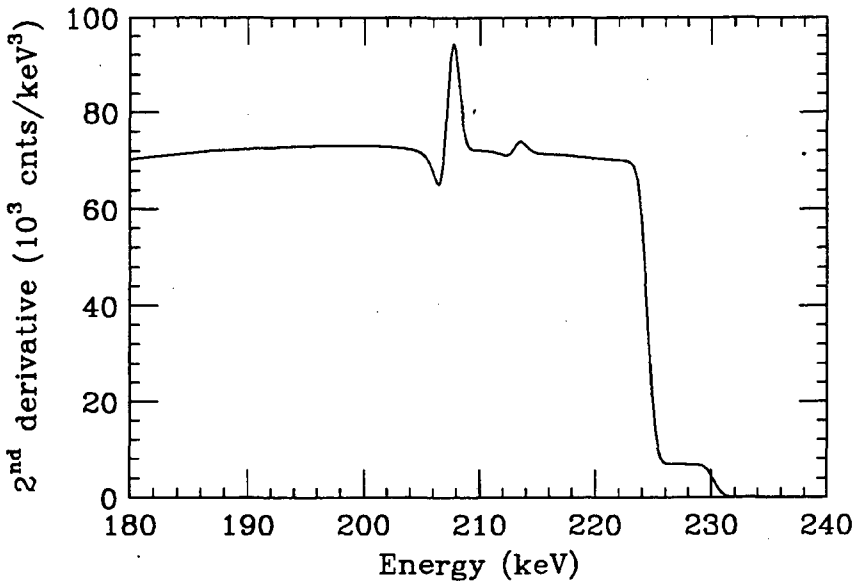

Figure 4.11: Second derivative of pseudodata spectrum without statistical dispersion. Neutrino kinks are seen at 208 keV (1s spectrum) and 214 keV (2s,2p,3p spectra).

have a 6-keV higher endpoint. Second derivatives of pseudodata spectra, with and without a 1% 17 keV neutrino and including Poisson statistics, are shown in figure 4.12. The data were compressed into 20 channel bins (2.6 keV/bin) to reduce the dispersion in the points. A peak due to the neutrino kink is evident at 208 keV, about 8 standard deviations above the baseline. The absolute height of the peak is smaller here than in figure 4.11 due to the data compression.

A 20-keV-wide region of the pseudodata (200–220 keV, 154 points) containing a 1% 17 keV neutrino was fit to the polynomial function (4.2). For each trial $\tan^2\theta$ and m_2 were fixed and a_0–a_3 were allowed to vary for the best fit. The χ^2 contour plot is shown in figure 4.13 (top). The χ^2 minimum corresponds to a mass of 16.9 ± 0.2 keV and a mixing of $0.74 \pm 0.08\%$. The mixing comes out too low because at the kink position (208 keV) 74% of the total spectrum is from 1s capture, 13% from $2s$ capture, 1% from $2p$ and $3p$ capture, and 12% from pileup. Therefore a 17 keV neutrino mixture of 1% in the $1s$ spectrum becomes 0.74% of the total.

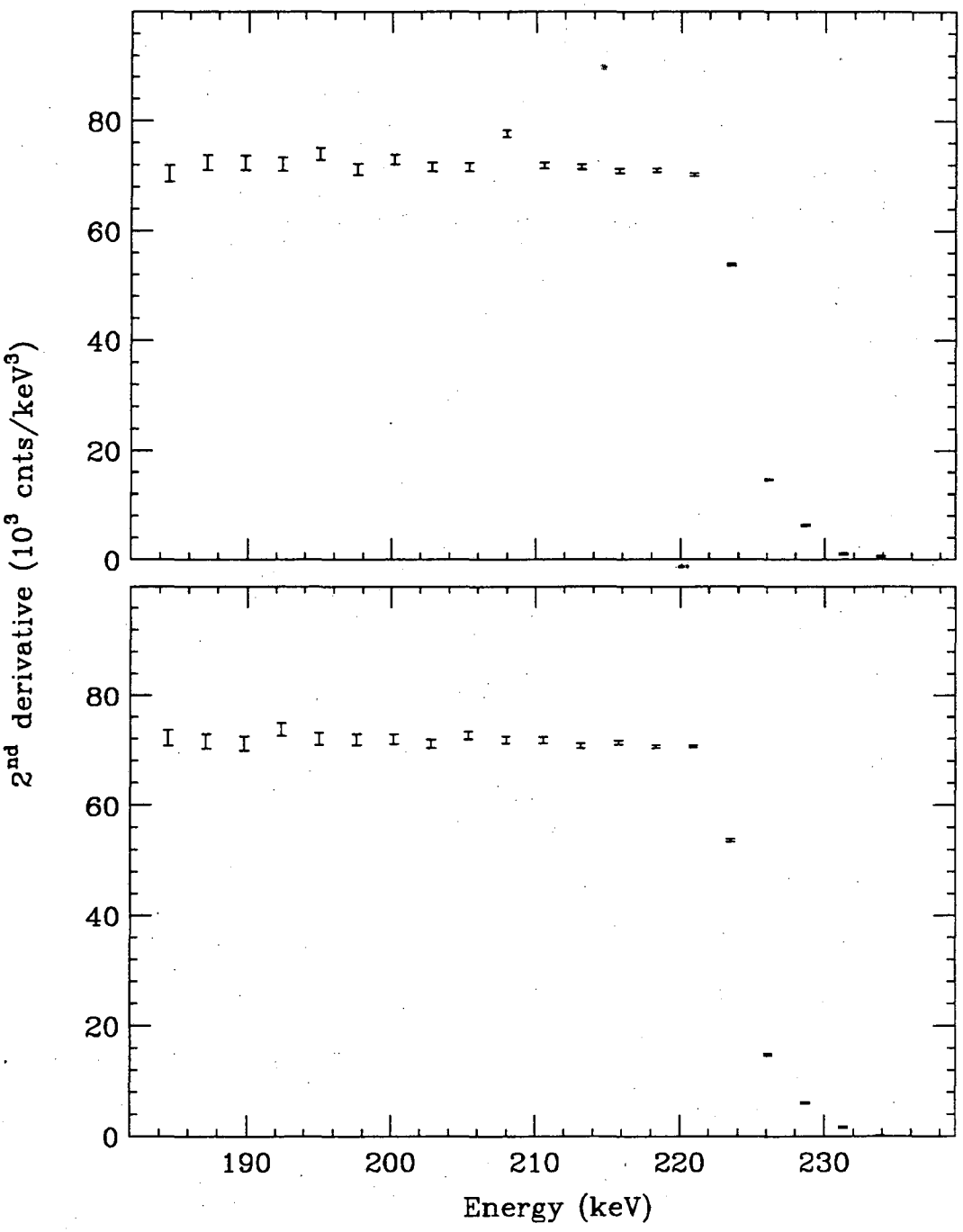

Figure 4.12: Second derivatives of pseudodata spectra containing a 1% 17 keV neutrino (top), and no massive neutrino (bottom).

A correction for this will be needed in the actual data analysis as well. The fit at $\tan^2\theta = 0$ has $\Delta\chi^2 = 55.9$ (7.5σ) from the minimum. The χ^2 contour plot for similar polynomial fits to the pseudodata containing no massive neutrino is shown in figure 4.13 (bottom). Figure 4.14 shows the polynomial fit and data/fit for the pseudodata containing a 1% 17 keV neutrino and fit with $m_2 = 0$, $\tan^2\theta = 0$.

Finally, to verify that the polynomial fit analysis will be insensitive to smooth distortions in the data, additional pseudodata spectra were generated containing quadratic distortions of the form:

$$N(k)_{dis} = N(k)\left[1 + c_1(q_{nl} - k) + c_2(q_{nl} - k)^2\right] \tag{4.21}$$

with c_1 and c_2 chosen arbitrarily. For $-10^{-2} \leq c_1 \leq 10^{-2}$ keV^{-1} and $-10^{-4} \leq c_2 \leq 10^{-4}$ keV^{-2} the presence or absence of a neutrino kink in the spectrum was always correctly found. Figures 4.15a,b show some examples.

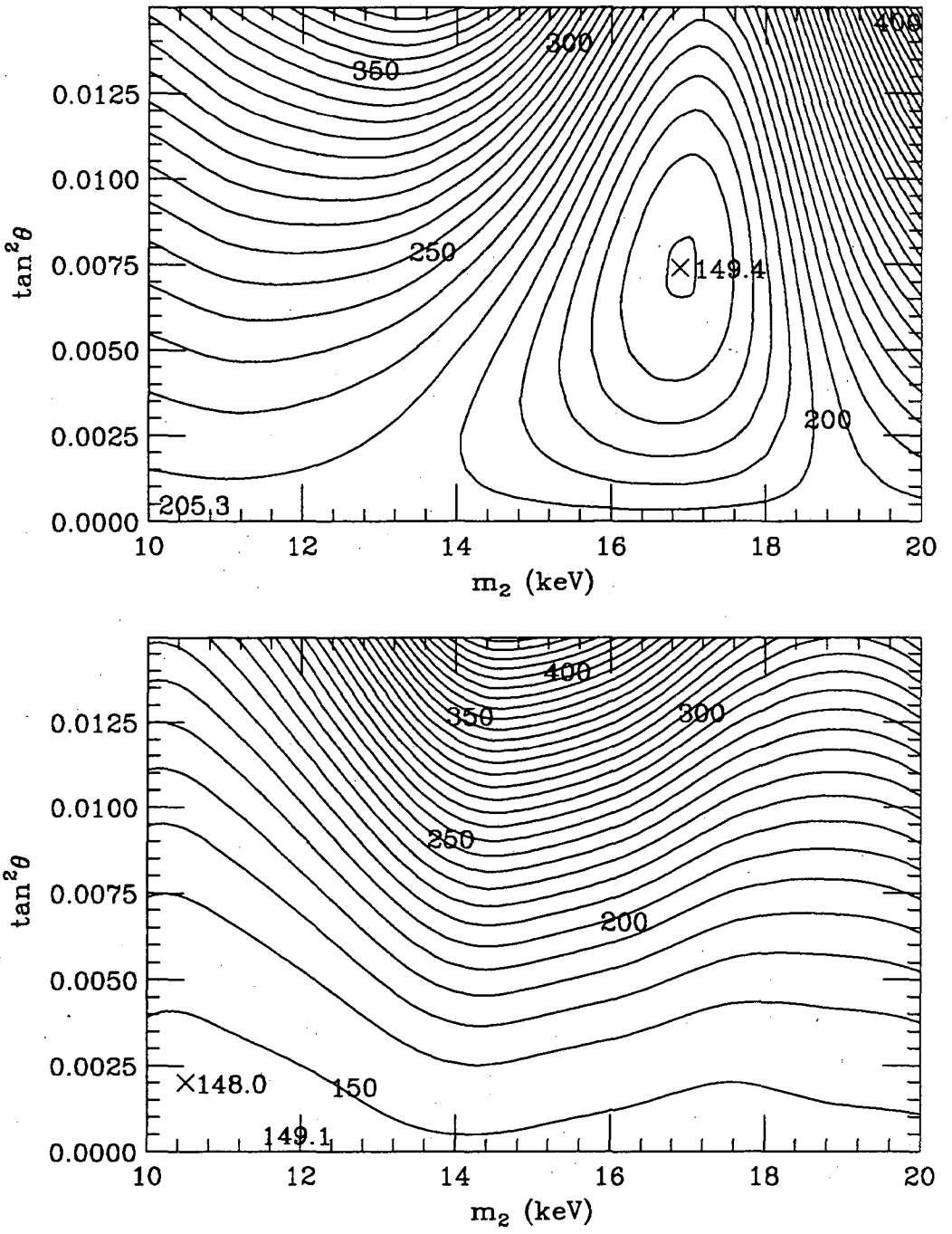

Figure 4.13: χ^2 contour plot for polynomial fits to the pseudodata containing a 1% 17 keV neutrino, in the region 200–220 keV, 154 points (top); and a similar plot for fits to the pseudodata containing no massive neutrino (bottom). The absolute minima are marked by an X.

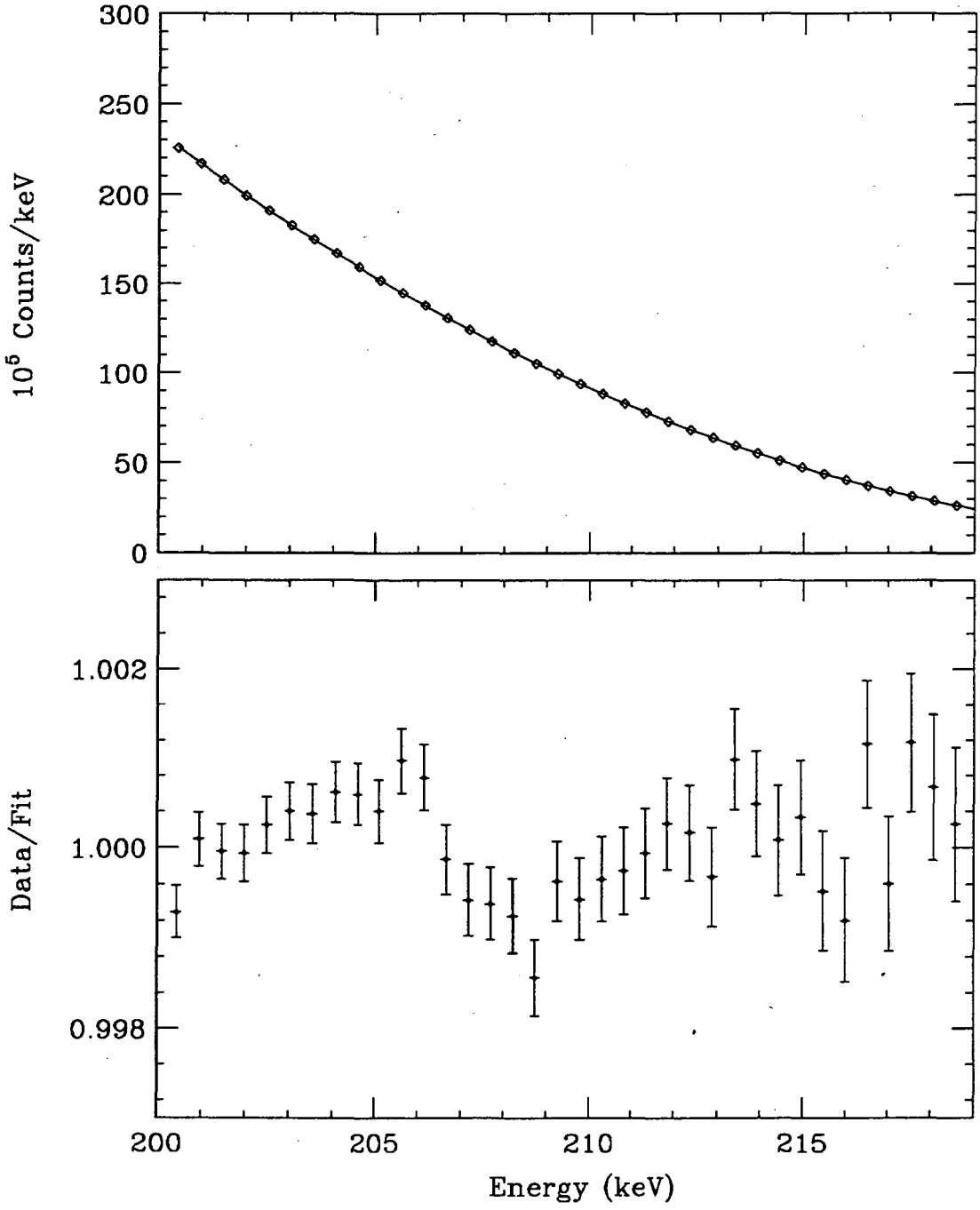

Figure 4.14: Polynomial fit (top) and data/fit (bottom) of the pseudodata containing a 1% 17 keV neutrino; fit with m_2=0, $\tan^2\theta = 0$. The data are compressed (4 channels/bin) for clarity.

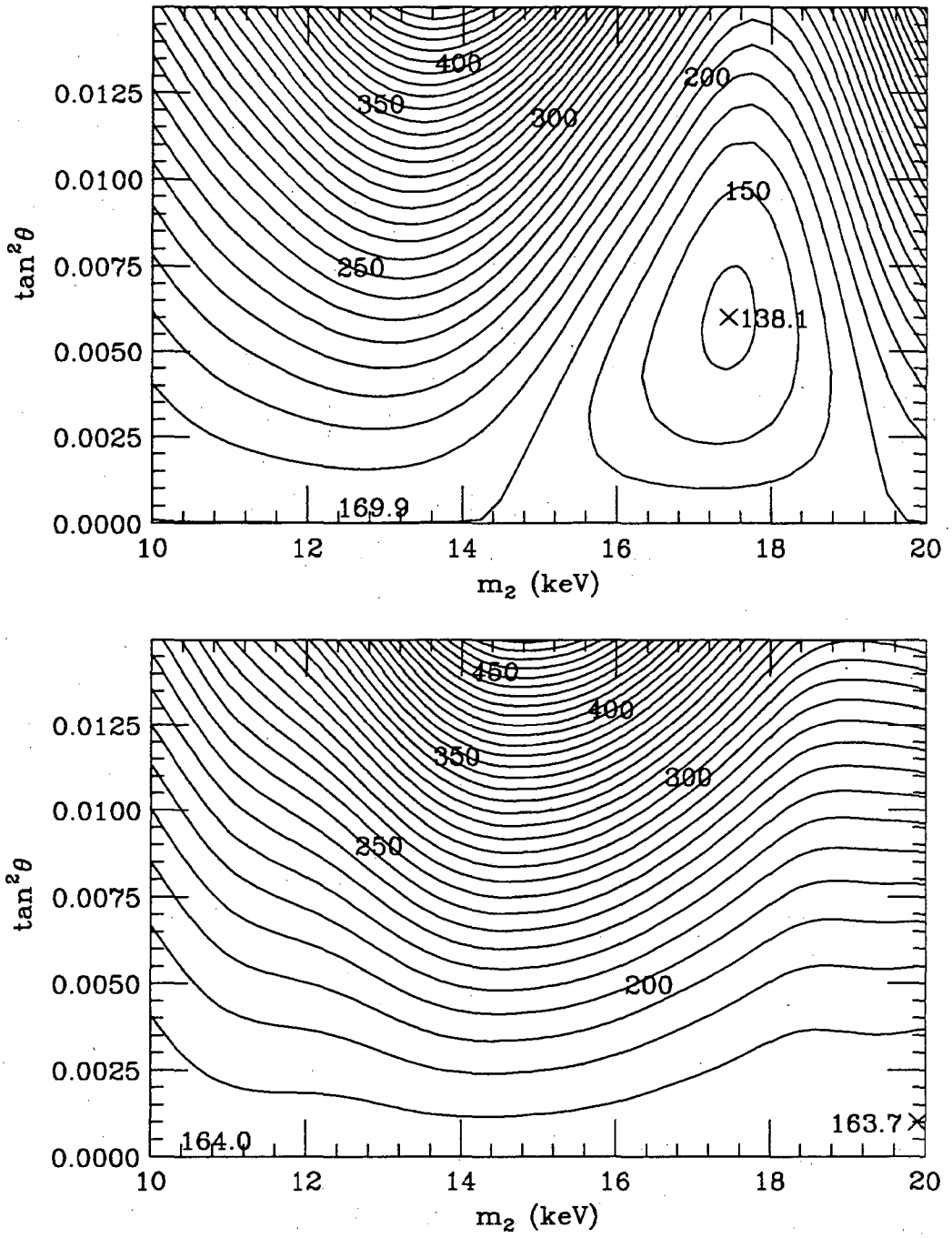

Figure 4.15a: Polynomial fits to pseudodata including a distortion factor equal to $[1 - 3.0 \times 10^{-3}\text{keV}^{-1}(q_{nl} - k) + 5.0 \times 10^{-5}\text{keV}^{-2}(q_{nl} - k)^2]$; with a 1% 17 keV neutrino (top), and no massive neutrino (bottom).

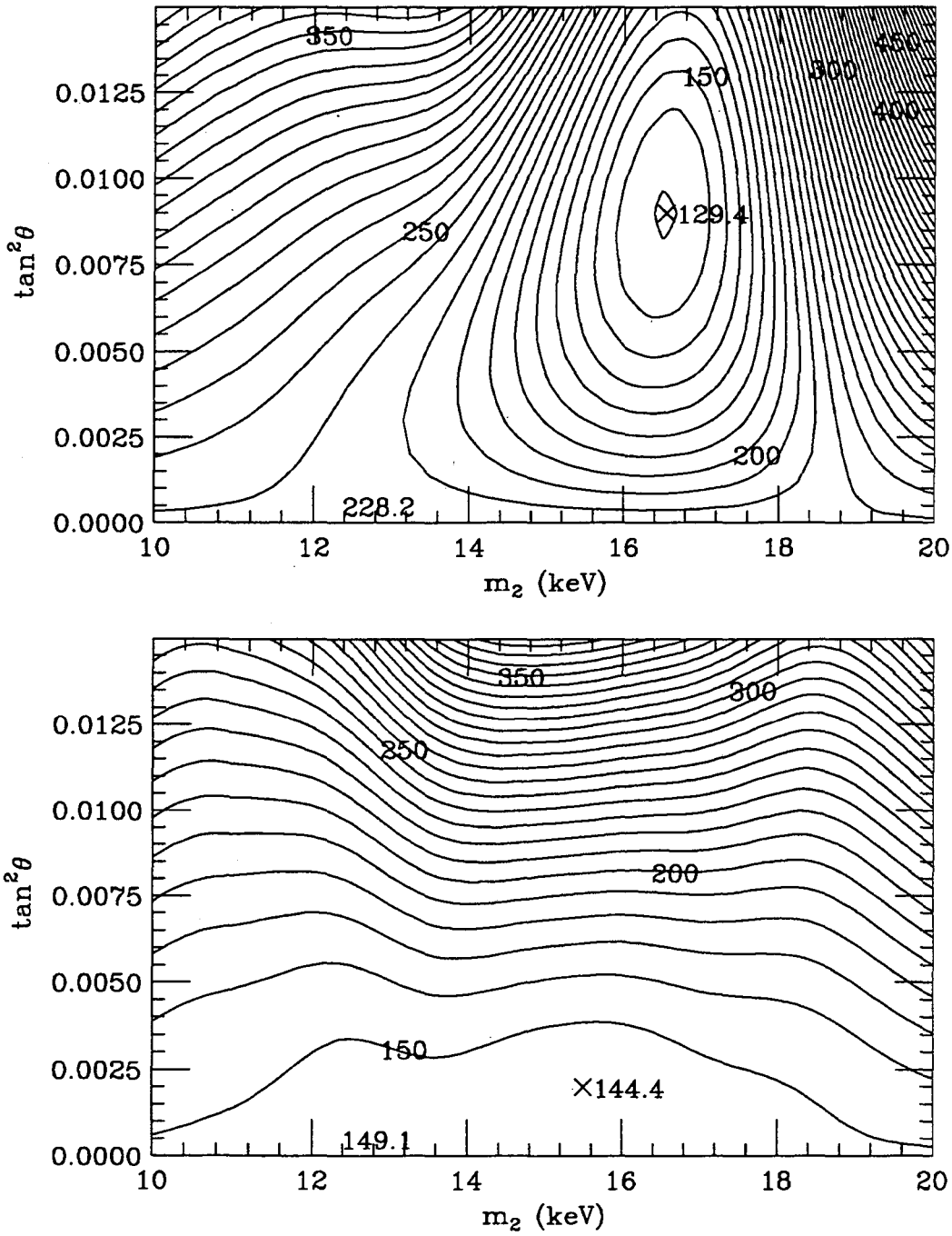

Figure 4.15b: Polynomial fits to pseudodata including a distortion factor equal to $[1 + 5.0 \times 10^{-3}\text{keV}^{-1}(q_{nl} - k) - 1.0 \times 10^{-5}\text{keV}^{-2}(q_{nl} - k)^2]$; with a 1% 17 keV neutrino (top), and no massive neutrino (bottom).

4.4 Data Analysis

The vetoed ^{55}Fe data (spectrum C) were analyzed in the same way as the pseudodata. Figure 4.16 (top) shows the second derivative of the raw spectrum. The dominant feature is the ^{59}Fe line at 192 keV, and it illustrates the power of the second derivative technique for magnifying small structures; this line can barely be seen in the raw data. Figure 4.16 (bottom) shows the second derivative of the same spectrum after background and impurity subtraction. There is no sign of a neutrino kink at 208 keV or anywhere else. As with the pseudodata, these data have been compressed into twenty-channel bins (2.6 keV/bin) to reduce the statistical dispersion and maximize sensitivity to the kink. There is a concern that if the neutrino mass were not exactly 17 keV, but rather 16 or 18 keV, this data compression would tend to wash out the peak in the second derivative; it would be split between two bins. To verify that this did not happen, twenty versions of the binned spectrum were produced, each with twenty channels per bin but with different channel offsets. Representative samples can be seen in Appendix B. None of these spectra show evidence for a massive neutrino kink.

Three overlapping regions of ^{55}Fe spectrum C were fit to the polynomial function (4.2) to test three ranges of neutrino mass: 195–215 keV with m_2=15–25 keV (154 points); 200–220 keV with m_2=10–20 keV (154 points), and 205–224 keV with m_2=5–15 keV (147 points). Figure 4.17 shows the χ^2 contours for the fits of the 200–220 keV region. The best fit is m_2=10.75 keV and $\tan^2\theta$=0.002, with χ^2=164.3 (χ^2_ν=1.10), which is statistically consistent with no massive neutrino (χ^2=166.2). A 0.8% 17.0 keV neutrino (the result of Hime and Jelley [56]) should give $\tan^2\theta$=0.006 in this analysis, after correcting for higher-shell capture and pileup (see Section 4.3). This yields χ^2=209, a difference of 45 units (6.7σ) from the minimum. The χ^2 contours for the other two regions are shown in figure 4.18. There is no evidence for a massive neutrino in either region. Figure 4.19 shows the polynomial fit and data/fit with no massive neutrino. Figure 4.20 shows a

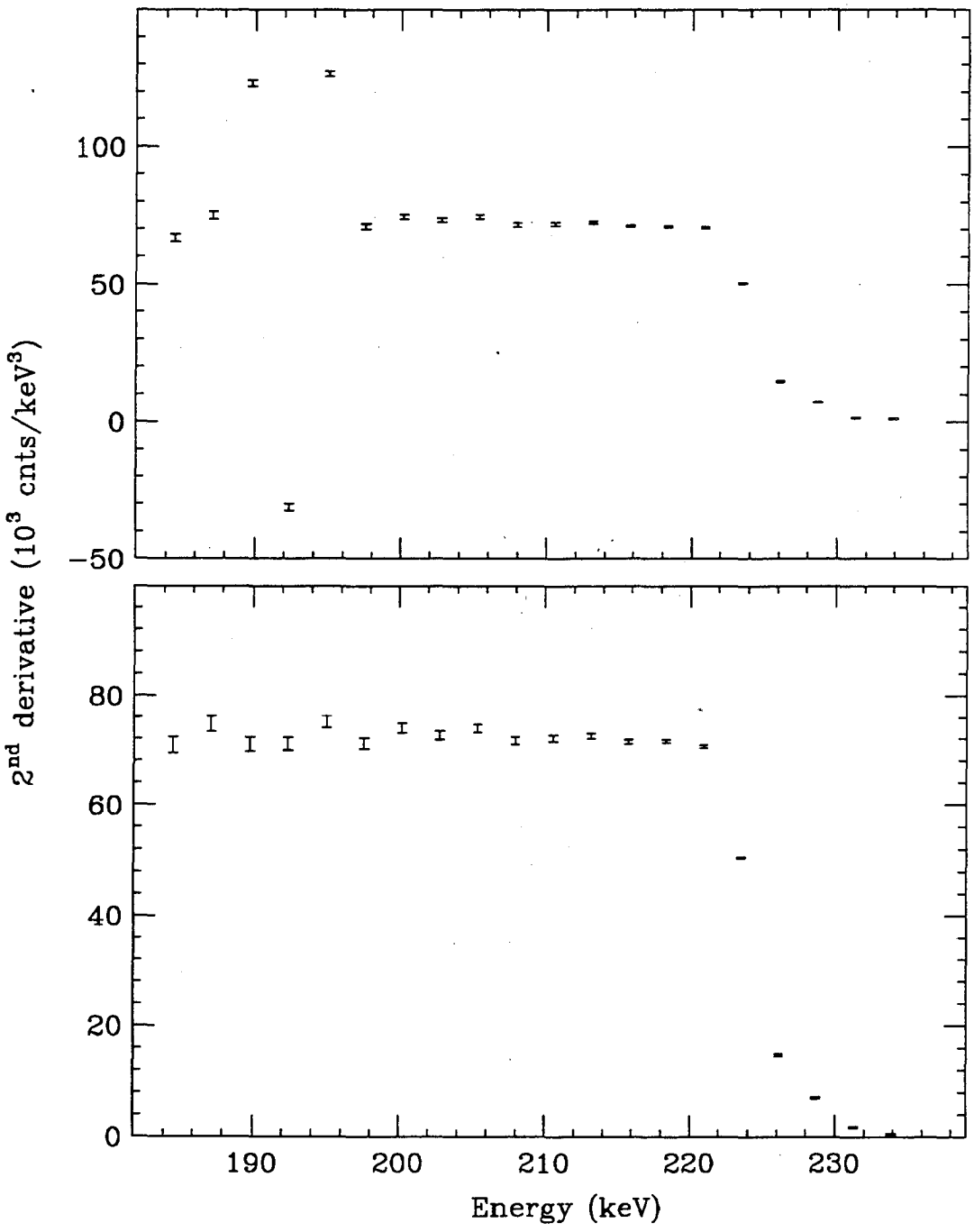

Figure 4.16: Second derivatives of ^{55}Fe spectrum C raw data (top) revealing the ^{59}Fe line at 192 keV, and the same data after background and impurity subtraction (bottom).

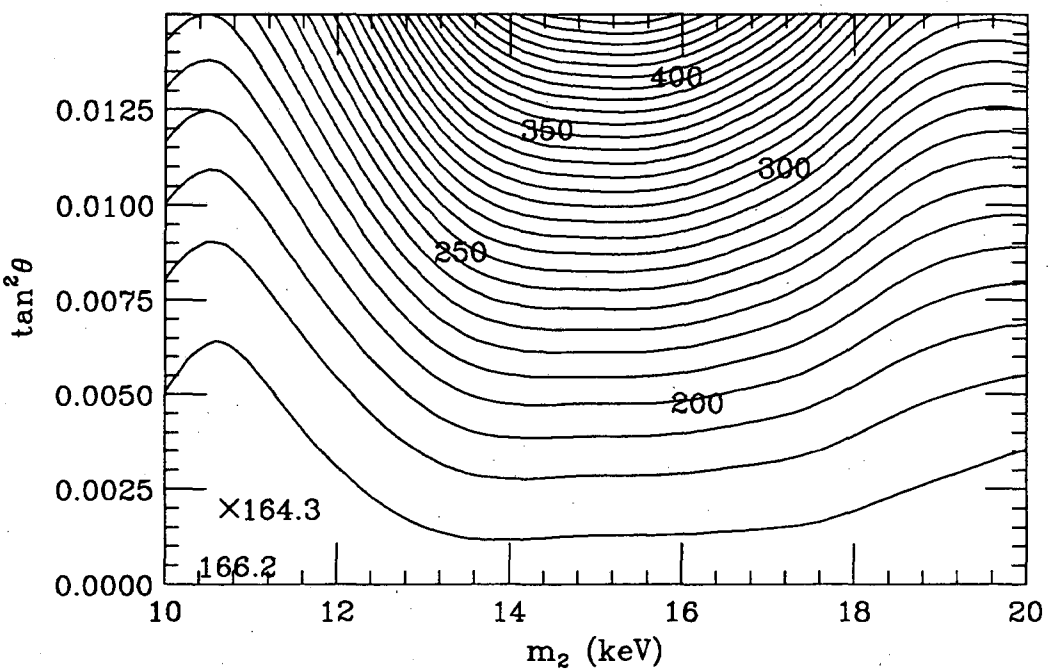

Figure 4.17: χ^2 contour plot for polynomial fits to ^{55}Fe spectrum C with 130-eV-wide bins in the region 200–220 keV (154 points). The absolute minimum is marked with an X.

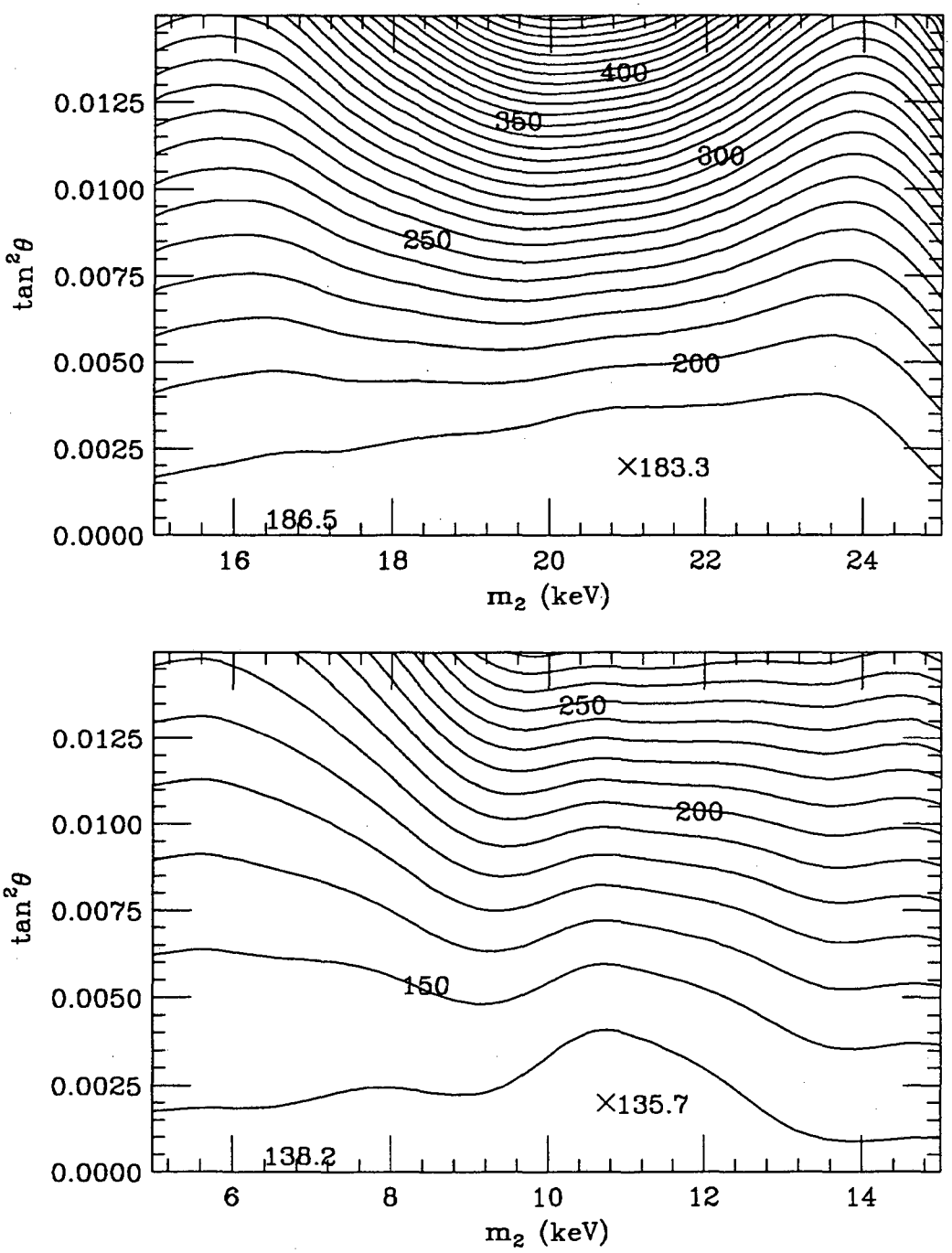

Figure 4.18: χ^2 contours for polynomial fits to ^{55}Fe spectrum C with 130-eV-wide bins in the regions 195–215 keV (154 points) (top), and 205–224 keV (147 points) (bottom).

similar plot for a fit including a 17 keV neutrino with $\tan^2\theta$=0.006.

The data of ^{55}Fe spectrum A (no vetos) and B (pileup rejection only) were analyzed in a similar way. Figure 4.21 shows the second derivatives of these spectra after background and impurity subtraction. The χ^2 contours for the polynomial fits are shown in figures 4.22-4.25. They support the results of spectrum C. There is no evidence for a massive neutrino in either spectrum.

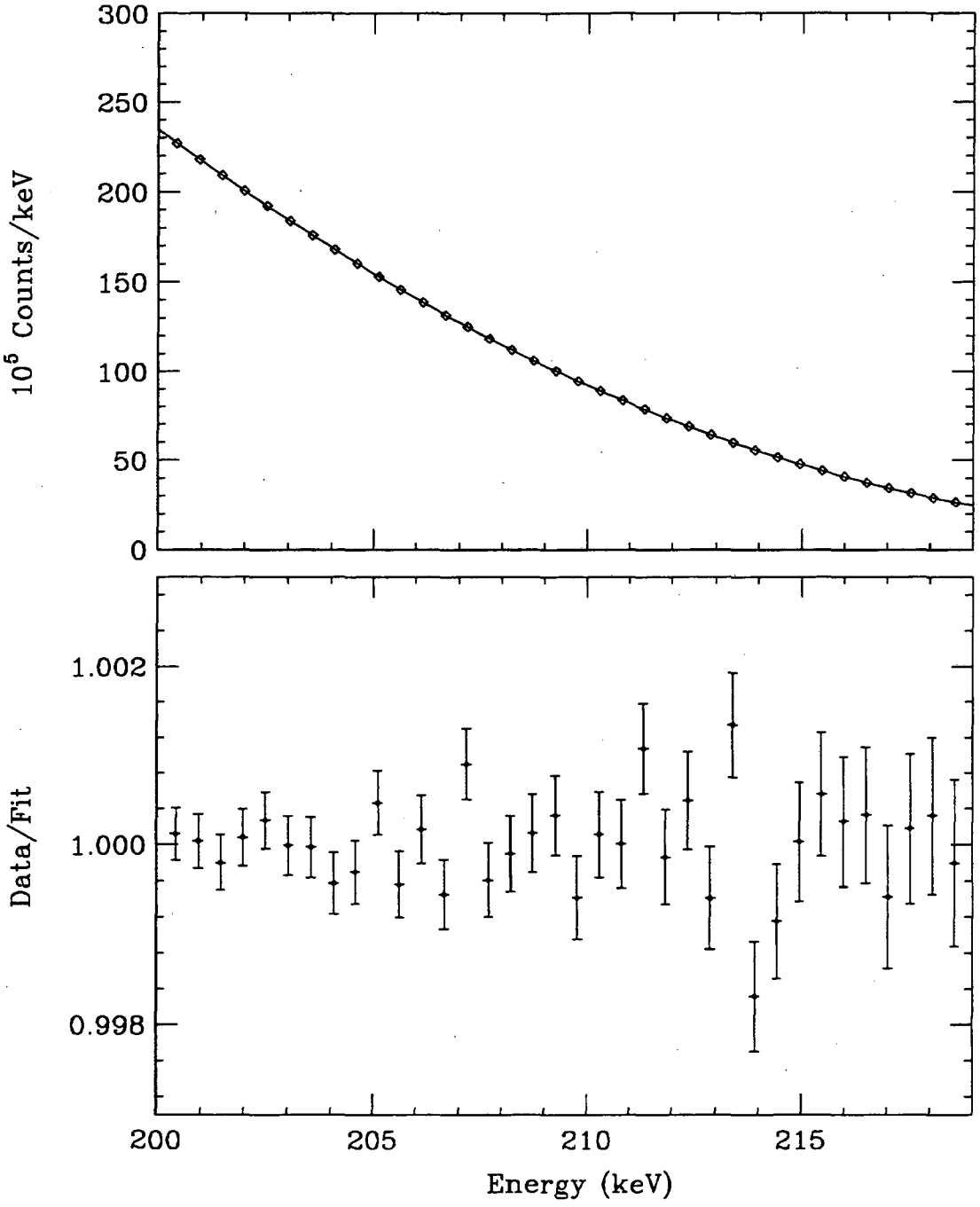

Figure 4.19: Polynomial fit (top) with no massive neutrino and data/fit (bottom) of ^{55}Fe spectrum C. The data are compressed (4 channels/bin) for clarity.

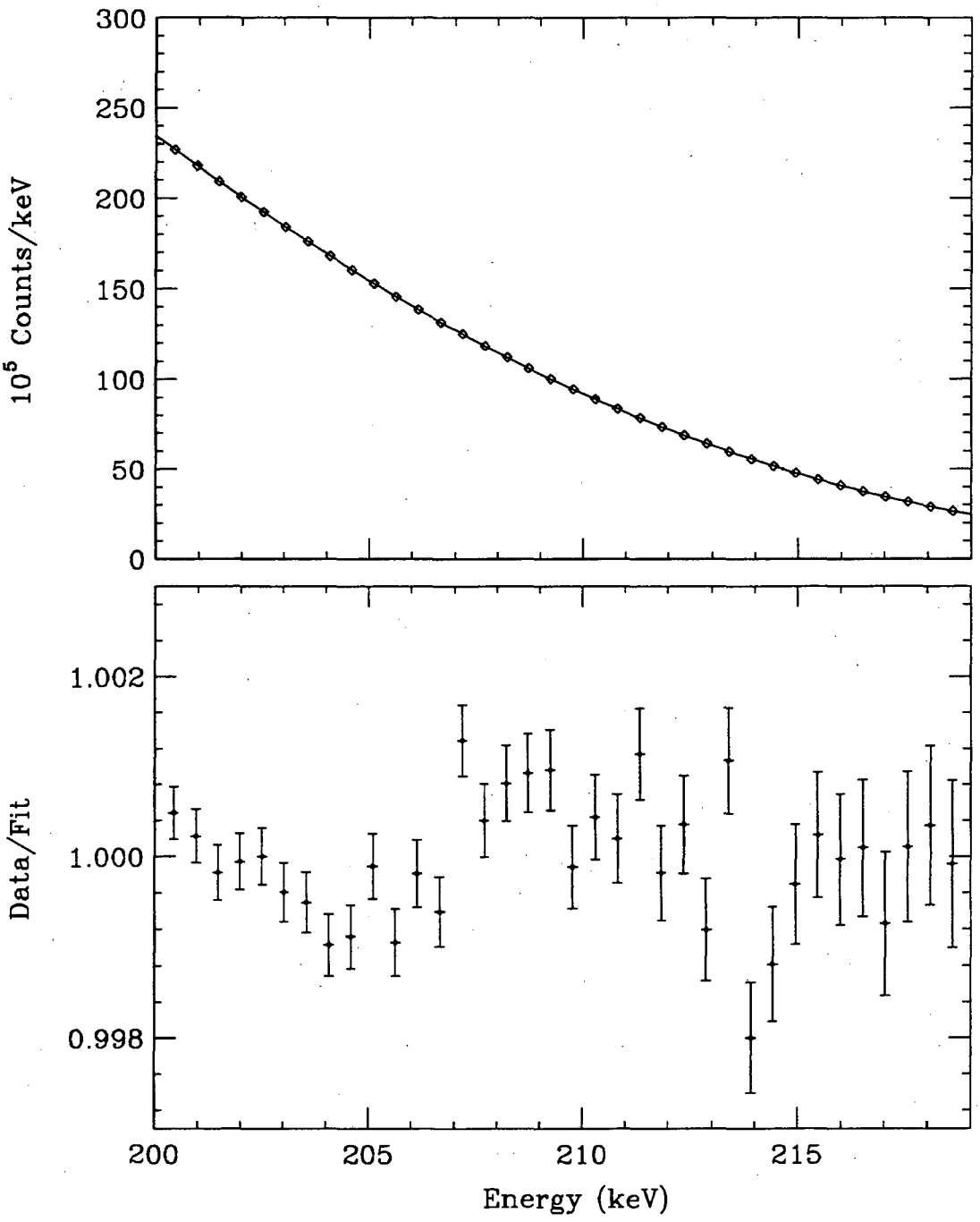

Figure 4.20: Polynomial fit (top) with m_2=17 keV, $\tan^2\theta$=0.006 and data/fit (bottom) of ^{55}Fe spectrum C. This value of the mixing is equivalent (after corrections) to the Oxford ^{35}S result [56].

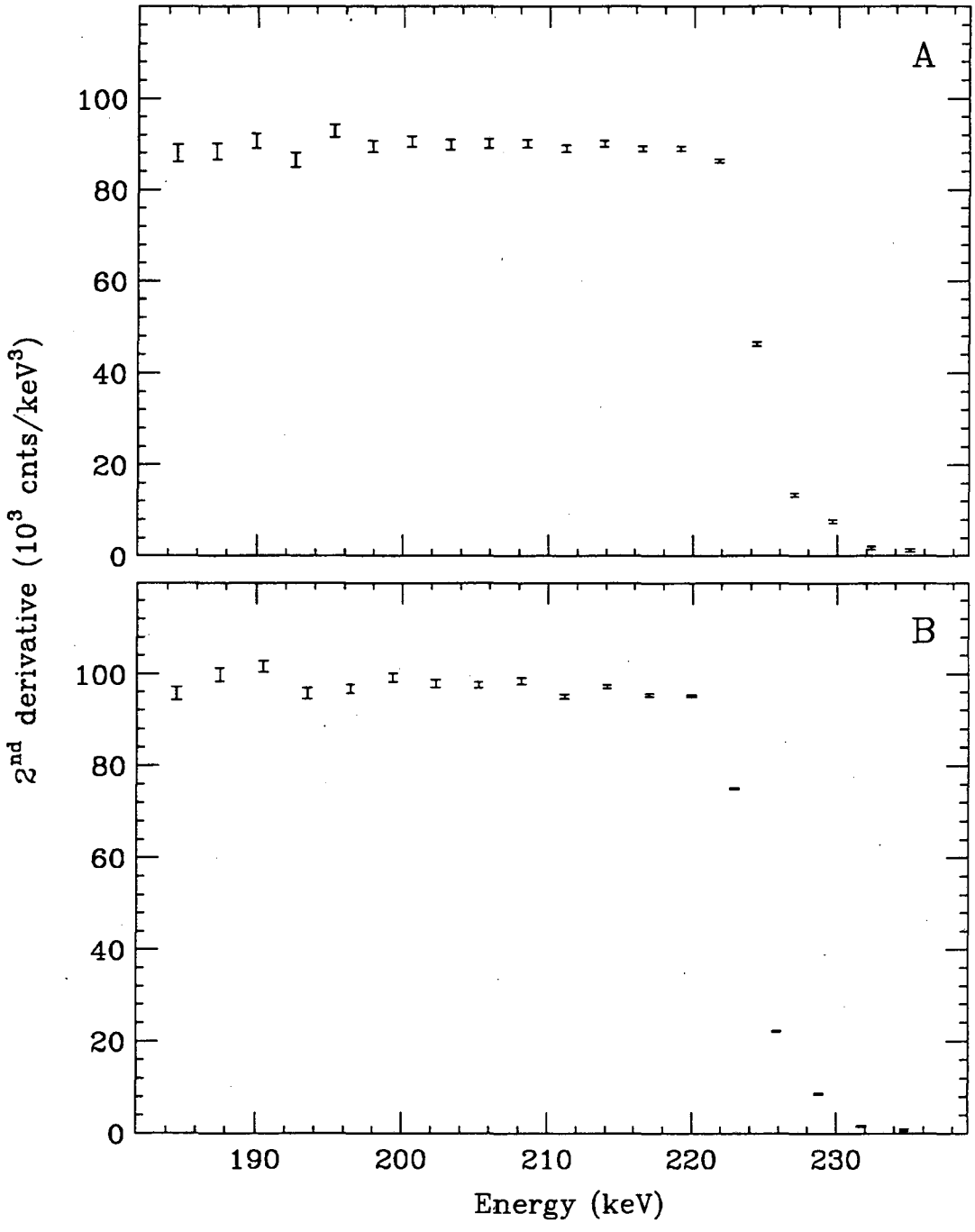

Figure 4.21: Second derivatives of ^{55}Fe spectrum A (no vetos) (top), and B (PUR only) (bottom).

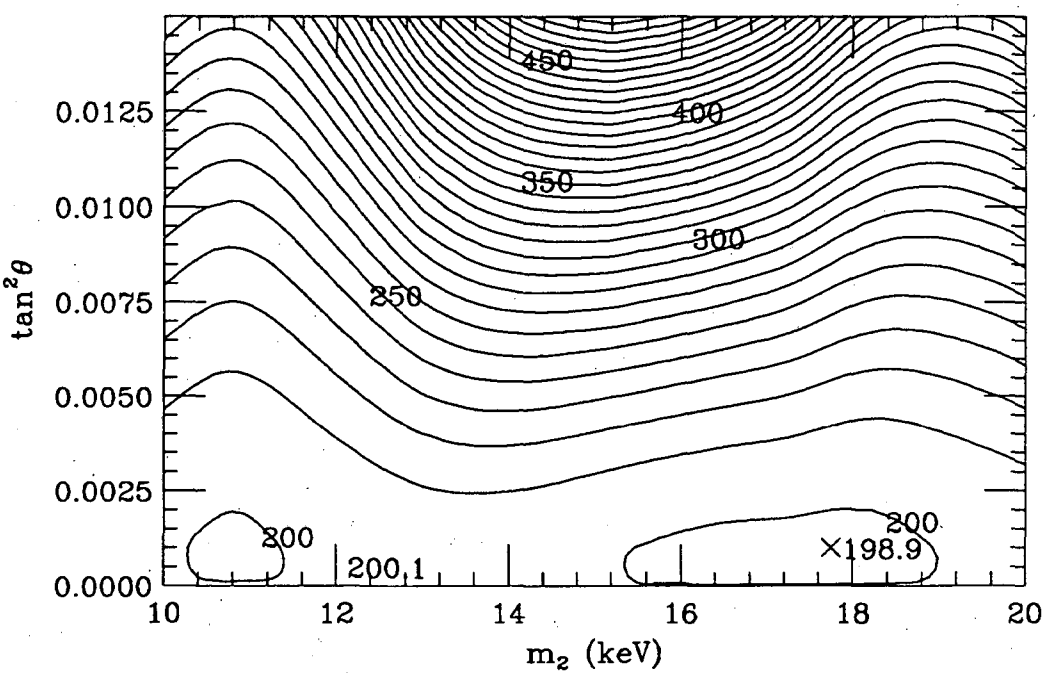

Figure 4.22: χ^2 contour plot for polynomial fits to ^{55}Fe spectrum A with 133-eV-wide bins in the region 200–220 keV (151 points).

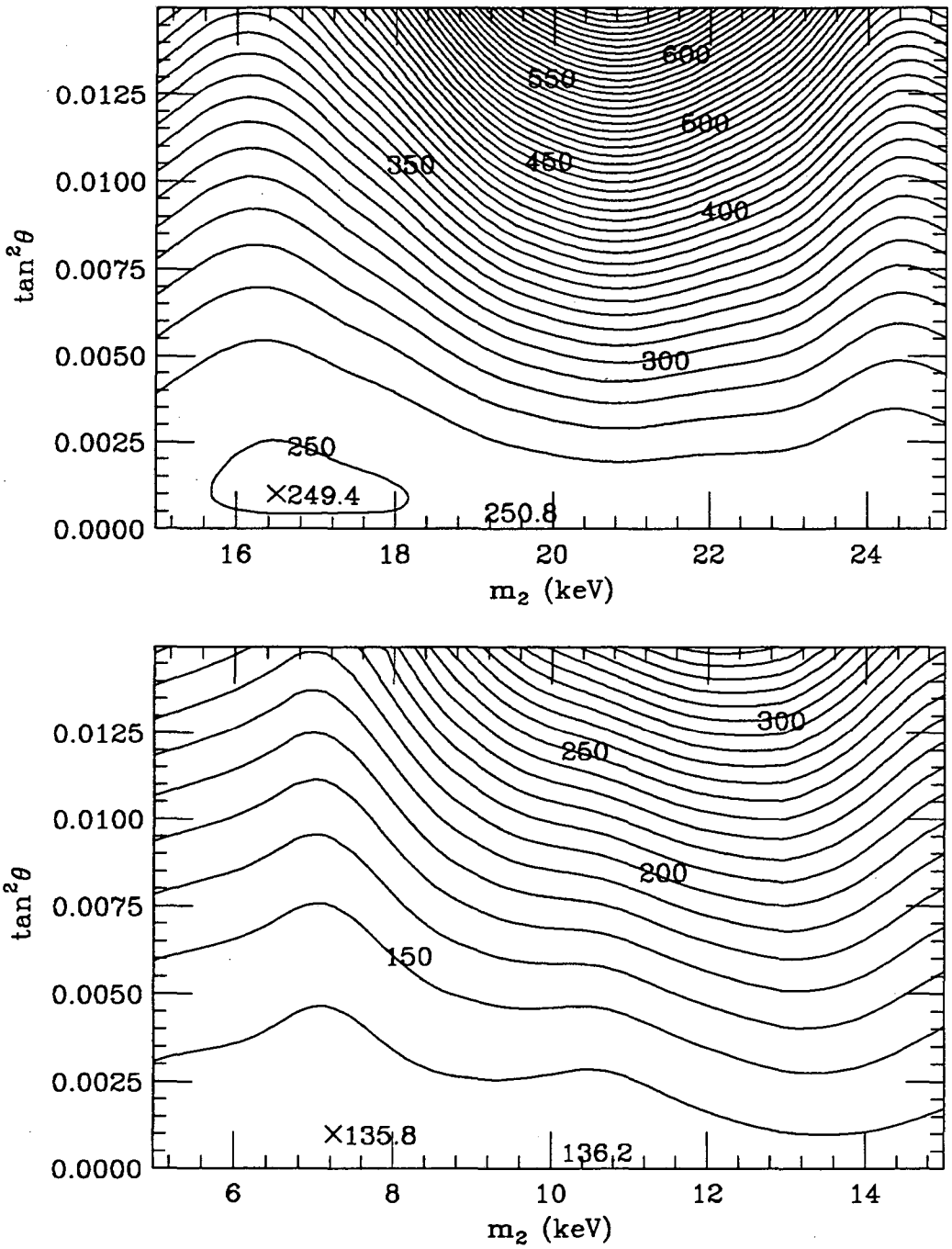

Figure 4.23: χ^2 contours for polynomial fits to ^{55}Fe spectrum A with 133-eV-wide bins in the regions 195–215 keV (151 points) (top), and 205–224 keV (143 points) (bottom).

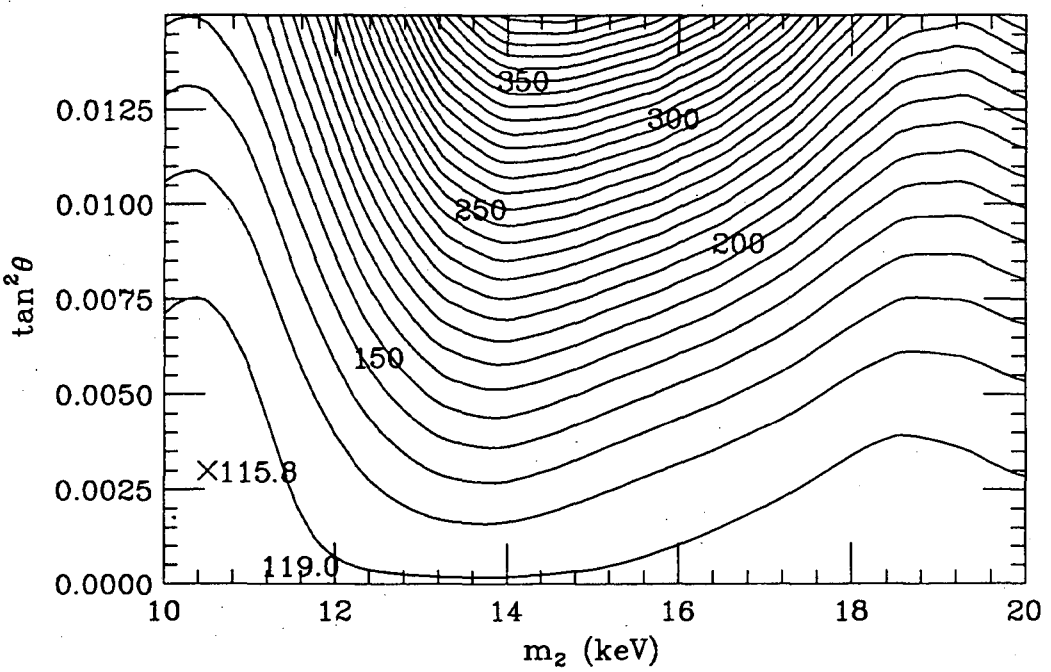

Figure 4.24: χ^2 contour plot for polynomial fits to ^{55}Fe spectrum B with 147-eV-wide bins in the region 200–220 keV (136 points).

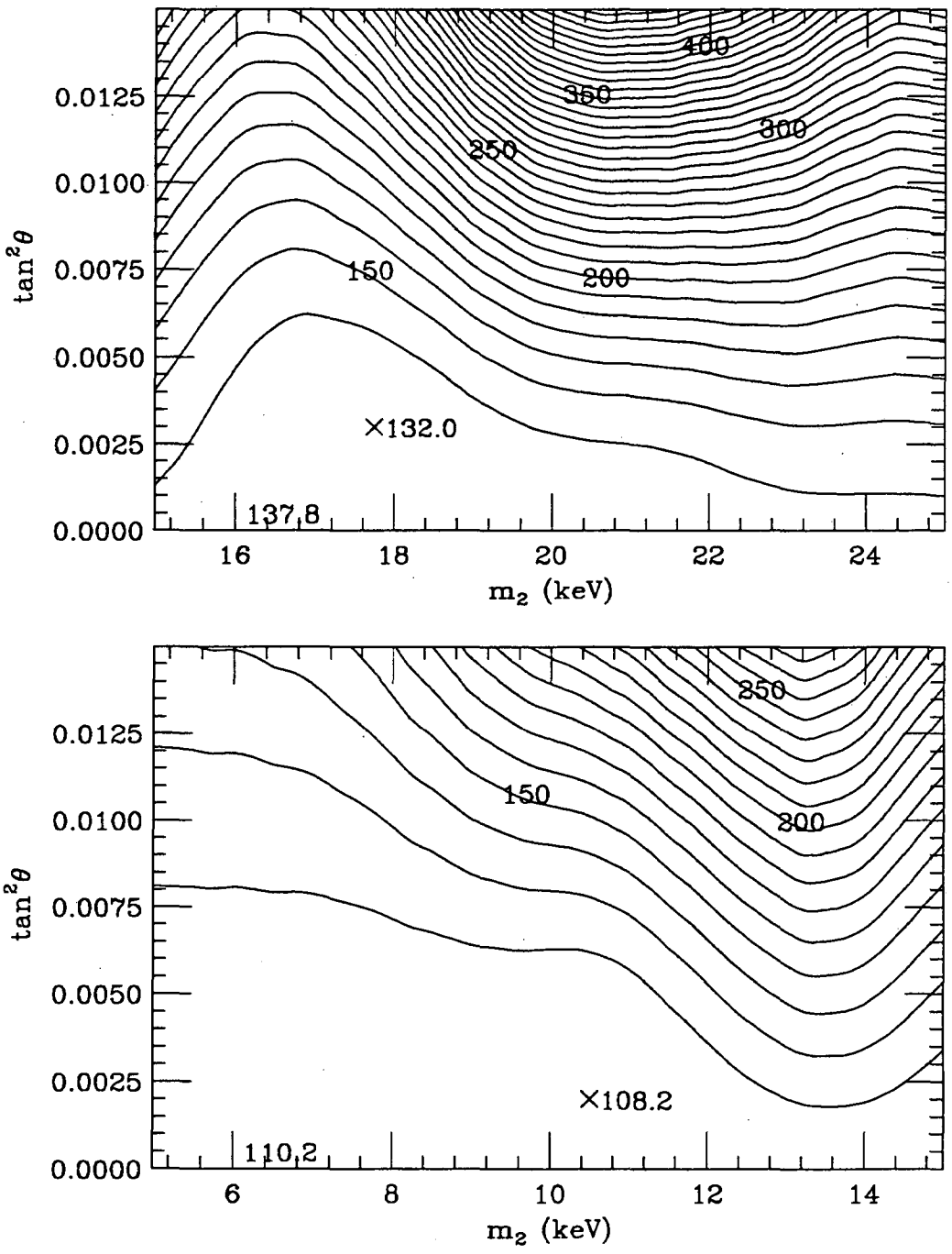

Figure 4.25: χ^2 contour plot for polynomial fits to ^{55}Fe spectrum B with 147-eV-wide bins in the regions 195–215 keV (136 points) (top), and 205–224 keV (129 points) (bottom).

4.5 Conclusions

The conclusion of this experiment is straightforward: there is no evidence for 17 keV neutrino emission in ^{55}Fe IBEC decay. A 17 keV neutrino with $\sin^2\theta$=0.008 is excluded at the 7σ level. Previous experiments were sensitive to the change in the global shape of a spectrum caused by emission of a massive neutrino; this can be mimicked or hidden by a small systematic distortion (as discussed in Section 2.5). The present result is significant because the experiment was sensitive to the local feature of the kink, which is unlikely to be influenced by a systematic distortion of the experimental spectrum. One might be concerned that detailed structure in the photon response of the detector might conspire in an energy-dependent way to create an actual kink (or anti-kink) in the spectrum. This seems *a priori* unlikely, but is a valid concern. The photon response of ^{55}Fe spectra A and B was very different, due to lack of Compton supression, from that of spectrum C. The fact that the kink searches in these spectra were also negative is strong evidence against this possibility.

A 2σ (95% CL) exclusion plot for neutrino masses in the range 5–25 keV is shown in figure 4.26, based on the polynomial fits to ^{55}Fe spectrum C. This plot includes the correction to $\tan^2\theta$ for higher-shell capture and pileup. The upper limit on the mixing of a neutrino with 17 keV mass is 0.14%. The weakest limit in the mass range explored is 0.65% for a 10.5 keV mass neutrino.

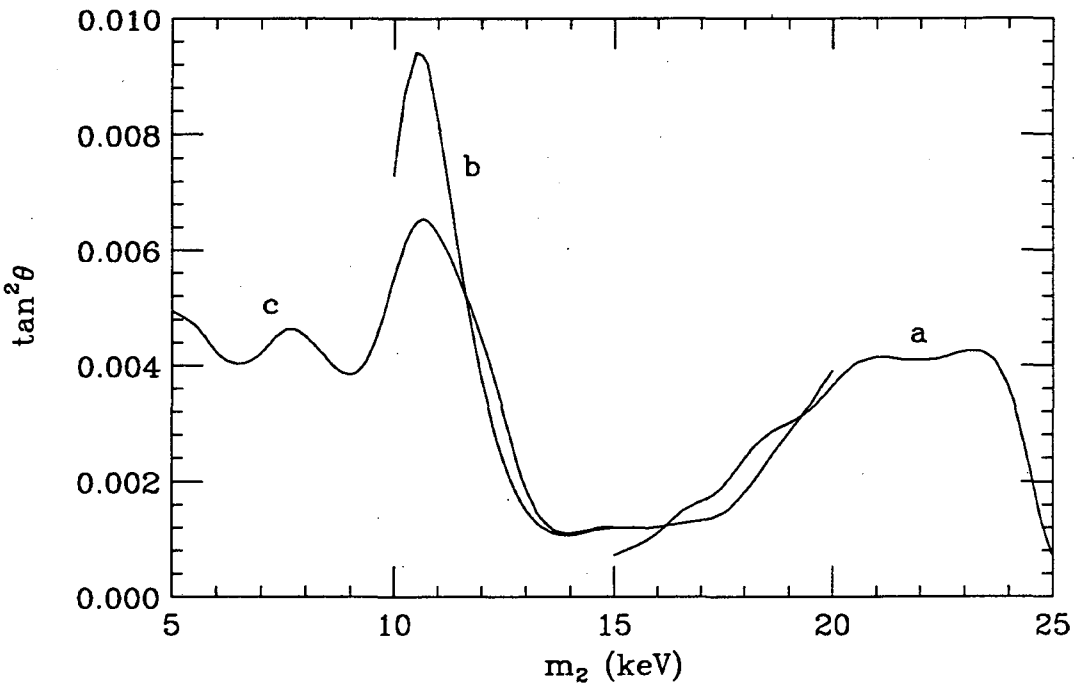

Figure 4.26: 2σ (95% CL) exclusion plot for neutrino masses from 5–25 keV, based on polynomial fits to ^{55}Fe spectrum C in the ranges (a) 195–215 keV, (b) 200–220 keV, and (c) 205–224 keV.

Chapter 5

Conclusions

From the point of view of fundamental physics, the 17 keV neutrino is no longer interesting. The experimental evidence against it is convincing. The general question of neutrino mass and mixing is still very important, but there is no further need to consider a 1% admixture of a 17 keV mass component in the electron neutrino. However in a broader sense the story of the 17 keV neutrino is still very relevant, and it should not be forgotten. It is a fascinating tale and an excellent case study of the scientific process; it teaches us valuable lessons about the use of precision spectroscopy to probe fundamental processes; and it raises the very interesting question of why a number of different research groups, using different methods, all found evidence for something that doesn't exist.

The 17 keV neutrino story represents a classic Hegelian dialectic. Simpson's initial report of the phenomenon in 1985 met with considerable skepticism (the thesis). After all, a 17 keV neutrino was completely unexpected, the experimental evidence favoring it was weak, and there seemed to be no theoretical basis for its existence. It was followed swiftly by negative experimental reports. A few years later, when new, more convincing positive results began to appear, it was generally realized that the initial reaction was premature. The field entered an antithetical period. The protagonists argued effectively that the early negative experiments

were inconclusive. The theoretical community began to take it seriously and viable models for a 17 keV neutrino were discussed. Experimental reports on both sides were in direct conflict, creating what one author called an "unresolved conundrum" [114]. Finally, the issues of experimental systematics and sensitivity were sorted out, and a new generation of experiments appeared that were able to conclusively rule out a 1% 17 keV neutrino. This was the synthesis. The 17 keV neutrino does not exist, but by studying the question of its existence we learned a lot about how to do these kinds of experiments correctly. In addition, the entire subject of neutrino mass and mixing was stimulated, which led to a development of theoretical ideas that may be very useful in the future.

The 17 keV neutrino experiments taught us how easily a systematic effect can masquerade as the signature for a new physical process. Obtaining a good χ^2 fit with the experimental spectrum is not sufficient; a convincing experiment must independently demonstrate its sensitivity to the effect in question. Seemingly negligible influences on the spectrum must not be taken for granted. An experimental response function that is used to fit the data should be measured at as many energies as possible, under the identical conditions as the beta spectrum, and must bracket the energy range being fit. Future efforts that use precision beta spectroscopy to probe fundamental physics will benefit tremendously from this experience.

It seems an extraordinary coincidence that, within a span of six years, seven different experiments at four different institutions each saw evidence for a 1% 17 keV neutrino for different reasons. If one considers the entire parameter space for neutrino mass and mixing, such a coincidence is inconceivable. Due to practical limitations however, the whole parameter space was not available to these experiments. The positive experiments all used roughly similar methods and had similar levels of statistics, even though the isotopes and apparatus designs were different. One might estimate the relevant parameter space to be about $5 < m_2 < 30$ keV

and $0.005 < \sin^2\theta < 0.05$. If an experiment of this type is going to mistake a systematic distortion for a massive neutrino signal, the parameters should fall within these ranges. The experiment will not be sensitive to a very small mass or mixing, and it can distinguish a sufficiently large mass or mixing from a systematic effect. With this in mind, the likelihood of this coincidence is small but not prohibitive.

We must also consider that subtle psychological effects may have played a role in this story. Scientists are human, and can be unknowingly influenced by social or subconscious pressures. For example, there is a tendency to make an experimental result public more quickly if it corroborates a previously reported result. One is more hesitant to go public if the result is something completely new, allowing more time to study the analysis and systematics. This may tend to bias a group of experiments toward agreement. It is beyond my purpose (and my competance) to expound further on the philosophical and sociological implications of the 17 keV neutrino, but I predict it will be a conspicuous subject for philosophers and historians of science in the years to come.

References

[1] W. Pauli, Letter to the Physical Society of Tubingen, unpublished (1930).

[2] A. Pais, *Niel Bohr's Times: In Physics, Philosophy, and Polity* (Clarendon Press, New York, 1991), p. 364–370.

[3] E. Fermi, Z. Physik **88**, 161 (1934).

[4] F. Reines and C. Cowan, Phys. Rev. **113**, 273 (1959).

[5] M. Fritschi, *et al.*, Nucl. Phys. B **19**, 205 (1991).

[6] R.G.H. Robertson, *et al.*, Phys. Rev. Lett. **67**, 957 (1991).

[7] N. Kawakami *et al.*, Phys. Lett. B **256**, 105 (1991).

[8] D. Decman and W. Stoeffl, presented at the 1993 Annual Meeting of the APS Division of Nuclear Physics, Asilomar CA.

[9] Particle Data Group, *Review of Particle Properties*, Phys. Rev. D **45** (1992).

[10] R. Abela, *et al.*, Phys. Lett. B **146**, 431 (1984).

[11] F. Boehm and P. Vogel, *Physics of Massive Neutrinos* (Cambridge University Press, Cambridge, second ed., 1992) p. 40.

[12] D. Cinabro, *et al.*, Phys. Rev. Lett. **70**, 3700 (1993).

[13] T. Kirsten, *et al.*, Phys. Rev. Lett. **50**, 474 (1983).

[14] S.R. Elliott, *et al.*, Phys. Rev. Lett. **59**, 2021 (1987).

[15] F.T. Avignone, *et al.*, Phys. Lett. B **256**, 559 (1991).

[16] S.R. Elliott, *et al.*, J. Phys. G Nucl. Phys. **17**, S145 (1991).

[17] M. Doi, *et al.*, Prog. Theor. Phys. Suppl. **83**, 1, Appendix A (1985).

[18] H.T. Wong, *et al.*, Phys. Rev. Lett. **67**, 1218 (1991).

[19] S.J. Freedman, *et al.*, Phys. Rev. D **47**, 811 (1993). I thank Brian Fujikawa for providing this plot.

[20] B. Blumenfeld *et al.*, Phys. Rev. Lett. **62**, 2237 (1989).

[21] L. Borokovsky, *et al.*, Phys. Rev. Lett. **68**, 274 (1992).

[22] L.A. Ahrens *et al.*, Phys. Rev. D **31**, 2732 (1985).

[23] G. Zacek *et al.*, Phys. Rev. D **34**, 2621 (1986).

[24] G. Gelmini, in *Neutrinos*, edited by H.V. Klapdor, (Springer-Verlag, Berlin, 1988) p. 313.

[25] A.H. Guth, Phys. Rev. D **23**, 347 (1981); A.D. Linde, Phys. Lett. B **108**, 389 (1982); A. Albrecht and P.J. Steinhardt, Phys. Rev. Lett. **48**, 1220 (1982).

[26] J. Yang *et al.*, Ap. J. **142**, 414 (1984).

[27] F. Boehm and P. Vogel, *op. cit.*, p. 222.

[28] *ibid.*, p. 83.

[29] J. Bahcall, *Neutrino Astrophysics* (Cambridge University Press, Cambridge, 1989) p. 14.

[30] R. Davis, Jr. *et al.*, in *Proceedings of the 21st International Cosmic Ray Conference*, Adelaide, Austrailia, 1989; J.N. Bahcall and M.H. Pinsonneault, Rev. Mod. Phys. **64**, 885 (1992).

[31] K.S. Hirata *et al.*, Phys. Rev. Lett. **65**, 1301 (1990).

[32] A.I. Abazov *et al.*, Phys. Rev. Lett. **67**, 3332 (1991).

[33] P. Anselmann *et al.*, Phys. Lett. B **285**, 376 (1992).

[34] L. Wolfenstein, Phys. Rev. D **17**, 2369 (1978); S.P. Mikheyev and A.Y. Smirnov, Sov. J. Nucl. Phys., **42**, 1441 (1985).

[35] S. Bludman *et al.*, Phys. Rev. D **47**, 2220 (1993).

[36] W. Marciano and A.I. Sanda, Phys. Lett. B **67**, 303. (1977).

[37] I. Goldman *et al.*, Phys. Rev. Lett. **60**, 1789 (1988); J. Lattimer and J. Cooperstein, Phys. Rev. Lett. **61**, 23 (1988).

[38] A. Burrows, *et al.*, Phys. Rev. Lett. **68**, 3834 (1992).

[39] J.N. Bahcall and S.L. Glashow, Nature **326**, 476 (1987).

[40] J.J. Simpson, Phys. Rev. Lett. **54**, 1891 (1985).

[41] W.C. Haxton, Phys. Rev. Lett. **55**, 807 (1985).

[42] B. Eman and D. Tadić, Phys. Rev. C **33**, 2128 (1986).

[43] J. Lindhard and P.G. Hansen, Phys. Rev. Lett. **57**, 965 (1986).

[44] E.G. Drukarev and M.I. Strikman, Zh. Eksp. Teor. Fiz. **91**, 1160 (1986); Phys. Lett. B **186**, 1 (1987).

[45] T. Altzitzoglou *et al.*, Phys. Rev. Lett. **55**, 799 (1985).

[46] A. Apalokov *et al.*, JETP Lett. **42**, 289 (1985).

[47] J. Markey and F. Boehm, Phys. Rev. C **32**, 2215 (1985).

[48] V.M. Datar *et al.*, Nature (London) **318**, 547 (1985).

[49] A. Carrington *et al.* Nucl. Inst. and Meth. **A248**, 425 (1986).

[50] T. Ohi *et al.*, Phys. Lett. B **160**, 322 (1985).

[51] J.J. Simpson, Phys. Lett. B **174**, 113 (1986).

[52] D.W. Hetherington *et al.*, Phys. Rev. **C36**, 1504 (1987).

[53] J.J. Simpson and A. Hime, Phys. Rev. **D39**, 1825 (1989).

[54] A. Hime and J.J. Simpson, Phys. Rev. **D39**, 1837 (1989).

[55] B. Sur *et al.*, Phys. Rev. Lett. **66**, 2444 (1991).

[56] A. Hime and N.A. Jelley, Phys. Lett. **B257**, 441 (1991).

[57] A. Hime and N.A. Jelley, Oxford University preprint OUNP-91-21 (1991).

[58] A. Hime, D. Phil. Thesis, Oxford (1991, unpublished).

[59] *ibid.*, p. 91–95.

[60] M.J.G. Borge, *et al.*, Phys. Scr. **34**, 591 (1986).

[61] I. Žlimen *et al.*, Phys. Scr. **38**, 539 (1988).

[62] I. Žlimen *et al.*, Phys. Rev. Lett. **67**, 560 (1991).

[63] E.B. Norman *et al.*, J. Phys. G **17**, S291 (1991).

[64] D.E. DiGregorio *et al.*, presented at the Workshop on the 17 keV Neutrino Question, Berkeley, 1991.

[65] G. Bonvincini, Z. Phys. A **345**, 97 (1993).

[66] I. Žlimen, D. Phil. Thesis, University of Zagreb (1991, unpublished).

[67] K. Schreckenbach *et al.*, presented at the Workshop on the 17 keV Neutrino Question, Berkeley (1991).

[68] S.L. Glashow, Phys. Lett. B **256**, 255 (1991).

[69] A.E. Nelson, Nucl. Phys. B **380**, 543 (1992).

[70] I.Z. Rothstein, Mod. Phys. Lett. A **7**, 821 (1992).

[71] G. Gelmini *et al.*, Int. J. Mod. Phys. A **7**, 3141 (1992).

[72] J.T. Peltoniemi *et al.*, Phys. Lett. B **286**, 321 (1992).

[73] H. Kawakami *et al.*, Phys. Lett. B **287**, 45 (1992).

[74] T. Ohshima *et al.*, Phys. Rev. D **47**, 4840 (1993).

[75] J.L. Mortara *et al.*, Phys. Rev. Lett. **70**, 394 (1993).

[76] J.D. Jackson, *Classical Electrodynamics* (Wiley, New York, second ed., 1975) p.588–593.

[77] F.E. Wietfeldt *et al.*, Phys. Rev. Lett. **70**, 1759 (1993).

[78] M. Chen *et al.*, Phys. Rev. Lett. **69**, 3151 (1992).

[79] G.E. Berman *et al.*, Phys. Rev. C **48**, R1 (1993).

[80] D.E. DiGregorio *et al.*, Phys. Rev. C **47**, 2916 (1993).

[81] M. Bahran and G. Kalbfleisch, Phys. Lett. B **291**, 336 (1992); G. Kalbfleisch and M. Bahran, Phys. Lett. B **303**, 355 (1993).

[82] H. Abela *et al.*, Phys. Lett. B **316**, 26 (1993).

[83] M.M. Hindi *et al*, preprint (1994).

[84] D.C. Conway and W.H. Johnson, Phys. Rev. **116**, 1544 (1959).

[85] S.E. Koonin, Nature **354**, 468 (1991).

[86] J.J. Simpson, personal communication (1994).

[87] L. Piilonen and A. Abashian, presented at the XIIth Moriond Workshop (1992).

[88] A. Hime, Phys. Lett. B **299**, 165 (1993); A. Hime, personal communications (1993–94).

[89] M.G. Bowler and N.A. Jelley, Oxford University preprint OUNP-94-04 (1994, submitted to Phys. Lett. B); N.A. Jelley, personal communication (1994).

[90] E. Browne and R.B. Firestone, *Table of Radioactive Isotopes* (Wiley, New York, 1986).

[91] L. Pages *et al.*, At. Data **4**, 1 (1972).

[92] E.E. Haller, *et al.*, IEEE Trans. Nucl. Sci. **29**, 160 (1982).

[93] M. Morita, *Beta Decay and Muon Capture* (W.A. Benjamin, Reading, Mass., 1973) p.33.

[94] D.H. Wilkinson, Nucl. Instr. and Meth. **A275**, 378 (1989).

[95] H. Behrens and W. Bühring, *Electron Radial Wave Functions and Nuclear Beta Decay* (Clarendon Press, Oxford, 1982) p.146–147.

[96] *ibid.*, p.431–432.

[97] J.K. Knipp and G.E. Uhlenbeck, Physica **3**, 425 (1936).

[98] M. Morita, *op. cit.*, p.33.

[99] R.P. Feynman and M. Gell-Mann, Phys. Rev. **109**, 193 (1958); M. Gell-Mann, Phys. Rev. **111**, 362 (1958).

[100] A. García, personal communication (1992).

[101] R. Brun, *et al.*, GEANT3, CERN, DD/EE/84-1, (1987).

[102] STEPIT, written by J.P. Chandler, University of Indiana, Bloomington, IN.

[103] W.J. Veigele, At. Data **5**, 51 (1973).

[104] P.N. Luke and E.E. Haller, J. Appl. Phys. **59**, 3734 (1986).

[105] L.G. Smith and A.H. Wapstra, Phys. Rev. C **11**, 1392 (1974).

[106] M.A. Mariscotti, Nucl. Instr. and Meth. **50**, 309 (1967).

[107] I. Žlimen *et al.*, Phys. Rev. C **46**, 1136 (1992).

[108] R.J. Glauber and P.C. Martin, Phys. Rev. **104**, 158 (1956); P.C. Martin and R.J. Glauber, Phys. Rev. **109**, 1307 (1958).

[109] W. Bambynek *et al.*, Rev. Mod. Phys. **49**, 77 (1977).

[110] R. P. Feynman, Phys. Rev. **76**, 749 (1949).

[111] A. De Rújula, Nucl. Phys. **B188**, 414 (1981).

[112] M.J. Martin and P.H. Blichert-Toft, Nucl. Data **A**, 1 (1970).

[113] G.F. Knoll, *Radiation Detection and Measurement* (Wiley, New York, 1989), p.459.

[114] A. Hime, *Pursuing the 17 keV Neutrino*, Mod. Phys. Lett. A **7**, 1301 (1992).

[115] V. Radeka, Ann. Rev. Nucl. Part. Sci **38**, 217 (1988).

[116] I am grateful to Paul Luke for preparing these plots and for helpful discussions about the bipolar pulses.

[117] I thank Paul Luke and Eugene Haller for explaining this phenomenon to me.

Appendix A

The ^{14}C Detector

This appendix contains technical issues concerning the ^{14}C-doped germanium detector described in Chapter 3.

A.1 Bipolar Image Pulses

The following discussion is based on the more general derivation by Radeka [115]. Figure A.1 depicts the interior of the detector where a localized region of ionization charge q, created by a beta or gamma event, is drifting toward the center region anode with velocity v_d. The cathode, the center and guard ring anodes, and the ionization region are treated as ideal conductors separated by a dielectric medium. A solution to the Laplace equation is determined if we specify either the potential V_i (relative to ground) or the charge Q_i, at each conductor. Consider two different configurations, the actual case a, and a hypothetical case b:

$$\begin{array}{lll} a) \quad \text{actual case:} & V_0 = V_{bias} \quad V_1 = 0 & \\ & V_2 = 0 \quad\quad Q_3 = q & \\ b) \quad \text{hypothetical case:} & V_0 = 0 \quad\quad V_1 = 0 & \\ & V_2 = 1 \quad\quad Q_3 = 0. & \end{array} \tag{A.1}$$

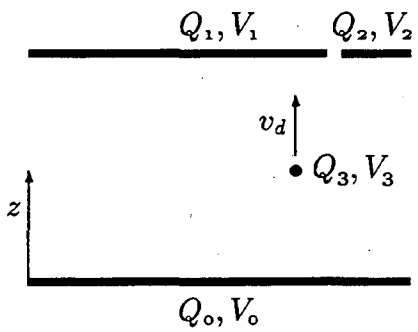

Figure A.1: A localized region of ionization charge inside the detector drifting toward the center electrode.

We use Green's reciporocity theorem to relate the two cases:

$$\sum_{i=0}^{3} Q_i^a V_i^b = \sum_{i=0}^{3} Q_i^b V_i^a \tag{A.2}$$

giving

$$Q_2^a + qV_3^b = Q_0^b V_{bias}. \tag{A.3}$$

Differentiating with respect to time:

$$-j_2 = -q\frac{d}{dt}\left(V_3^b\right) \tag{A.4}$$

or

$$j_2 = qv_d\frac{d}{dz}\left(V_3^b\right) = -q\vec{v_d}\cdot\vec{E_3^b} \tag{A.5}$$

where j_2 is the current flowing out of the guard ring anode into the preamp in the actual case. E_3^b, called the weighting field, is the electric field in the hypothetical case. It conveniently contains all of the geometry in the problem. We can integrate (A.5) to obtain the total charge collected in the guard ring as a function of the position z of the ionization charge:

$$Q_2(z) = qv_d V_3^b(z). \tag{A.6}$$

Since we are interested only in the transient behavior we take the constant of integration to be zero. The charge collected in the center is obtained in in a similar way by considering a new hypothetical case c:

$$\begin{aligned} c) \quad \text{hypothetical case:} \quad & V_0 = 0 \qquad V_1 = 1 \\ & V_2 = 0 \qquad Q_3 = 0 \end{aligned} \tag{A.7}$$

which gives

$$Q_1(z) = q v_d V_3^c(z). \tag{A.8}$$

The weighting potentials $V_3^b(z)$ and $V_3^c(z)$ can be found by solving the Laplace equation numerically, as shown in Figure A.2 [116]. In these plots, the gradient of the weighting potential along the path of the drifting ionization charge is proportional to the current signal in each preamp. The center preamp sees a positive pulse that integrates to q. The guard ring preamp sees a bipolar pulse that integrates to 0. Likewise, the center preamp sees a bipolar pulse when an ionization event occurs in the guard ring. These bipolar pulses are highly attenuated by the preamps. When the amplified signals associated with gamma-ray interactions were observed with an oscilloscope, the bipolar pulses had amplitudes of only 1–3% of the true pulses.

A.2 Surface Effects

The crystal lattice ends abruptly at the edge of a solid state detector, so the band structure is highly distorted there. This can create a surface channel, causing the electric field lines to terminate at the edge instead of running straight to the opposite electrode (see Figure A.3). When this occurs, charge from an ionization event near the edge can be diverted to the surface and become trapped. Tiny amounts of surface contamination can influence the size of the effect.

We can use the results of the previous section to determine the detector response for such an event [117]. Suppose the ionization charge drifts through the

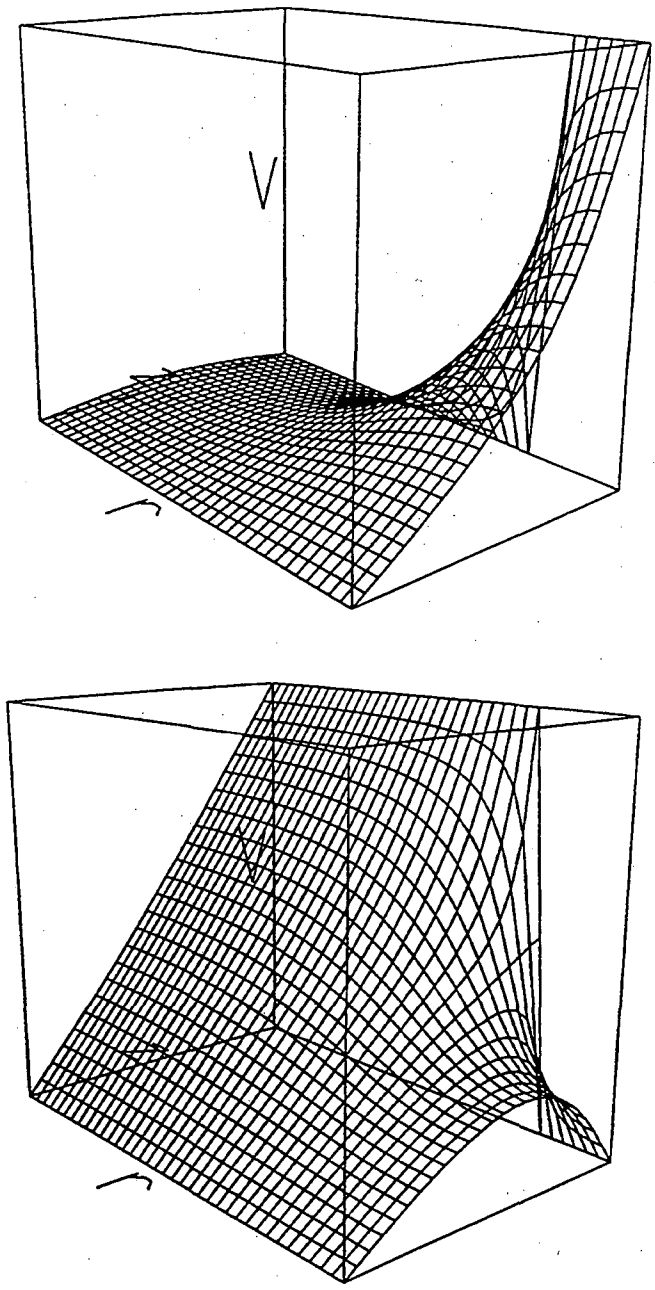

Figure A.2: Numerical solutions of the Laplace equation for the weighting potentials $V_3^b(z)$ (top) and $V_3^c(z)$ (bottom)

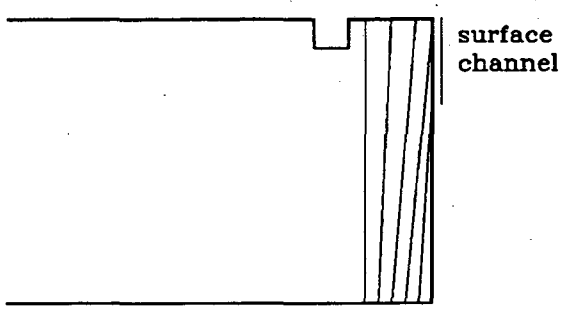

Figure A.3: A surface channel on the edge of the detector can cause the electric field lines to terminate at the edge.

detector until it becomes trapped at the surface at position $z = z_{tr}$. The trapped charge travels slowly along the surface, so the signals seen by the center and guard ring preamps are simply the integrated charges collected at the anodes at the time of trapping. According to (A.6) and (A.8) these are $Q_1(z_{tr}) \propto V_1^c(z_{tr})$, and $Q_2(z_{tr}) \propto V_2^b(z_{tr})$. Figure A.4 shows a plot of the center signal verses the guard ring signal for different z_{tr}, based on the weighting potentials of Figure A.2. The shape of this coincidence plot is a function of geometry alone, although its intensity will depend on the size of the surface channel. Compare Figure A.4 to the actual ^{141}Ce 2-D spectrum in Figure 3.11.

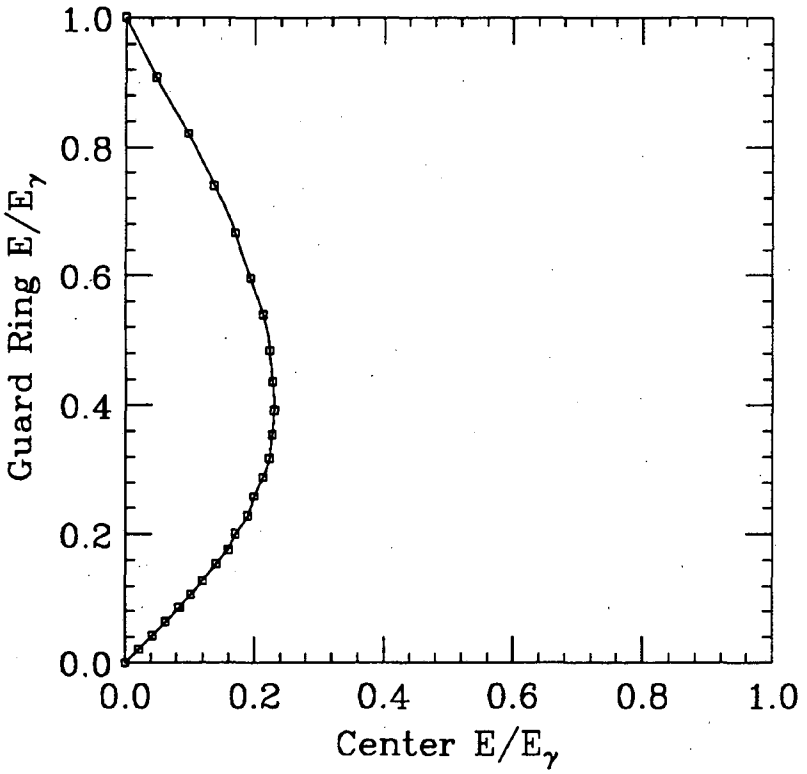

Figure A.4: Predicted plot of center-guard ring coincidences caused by the surface effect.

Appendix B

Second Derivatives of ^{55}Fe Spectra

As discussed in Chapter 4, the second derivative is a simple and powerful way to reveal a massive neutrino kink in a beta or IBEC spectrum. Unfortunately, the statistical dispersion in the data is magnified enormously by taking derivatives. The dispersion in the second derivative can be reduced by binning the data. Pseudodata studies showed that compressing the data into twenty-channel bins (2.60 keV/bin for ^{55}Fe spectrum C) maximized the sensitivity of the second derivative to a neutrino kink in the experimental ^{55}Fe spectrum. However, with such coarse binning the size of the effect will depend on the position of the kink with respect to the bins; the kink-peak will be smaller if it is split between two bins than if contained in only one. For this reason twenty binned spectra were created from each background-subtracted ^{55}Fe spectrum (A,B,C). Each contained twenty channels per bin but a different channel offset. Second derivatives were taken of all of these binned spectra. Representative samples of these are shown in Figures B.1a,b,c. The residual from subtracting the 192 keV is significant in some of the spectra, but none show evidence for the presence of a massive neutrino kink (compare to the pseudodata, Figure 4.12).

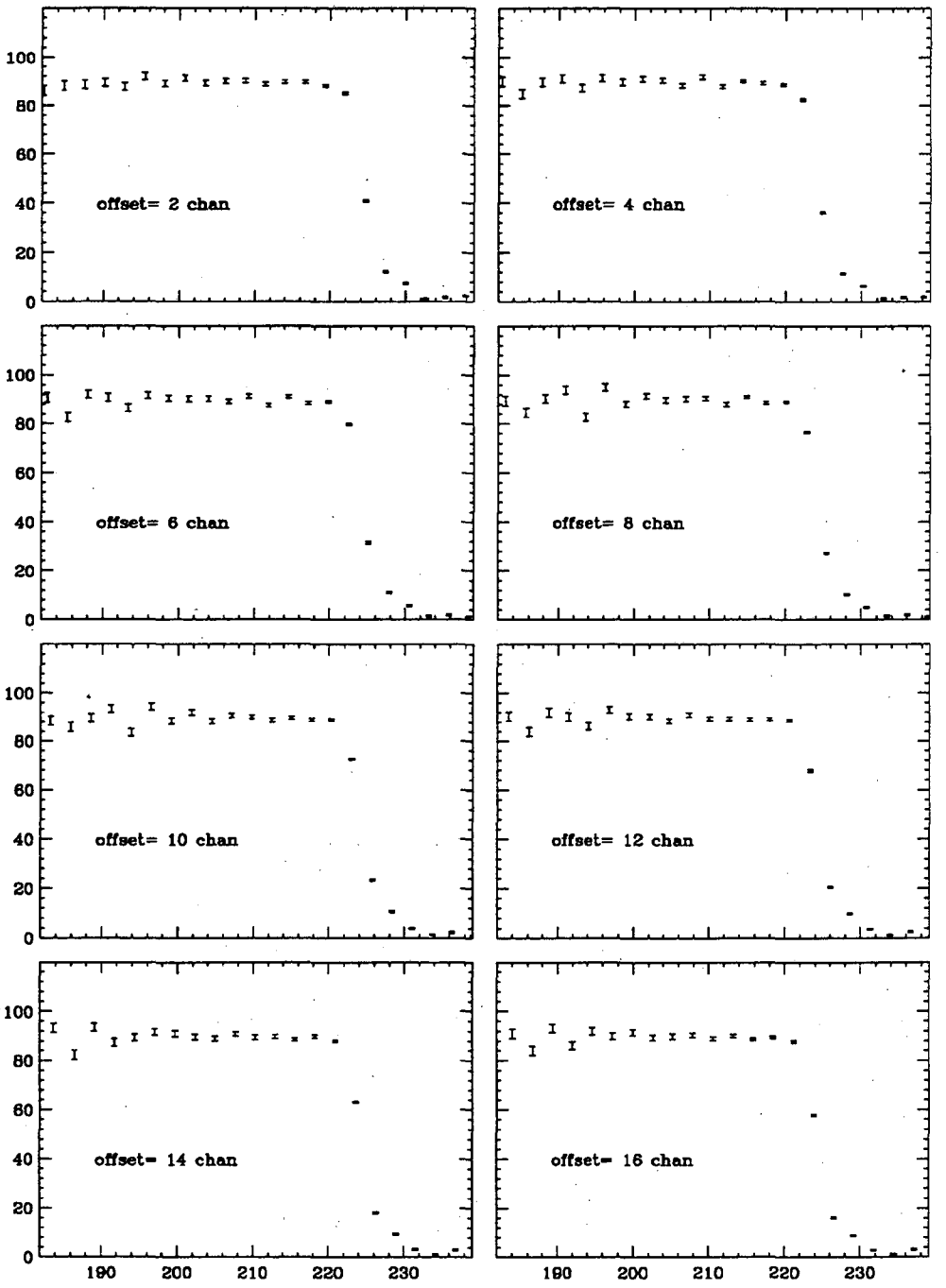

Figure B.1a: Second derivatives of ^{55}Fe spectrum A (no vetos) compressed into 20 channel bins with different channel offsets.

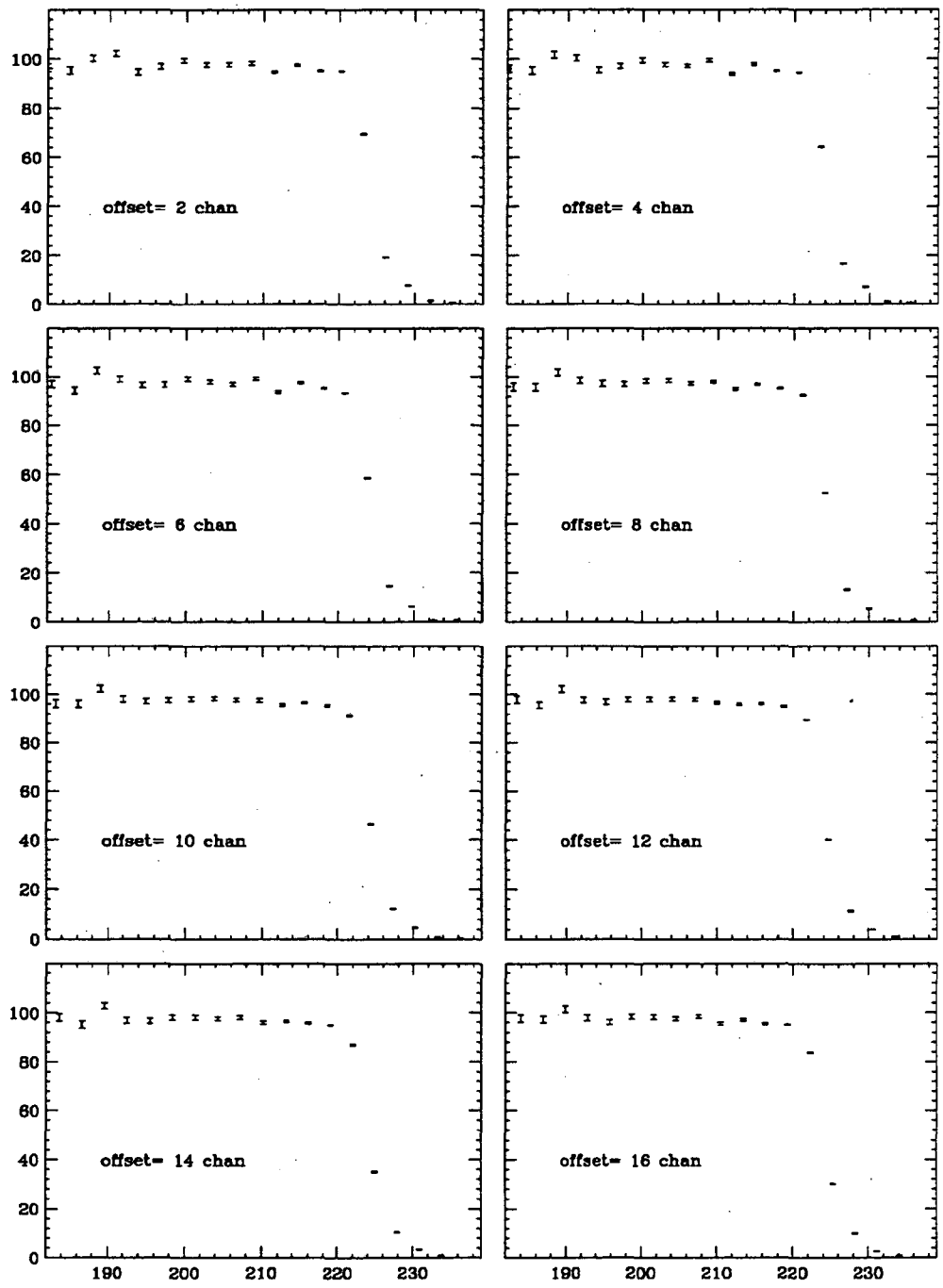

Figure B.1b: Second derivatives of ^{55}Fe spectrum B (PUR only) compressed into 20 channel bins with different channel offsets.

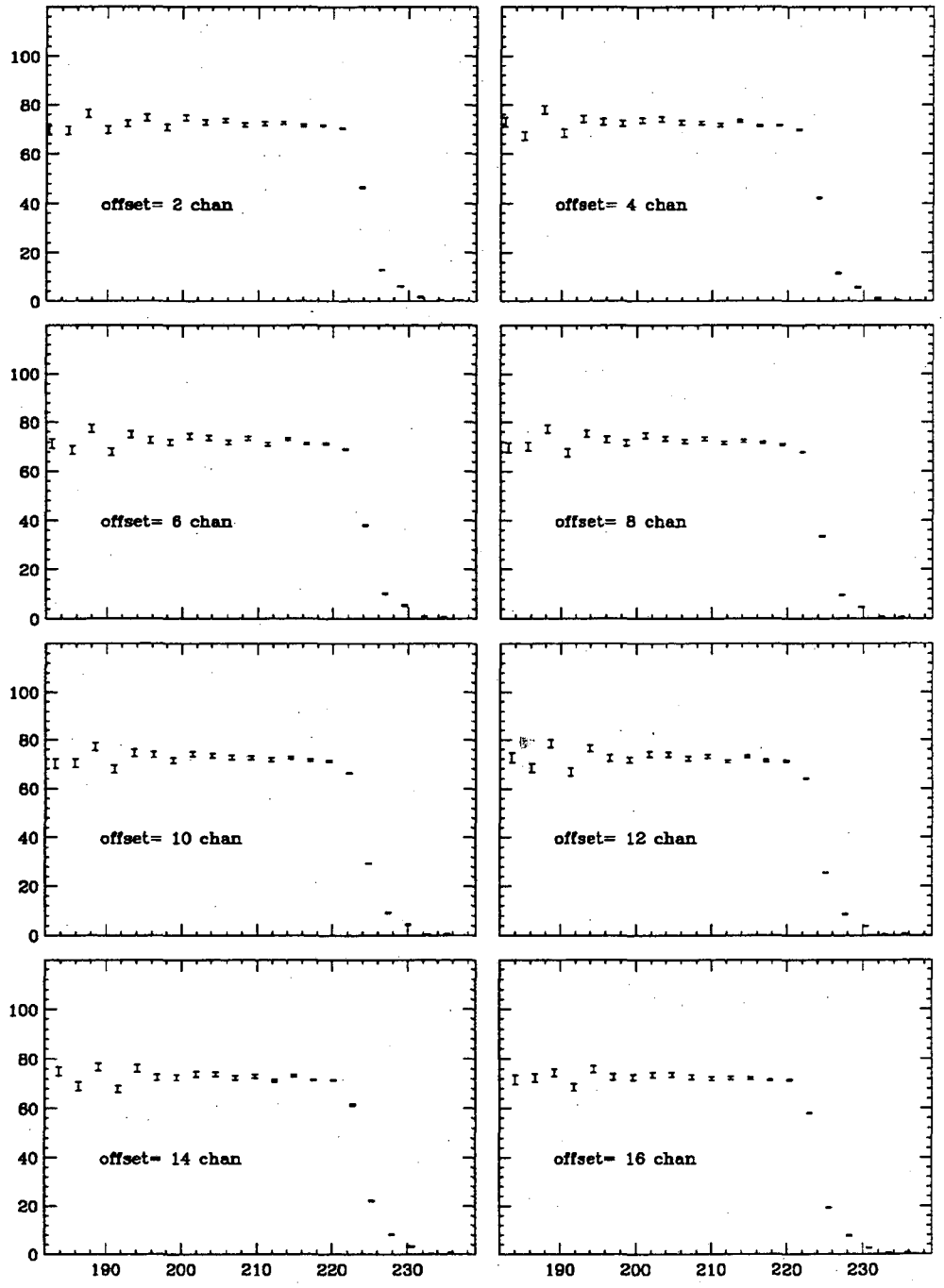

Figure B.1c: Second derivatives of ^{55}Fe spectrum C (PUR and NaI veto) compressed into 20 channel bins with different channel offsets.

LAWRENCE BERKELEY LABORATORY
UNIVERSITY OF CALIFORNIA
TECHNICAL INFORMATION DEPARTMENT
BERKELEY, CALIFORNIA 94720